DENSITY FUNCTIONAL THEORY STUDY OF OXIDIZED EPITAXIAL GRAPHENE

A Thesis
Presented to
The Academic Faculty

by

Si Zhou

In Partial Fulfillment
of the Requirements for the Degree
Doctor of Philosophy in the
School of Physics

Georgia Institute of Technology
August 2014

DENSITY FUNCTIONAL THEORY STUDY OF OXIDIZED EPITAXIAL GRAPHENE

Approved by:

Dr. Angelo Bongiorno, Advisor
School of Physics
Georgia Institute of Technology

Dr. Edward Conrad
School of Physics
Georgia Institute of Technology

Dr. Andrew Zangwill
School of Physics
Georgia Institute of Technology

Dr. Dennis W. Hess
School of Chemical & Biomolecular Engineering
Georgia Institute of Technology

Dr. Meiyin Chou
School of Physics
Georgia Institute of Technology

Date Approved: 1 July 2014

ACKNOWLEDGEMENTS

First and foremost, I would express my sincere gratitude to my advisor Dr. Angelo Bongiorno for his guidance and support throughout my Ph.D. studies. His continuous assistance, inspiration, patience, and trust have not only helped me to complete my thesis work, but also led me the way to be an independent and open-minded scientist. His passion, dedication, wisdom, as well as his rigor and high standards toward science have deeply impacted me, which would be a great fortune for my future academic career.

I sincerely thank for my committee members: Dr. Dennis Hess, Dr. Andrew Zangwill, Dr. Meiyin Chou, and Dr. Edward Conrad for taking their time to review my thesis and provide valuable comments and suggestions.

My special thanks go to Dr. Elisa Riedo, who first introduced this "graphene project" to me. During our collaborations on this project, she has provided so many creative insights and suggestions on my work. I would also like to thank all of our collaborators on this project: Dr. Walt de Heer, Dr. Claire Berger, Dr. Yike Hu, Dr. Suenne Kim, Dr. Douglas Chiu, Dr. Emiliano Gennaro, Dr. Carmela Aruta, and Dr. Yves Chabal. I could not complete my thesis work without their excellent jobs in experiment and insightful discussions.

I deeply thank my friends in Atlanta for their help and support, as well as the happy time we have spent together: Chu Han, Annie Lesiak, Feng Wang, Xue Dong, Wenlong Yu, Wenchao Jiang, Feifei Qian, James Palmer, Heather Palmer, Lede Xian, Xi Lu, and Yang Gao.

Finally, and most importantly, I would like to thank my husband Xunchi Chen for his company, support and encouragement throughout the past eight years. I am deeply grateful for my parents Meng Miao and Shaoli Zhou who gave me my life and raised me up. I owe them forever.

TABLE OF CONTENTS

ACKNOWLEDGEMENTS . . . . . **iii**

LIST OF TABLES . . . . . **vii**

LIST OF FIGURES . . . . . **viii**

SUMMARY . . . . . **xiv**

I INTRODUCTION **1**

1.1 Graphene and its chemically modified forms 1

1.1.1 Structure, properties and applications 1

1.1.2 Epitaxial graphene on SiC 3

1.1.3 Chemically modified graphene 4

1.2 Oxidized epitaxial graphene 5

1.2.1 Synthesis of EGO 6

1.2.2 Experimental information 6

1.3 Thesis outline 8

II DENSITY FUNCTIONAL THEORY **9**

2.1 The electron many-body problem 9

2.2 The Hohenberg-Kohn theorems 11

2.3 The Kohn-Sham formalism 12

2.4 Local density and generalized gradient approximations of DFT 14

2.5 Technical and numerical aspects 15

2.5.1 Plane-wave basis set 15

2.5.2 Pseudopotentials 17

2.6 Dispersion interactions and DFT 19

2.7 Technical details of my DFT calculations 21

III CHEMICAL COMPOSITION AND STABILITY OF EGO FILMS . **22**

3.1 X-ray photoelectron spectroscopy 22

3.1.1 Basic concepts 22

3.1.2 Calculations of core-level shifts 24

3.1.2.1 Hartree-Fock method 25

3.1.2.2 Density functional theory method 26
3.1.3 A pseudopotential approach for calculating core-level shifts 27
3.2 Calculations of XPS spectra for multilayer EGO films 30
3.2.1 Model structures of multilayer EGO films 31
3.2.2 Computed XPS spectra for as-synthesized EGO 32
3.2.3 Computed XPS spectra for aged EGO 35
3.2.4 Proposed reduction mechanism 36
3.3 Summary of main results 38
IV ORIGIN OF CHEMICAL AND KINETIC STABILITY OF EGO . . 39
4.1 Methods 39
4.1.1 Calculation of chemical reaction rates 39
4.1.1.1 Transition state theory 39
4.1.1.2 The nudged elastic band method 41
4.1.2 The Metropolis Monte Carlo algorithm 43
4.2 Stability of graphene oxide: kinetics and thermodynamics 45
4.2.1 Isolated oxygen species on graphene 45
4.2.2 Dimeric oxygen species on graphene 48
4.2.2.1 Decomposition reactions 48
4.2.2.2 Pair-wise association energies 50
4.2.3 Graphene oxide with arbitrary chemical compositions 53
4.2.3.1 A simplistic energy scheme 53
4.2.3.2 A lattice-model Monte Carlo method 56
4.2.3.3 Intralayer structure and stability of aged EGO 58
4.2.3.4 Comparison with DFT models 60
4.3 Summary of main results 63
V THE INTERLAYER STRUCTURE OF EGO FILMS 65
5.1 EGO models with homogeneously oxidized layers 65
5.2 EGO models with non-homogeneously oxidized layers 66
5.3 Summary of main results 69

VI CONCLUSION **71**

6.1 Summary 71

6.2 Future Considerations 72

REFERENCES **73**

LIST OF TABLES

1 Lattice parameters (a and c), bulk modulus (B), and interlayer binding energy (E_b) of graphite. Present results obtained by DFT and DFT-D are compared to the experimental values and results from other calculations. . . 20

2 Geometrical parameters and binding energy (E_0) of a water dimer. Present results obtained by DFT and DFT-D schemes are compared to the experimental values. E_0 is referred to the energy of two isolated water molecules in vacuum. 21

3 C 1s core-level energy shifts (in eV) of C atoms in selected molecules. The chemical shifts are referred to that of C in CO. ΔC_{1s} and $\Delta^a C_{1s}$ are calculated values by accounting for the vertical transition and adiabatic effect, respectively. 29

4 O 1s core-level energy shifts (in eV) of O atoms in selected molecules. The chemical shifts are referred to that of O in CO. ΔO is calculated values by accounting for the vertical transition. 30

5 Chemical, geometrical, and energetic information of model structures of as-synthesized EGO generated from DFT-D. The models have an O:C ratio of 0.44. The fractions of C-O-C, C-OH, and H_2O species are referred to the total number of C atoms. Mean interlayer separation, average intralayer vertical buckling, and mean interlayer binding energy are indicated by d, Δd, and E_b, respectively. 32

6 Chemical, geometrical, and energetic information of model structures of aged EGO generated from DFT-D. The models have an O:C ratio of 0.38. Labels are the same as that in Table 5. 32

LIST OF FIGURES

1 (a) Graphene real-space lattice structure (left) and Brillouin zone (right). Red and blue circles indicate sublattices A and B, respectively. Lattice vectors $\mathbf{a}_1$ and $\mathbf{a}_2$, reciprocal lattice vectors $\mathbf{b}_1$ and $\mathbf{b}_2$, and the Dirac points $\mathbf{K}$ and $\mathbf{K}'$ are indicated. (b) Electronic dispersion in the honeycomb lattice [82]. Left: energy spectrum (in unit of t) for finite values of t and t', with t=2.7 eV and t'=-0.2t. Right: zoom in of the energy bands close to one of the Dirac points. 2

2 (a) Schematic layer structure of epitaxial graphene on Si-face 6H-SiC [69]. (b) A monolayer graphene on the bulk-truncated Si-face SiC surface. The large diamond indicates the unit cell of the $(6\sqrt{3}\times 6\sqrt{3})R30^\circ$ reconstruction [29]. 4

3 Rotational stacking faults in multilayer epitaxial graphene (MEG) on C-face SiC. (a) Schematic $(\sqrt{13}\times\sqrt{13})R46.1^\circ$ unit cell alignment of two graphene sheets [50]. (b) Scanning tunneling microscopy image of the moiré superlattice on the top layer of a nominally 10-layer MEG sample [50]. (c) Angle-resolved photoemission spectroscopy of band structure of an 11-layer graphene film grown on C-face 6H-SiC measured at 6 K. The wavevector scan is perpendicular to the SiC $(10\bar{1}0)$ at the $\mathbf{K}$ point. Two linear Dirac cones are visible [112]. 5

4 (a) Experimental C 1*s* XPS spectra of EGO films at increasing aging times at room temperature: 1 day, 40 days and 70 days after their synthesis. The three fitted components are assigned to unoxidized C (blue), C-O-C and C-OH (orange), and C=O (green). (b) XRD ω-2θ spectra of an $11(\pm1)$-layer EGO film (blue), a $12(\pm1)$-layer EG film (red), and a bare 4H-SiC $(000\bar{1})$ substrate (black). The asterisks refer to the peaks of the substrate. 7

5 (a) DFT total energy vs. energy cutoff for graphene. (b) Electronic band structure of graphene calculated by DFT. Graphene in (a) and (b) is represented by its primitive unit cell, with a lattice constant of 2.47 Å. The Brillouin zone is sampled by a uniform $48\times48\times1$ $\mathbf{k}$ point mesh. 16

6 (a) Schematic illustration of all-electron wavefunction (blue) vs. pseudo wavefunction (red). (b) Nuclear Coulomb potential (blue) vs. pseudopotential (red). 17

7 (a) Interlayer binding energy vs. interlayer distance in graphite calculated by DFT (black) and DFT-D (red) schemes. (b) Model structure of a water dimer. The values of geometrical parameters R_{oo}, β, θ_a, and θ_b obtained by DFT and DFT-D are reported in Table 2. 20

8 (a) Basic components of a XPS spectrometer system, including radiation source, specimen, electron energy analyzer, and detector. (b) Energy diagram of a metallic specimen in electrical equilibrium with a XPS spectrometer. The kinetic energy of photoelectrons are measured in the spectrometer, where the vacuum level may be different from that in the UHV chamber. Thus $E_b^V(k)$ can not be directly acquired. For gas phase molecules, $E_b^V(k)$ is obtained by measuring the kinetic energy of photoelectrons relative to that of a standard species with a precisely known ionization potential [126]. For solids, no such standards are available, and the binding energy is most commonly referred to the Fermi level of the specimen [13], which is in electrical contact with the spectrometer. For metallic materials, both Fermi levels are at equal energies. The Fermi-level referred binding energy $E_b^F(k)$ is given by $E_b^F(k) = h\nu - E_{kin} - \phi_{spect}$, where E_{kin} is the kinetic energy measured in the spectrometer; ϕ_{spect} is the work function of the spectrometer. The vacuum-referred binding energy $E_b^V(k)$ can be obtained by $E_b^V(k) = E_b^F(k) + \phi_s$, once the work function of the specimen ϕ_s is known. For semiconductors and insulators, the Fermi level is not well defined. The specimen may carry net charges as emitted photoelectrons are not replaced by electrons from the ground. Usually low energy electrons are used to flood the specimen to insure charge equilibrium. 23

9 Experimental vs. computed (a) C 1s and (b) O 1s chemical shifts of C and O in selected molecules, shown by the ball-and-stick illustration. Grey, red and white colors (hereafter) represent C, O and H atoms, respectively. The energy shifts are referred to that of C and O in the CO molecule. Black discs and cyan triangles are computed values by accounting for the vertical photoexcitation transition and the adiabatic effect, respectively. To calculate the latter quantities, the geometry of the ionized system is fully relaxed, and E[C^+] is computed under the new structure. Chemical shifts obtained by using the two schemes are very close, with difference less than 0.1 eV on average. Given the good performance of the vertical transition scheme, the adiabatic effects will not be considered in the following work. 29

10 (a) Model structure of EGO generated from DFT-D. (b) A selected region of the same model showing the predominant chemical species present in EGO; clockwise from the top and indicated by the green arrows: a C-H species, an epoxide group, a water molecule, and a hydroxyl group. 31

11 Experimental (circles) and computed (lines) C 1s XPS spectra of as-synthesized EGO. Shirley background is subtracted from the experimental data. The chemical compositions of the models are reported in Table 5. 33

12 Calculated C 1s XPS spectra (black line) of model A-D, compared with the experimental spectra of as-synthesized EGO (circles). The computed spectra are decomposed in four peaks: unoxidized C (red line), C-O-C and C-OH (blue line), C bonding to ether groups (green line), and doubly oxidized C species (magenta line). 34

13 Distribution of C-O-C bond angle extracted from the EGO models. Epoxide and ether groups are clearly distinguishable by this geometrical parameter. The atomistic structures of doubly oxidized C species are shown as inset and on the right. 34

14 Experimental (circles) and computed (lines) C 1s (left) and O 1s (right) XPS spectra of aged EGO. Shirley background is subtracted from the experimental data. The chemical compositions of the models are reported in Table 6. . . 35

15 (a) DFT energy diagram of the reduction process in EGO. The line segments show the energy levels of the reactants and products (black), and the transition states (cyan) of the two reactions, all referred to that of a H_2O molecule physisorbed on graphene. The corresponding optimized atomic configurations are shown next to their energy levels. (b) The diffusion processes of individual -H, -O- and -OH species on graphene given by NEB-DFT calculations. The optimized structures of the three species in equilibrium and transition state are shown on the right and top of the energy profile, respectively. 37

16 Energy profiles of the reaction processes of (a) -H and -O- to the formation of -OH, (b) -H and -OH to the formation of a physisorbed water on graphene, obtained by NEB-DFT calculations. The atomic configurations of the initial state (top and side views), transition state and final state are shown as inset next to their corresponding energy points marked by red discs. The energy values are referred to that of the initial state. 37

17 (a) A two-dimensional potential energy landscape. Regions A and B shown in dark gray are two local minima, connected by the minimum energy path (MEP) indicated by the dark line. The dashed curves represent the energy surface equal to the transition state energy. The black discs labeled by numbers represent the images used in a NEB calculation. (b) One-dimensional energy profile of a MEP. 40

18 Binary decomposition reactions between epoxide and hydroxyl groups on one side or on both sides of graphene. Energy values correspond to ΔG per oxygen functional group computed via Equation (119). Relevant energy barriers are obtained by NEB-DFT calculations. 49

19 The energy profile and optimized atomic configurations in the reaction process to the formation of a O_2 molecule from two epoxide groups on graphene, by NEB-DFT calculations. The red and blue curves are the potential energy surfaces for the two oxygen in singlet and triplet state, respectively. The zero energy level is shifted to the energy of the initial system in singlet state. The atomic configurations of the initial state, transition states, metastable state, and final state are shown next to their corresponding energy points marked by the black filled symbols. The crossing point of the two potential energy surfaces is circled. 50

20 Pair-wise association energy (symbols) of binary epoxide-epoxide (red), hydroxyl-hydroxyl (blue), and epoxide-hydroxyl (cyan) complexes on graphene with the two oxygen species separated by up to 4 C=C bonds. Energy values are referred to that of two isolated oxygen units on graphene. Insets show examples of binary complexes having functional groups separated by one, two, and three C=C bonds (asterisks). Detailed energetic information and atomic configurations are shown in Figure 21, 22 and 23. Solid lines are guide to the eye. 51

21 Pair-wise association energy of epoxide groups on graphene. The atomic configurations are shown next to their corresponding energy levels indicated by line segments. Cyan colored line segments represent the transition states leading to the formation of either a O_2 molecule (left) or a carbonyl-pair species (right). 52

22 Pair-wise association energy of hydroxyl groups on graphene. Same as Figure 21; cyan colored segments indicate the transition states to the formation of a H_2O molecule and an epoxide species. 52

23 Pair-wise association energy of an epoxide and a hydroxyl group on graphene. Same as Figure 21; cyan colored segments indicate the transition states leading to proton transfer between neighboring hydroxyl and epoxide species. . 52

24 Role of O-H bond orientation on the association energy of two neighboring hydroxyl species. Left panel, energy profile obtained from NEB-DFT calculations of two -OH groups in ortho-position whose O-H bonds undergo rotations in the plane parallel with the graphene layer. Optimized atomic configurations of the two stable configurations and the transition state are shown next to their corresponding energy points indicated by red discs. Right panel, stable configurations of two -OH groups in para-position showing different relative orientations of O-H bonds by DFT calculations. All the energy values are referred to that of two isolated -OH groups on graphene. 54

25 Association energy of single-layer graphene with epoxide-only (red), hydroxyl-only (blue), and mixed epoxide-hydroxyl (cyan) functionalizations as computed by both DFT (ΔE) and the simplistic energy scheme ($\Delta E^{(2)}$). Filled and empty symbols refer to crystalline structures, and small clusters of trimeric and tetrameric oxygen species on graphene, respectively. Selected model structures are shown as insets and on the right side. Full information is reported in Figure 26. 55

26 Association energies per oxygen species obtained by DFT (black) and the simplistic energy scheme based on Equation (122) (blue) for single-layer graphene with (a) epoxide-only, (b) hydroxyl-only, and (c) mixed epoxide-hydroxyl functionalizations. Models of crystalline structures (enclosed in dashed boxes) have O:C ratios of – from left to right – in (a) 0.25, 0.375, 0.5 and 0.5; in (b) 0.5, 0.75, and 1.0; and in (c) 0.75 and 0.67, with hydroxyl:epoxide ratios of 2:1 and 1:1, respectively. 55

27 The stable configurations of an epoxide (red sphere) and a hydroxyl group (blue sphere) on graphene lattice. The four nearest-neighbor stable sites are marked by orange spheres for the epoxide group. The three nearest-neighbor stable sites are marked by cyan spheres for the hydroxyl group. 56

28 (a) Total square displacement vs. Monte Carlo steps of epoxide groups on a lattice model during the melting process at T=5000 K. The system is considered to be completely melted when the average displacement per oxygen species is over half of the supercell dimension. (b) Energy of a EGO model calculated by Equation (122) vs. T during the quenching process. 57

29 (a) ΔG (per oxygen species) of single-layer graphene with epoxide functionalization. Black and red symbols show ΔG of hand-made structures calculated by DFT (Equation (125)), and EGO models generated by Monte Carlo simulations (Equation (126)), respectively. Selected EGO models from MC simulations are shown as insets: red and yellow discs represent -O- groups facing upward and downward the graphene plane, respectively; the graphene lattice is not shown. The black filled disc is evaluated by Equation (126) using the model structure shown in Figure 30(a). (b) Same as (a) for hydroxyl-functionalized graphene. In the insets, -OH species facing upward and downward the graphene plane are shown in blue and cyan, respectively. The black filled disc is evaluated using the model structure shown in Figure 30(b). (c) ΔG of mixed epoxide-hydroxyl functionalized graphene by MC simulations, with O:C ratios of 0.3 (magenta) and 0.4 (cyan). Insets show selected models with an O:C ratio of 0.4 and different relative fractions of -OH and -O- groups (OH/O refers to the fraction of -OH groups relative to the total amount of oxygen). 59

30 Crystalline structure of graphene fully covered by (a) epoxide and (b) hydroxyl groups. Dashed boxes indicate the primitive unit cells. These two phases are found to be most energetically favored in the proposed single-layer GO models [108, 128]. 59

31 (a) Schematic energy diagram of the binary reaction from two epoxide groups embedded in highly oxidized domains in aged EGO. ΔG (per oxygen species) of reactants and products correspond to the averages extracted from the aged EGO models with epoxide-functionalization generated by Monte Carlo simulations. (b) Same as (a) in the case of two hydroxyl groups embedded in highly oxidized regions of aged EGO with hydroxyl-functionalization. The activation energies are extracted from NEB-DFT calculations based on the models in Figure 32. 60

32 Single-layer EGO models generated by DFT. (a) A EGO model with an O:C ratio of 0.42 (fractions of hydroxyl and epoxide groups are 0.17 and 0.25, respectively). (b) A EGO model with an O:C ratio of 0.25 including epoxide groups only. The dashed frames indicate the supercell used in DFT calculations. Colored ellipses show selected pairs of oxygen species, which are eligible for the reactions to form O_2, H_2O (cyan), and a carbonyl-pair (blue), for computing the energy barriers using the NEB method. 61

33 NEB-DFT calculations of reactions in EGO models in Figure 32: (a) Two -OH groups forming a H_2O molecule and an -O- group. (b), (c), (e) and (f) Two -O- groups forming a O_2 molecule. (d) Two -O- groups forming a carbonyl pair. Line segments show the energy levels of reactants (black), transition state (cyan), and products (red). The corresponding energy values (in black) are shown below the line segments. Blue dashed line segments and energy values in blue indicate the energy of products estimated by the simplistic energy scheme based on Equation (122). All the energies are referred to that of the initial state in each case. 62

34 A EGO model generated by the DFT-D scheme, presenting a homogeneous lateral distribution of oxygen functionalities, with an O:C ratio of 0.46, fractions of epoxide and hydroxyl groups equal to 0.08 and 0.28, respectively, and a water content of 10%. The optimized structure shows an average interlayer spacing of 7.3 Å. Right panel, selected region of the EGO model showing a large concentration of hydroxyl groups and water molecules. 66

35 (a) Schematic representation of a multilayer EGO film consisting of non-homogeneously oxidized regions rich in hydroxyl species (red regions), and connected by trapped water molecules. (b) In-plane structure of aged EGO generated by Monte Carlo simulation as described in Chapter IV, with an O:C ratio of 0.38, and fractions of hydroxyl and epoxide species equal to 0.27 and 0.11, respectively. The dashed box indicates the supercell used in the simulation with dimensions of about 5 nm. 67

36 Periodic model structures of EGO films fully oxidized with hydroxyl groups including increasing amount of water. First panel on the left shows the in-plane structure of these models. The colored dashed rectangles indicate the planar dimensions of the supercells for the EGO models including 6.25% (blue), and 0%, 12.5% and 25% (green) of water. The optimized interlayer distances by DFT-D are reported on top of each model. In the case of the hydrated EGO models, the (zero-temperature and zero-pressure) enthalpy difference per water molecule (ΔE) between the hydrated and dehydrated structures is also reported. The structures on the left and right side present "type 1" and "type 2" stacking geometries, respectively. 68

37 Same as Figure 36, for EGO models containing epoxide functionalities. . . . 68

SUMMARY

Graphene oxide (GO) holds great promise for applications in nanoelectronics, optics, nanomechanics, sensors, and energy storage. GO is commonly obtained from graphite via a harsh chemical oxidation process, followed by several other solution processing steps. The whole synthesis method leads to lamellar oxide films with a very complex microstructure, whose physical chemical properties are difficult to fully characterize, understand, and hence control. In my thesis work, I used and developed atomistic computer simulations to investigate the thermochemical and structural properties of a particular form of ultrathin GO films. These oxide films are obtained by chemical oxidation of multilayer epitaxial graphene grown on silicon carbide, they present a very uniform layered structure consisting of a stack of large-area oxidized graphene sheets and a minimal amount of edge defects, and thereby they represent model films to be used for fundamental studies of GO; in this thesis work, these oxide films are referred to as EGO. The motivation of this thesis work thus lies in the importance of GO in both basic science and technology, and its goal has been achieving a detailed atomistic understanding of a selected form of GO films, i.e. multilayer EGO on SiC substrates.

Multilayer EGO films are only a few nanometers in thickness, they exhibits a complex and, to a large extent, an unknown chemical composition and structure, and X-ray photoelectron spectroscopy, X-ray diffraction, and Infrared spectroscopy experiments show the occurrence of puzzling behaviors and properties. After the synthesis at room temperature, the EGO films exhibit the occurrence of slow aging processes, encompassing structural and chemical changes. Furthermore, in spite of the moderate amount of water detected in the lamellar structure, the interlayer spacing in EGO is unexpectedly found to be around 10 Å. In my thesis work, I used density functional theory calculations to generate model structures of EGO and to calculate X-ray photoelectron spectroscopy spectra. Also, I used this type of calculations to first investigate the diffusion, interaction, and reaction of oxygen/hydrogen

functional groups on graphene, and second, to devise a simplified energy scheme describing the energy of arbitrary oxygen functionalizations of graphene. This simple energy scheme was used in combination with a lattice-model Monte Carlo simulation to mimic the aging process of EGO. The above numerical simulations and developments have led me to elucidate the origin and mechanism underlying the metastable behaviors of EGO, its interlayer and intralayer structure, and to clarify the relation between water content, interlayer spacing, and spatial distribution of oxygen functionalities.

In this thesis, importance, applications, and synthesis of the EGO films are described in Chapter I. Experimental observations and open questions are also discussed in Chapter I. Chapter II reports on basic concepts of density functional theory, as well as technical aspects related to its numerical implementation. Results and discoveries of my studies are reported in detail in Chapter III, IV, and V.

CHAPTER I

INTRODUCTION

Graphene is a two-dimensional carbon material with exceptional electronic, optical, and mechanical properties. Synthesized for the first time in 2004 [9, 84], graphene nowadays holds great promise in a variety of technological applications. In particular, graphene is a candidate replacement material in traditional transistor devices [37, 102], as well as the base material to develop novel nanoelectronics. Unfortunately, graphene has no energy gap, and to control its electronic transport properties, and therefore to enable its implementation in digital logic devices, solutions are being sought to open a bandgap in this material. So far, four possible directions have been pursued: nanostructuring to exploit quantum confinement effects [48], biasing bilayer graphene [133], strain-induced bandgap opening [45], and chemical functionalization [46]. The most important and widely studied functionalization of graphene has been with oxygen. In this thesis, I employed computational methods based on density functional theory to investigate the structure and chemical properties of graphene films grown epitaxially on silicon carbide oxidized by using a chemical method.

1.1 Graphene and its chemically modified forms

1.1.1 Structure, properties and applications

Graphene is a two-dimensional (2D) crystalline material consisting of a single layer of carbon atoms arranged in a honeycomb lattice. The unit cell of graphene contains two C atoms, and is defined by lattice vectors $\mathbf{a}_1 = a(\frac{\sqrt{3}}{2}, \frac{3}{2})$ and $\mathbf{a}_2 = a(-\frac{\sqrt{3}}{2}, \frac{3}{2})$, with $a = 1.42$ Å (Figure 1(a)). The 2s, $2p_x$ and $2p_y$ orbitals of each C hybridize in the sp^2 configuration and form tight σ bonds with three nearest-neighbor C atoms, resulting in a robust carbon network. The remaining $2p_z$ orbitals form a band of delocalized electronic states, which control the electronic transport properties of this material. The energy dispersion of the π band can be described by a tight-binding Hamiltonian [121], yielding – under the assumption of only nearest- and next-nearest-neighbor coupling between $2p_z$ orbitals – the following analytical result:

$$\begin{aligned} E(\mathbf{k}) &= \pm t\sqrt{3 + f(\mathbf{k})} - t' f(\mathbf{k}) \ , \\ f(\mathbf{k}) &= 2\cos(\sqrt{3}k_y a) + 4\cos(\frac{\sqrt{3}}{2}k_y a)\cos(\frac{3}{2}k_x a) \ , \end{aligned} \tag{1}$$

where t and t' are the nearest- and next-nearest- neighbor hopping energies, respectively. The plus and minus signs correspond to the upper (electron) and lower (hole) bands, respectively (Figure 1(b)).

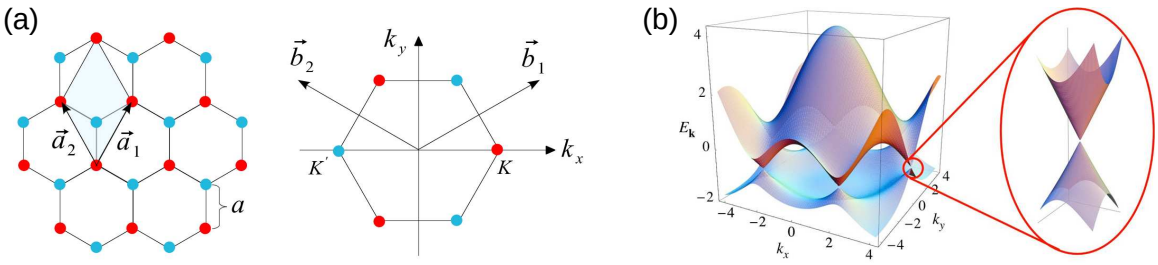

Figure 1: (a) Graphene real-space lattice structure (left) and Brillouin zone (right). Red and blue circles indicate sublattices A and B, respectively. Lattice vectors $\mathbf{a}_1$ and $\mathbf{a}_2$, reciprocal lattice vectors $\mathbf{b}_1$ and $\mathbf{b}_2$, and the Dirac points $\mathbf{K}$ and $\mathbf{K}'$ are indicated. (b) Electronic dispersion in the honeycomb lattice [82]. Left: energy spectrum (in unit of t) for finite values of t and t', with t=2.7 eV and t'=-0.2t. Right: zoom in of the energy bands close to one of the Dirac points.

The irreducible region of the Brillouin zone of graphene contains two non-equivalent corners $\mathbf{K}$ and $\mathbf{K}'$, called the Dirac points. The valence band and conduction band of graphene intersect at the Dirac points, rendering graphene a gapless semimetal. Close to $\mathbf{K}$ and $\mathbf{K}'$, Equation (1) can be approximated by

$$E(\mathbf{q}) \approx \pm v_F \mathbf{q} \ , \tag{2}$$

where $\mathbf{q}$ is the momentum relative to the Dirac points and v_F is the Fermi velocity; with t'=0, v_F assumes the value of $3ta/2 \approx 10^6$ m/s. This linear energy-momentum relation shows the effective mass of electrons and holes near the Fermi energy is zero. Electrons and holes at low energy behave as "zero-mass" relativistic particles whose motion must therefore be described by the Dirac equation.

Graphene has a remarkably high electron mobility μ at room temperature. Experiments show that μ can exceed 15000 cm^2/Vs with carrier concentrations up to 10^{13} cm^2, and temperature-resolved transport measurements reveal that μ is limited by scattering with impurities and intrinsic defects [39]. The conical band structure gives rise to unique optical properties. Despite being only one atom thick, graphene absorbs a significant fraction (about 2.3%) of light [81]. It is possible to see graphene without the use of a microscope. Graphene has a number of other exceptional properties, arising from the σ bonding between the C atoms. It has a Young's modulus of $\sim$ 1 TPa and a breaking strength of $\sim$42 N/m [70], over 100 times greater than a hypothetical steel film of the same thickness. Graphene has high thermal conductivity up to 5000 W/mK at room temperature [7], and therefore is an excellent candidate material for heat removal. Finally, graphene has a negative thermal expansion coefficient of about -6$\times 10^{-6}$/K, which is an important property to be considered in controlling thermal stress in graphene-based devices [129].

The unique properties of graphene can be exploited in a variety of technologies. In addition to be a potential replacement for silicon in conventional field effect transistors

(FET), graphene is being considered, in the place of indium tin oxide, as transparent conducting electrodes in displays, touch screens, solar cells, and organic light-emitting diodes [25, 122]. Doping or chemical modification of graphene have been proposed as ways to control light absorption in graphene, and hence to use it in novel optical modulator [75] and electrochromic devices [63]. Graphene is sensitive to the chemical environment (absorption of gas molecules and biomolecules can change the resistance of graphene), and is suitable for sensing technologies [99]. Graphene-made nanopores are being explored for rapid and inexpensive electronic DNA sequencing [127]. Furthermore, the extraordinary thinness and stiffness of graphene make it promising in electromechanical applications such as nanomechanical resonators for ultralow mass detection and ultrasensitive force and charge sensors [16], and piezoresistive pressure sensors [109]. Finally, graphene has great potential as an energy storage material in batteries or supercapacitors. Single and multilayer graphene used as anodes in lithium batteries exhibit much larger reversible specific capacity than graphite [74, 92]. Graphene or functionalized graphene used as electrodes in supercapacitors possesses even more advantages for its enormous surface area per unit mass, and it has been shown to yield both large energy and power density, as well as excellent cycle stability [132].

1.1.2 Epitaxial graphene on SiC

Currently, four methods are most commonly used to prepare graphene: exfoliation of graphite by "scotch tape" [84], chemical vapor deposition of graphene on metals [73], reduction of graphene oxide obtained from oxidizing graphite [27], and epitaxial growth of graphene on silicon carbide (SiC) [9]. In this thesis, I studied the oxide of this latter form of graphene.

To grow epitaxial graphene (EG), 4H-SiC or 6H-SiC substrates are heated at temperatures higher than 1200 °C in either vacuum or an inert atmosphere [35]. Si atoms desorb from the surface of SiC, and the remaining C atoms rearrange and crystallize, leading to the formation of graphene layers. Graphene films exhibit different properties depending on the termination of SiC from which they are grown. To date, epitaxial graphene has been obtained by heating SiC substrates exposing either the Si-face (0001) or C-face ($000\bar{1}$) of SiC.

High quality EG grown on the Si-face of SiC is usually prepared by introducing one atmosphere of argon into the ultra-high vacuum (UHV) system [28]. The resulting EG films consist of a "buffer layer" [29, 95] showing the $(6\sqrt{3} \times 6\sqrt{3})R30^\circ$ surface reconstruction in contact with SiC, and a few-layer thick graphene film on top of it (Figure 2). These EG films are electron-doped due to the interaction with substrate [35], and decoupling can be achieved by intercalating hydrogen or other species between the buffer layer and SiC [42, 94]. Monolayer EG exhibits the characteristic linear electronic band structure near the Fermi level, with modest mobility of about 1000 cm^2/Vs [22]. Multilayer EG films are

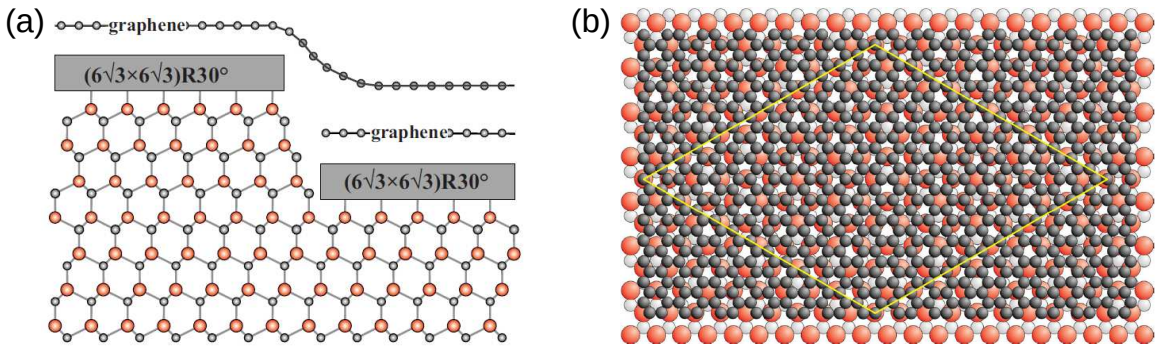

Figure 2: (a) Schematic layer structure of epitaxial graphene on Si-face 6H-SiC [69]. (b) A monolayer graphene on the bulk-truncated Si-face SiC surface. The large diamond indicates the unit cell of the $(6\sqrt{3} \times 6\sqrt{3})R30°$ reconstruction [29].

Bernal stacked: bilayer EG shows parabolic bands and the band structure evolves to that of graphite with increasing thickness [137]. Consequently, multilayer EG on the Si-face of SiC is actually ultrathin graphite film.

Growth of graphene on the C-face of SiC is carried out in UHV and it is faster than that on the Si-face. The growth process leads to multilayer EG of 10 to 20 layers exhibiting either a disordered stacking structure – many rotational domains rather than the simple "AB" stacking [35] – or a unique layer-stacking structure [22]. These latter samples have adjacent graphene layers rotated with respect to the $(21\bar{3}0)$ direction in SiC by 30° and $\pm \sim 7°$ [50] (Figure 3). Bernal stacked layers make up less than 15% of the film with this particular stacking structure [111]. The rotational faults decouple the graphene sheets, such that they behave as isolated graphene monolayers and therefore the EG film shows a linear band structure [112] and ultrahigh mobilities exceeding 250000 cm^2/Vs at room temperature [87].

Graphitization of SiC allows one to grow large-area of high-quality graphene films with both the single- and multi-layer geometry. In addition, growth of sidewall graphene nanoribbons on a specific SiC facet has recently advanced to the point that narrow ribbons down to ~ 1.4 nm can be made with very well-defined edges and bandgaps up to 0.5 eV [53]. The development of these techniques is an important step toward the ultimate goal of producing integrated epitaxial graphene circuits.

1.1.3 Chemically modified graphene

Chemical modification of graphene offers a promising path to tailor the properties of graphene, for instance, opening a bandgap and therefore enabling electronic applications [26], enhancing its chemical compatibility with other materials such as dielectric layers in FET devices [124], and tuning the work function of graphene to optimize charge-injection barriers for using it as electrodes in solar cells and light-emitting diodes [104]. To date,

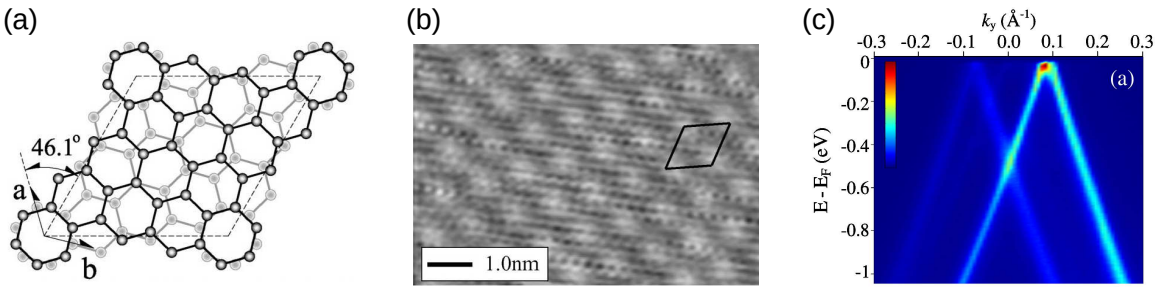

Figure 3: Rotational stacking faults in multilayer epitaxial graphene (MEG) on C-face SiC. (a) Schematic $(\sqrt{13} \times \sqrt{13})R46.1°$ unit cell alignment of two graphene sheets [50]. (b) Scanning tunneling microscopy image of the moiré superlattice on the top layer of a nominally 10-layer MEG sample [50]. (c) Angle-resolved photoemission spectroscopy of band structure of an 11-layer graphene film grown on C-face 6H-SiC measured at 6 K. The wavevector scan is perpendicular to the SiC $(10\bar{1}0)$ at the **K** point. Two linear Dirac cones are visible [112].

chemical functionalization of graphene has been obtained by using oxygen [25], hydrogen [110], fluorine [96] and larger functional groups such as nitrophenyl [83, 98], through a variety of functionalization methods. In this thesis, I studied epitaxial graphene on SiC oxidized by a chemical solution method known as "Hummers method".

Before entering the core of my thesis, it is worth to briefly describe conventional graphene oxide (GO), a carbon material having a long history [12], many potential applications, and for this reason extensively studied [26, 106]. The conventional method to produce GO relies on the chemical oxidation of bulk graphite, the subsequent exfoliation of graphite oxide sheets, and the deposition of the GO platelets on a substrate [25]. The resulting material has a lamellar structure, with carbon sheets buckled due to the presence of oxygen functionalities predominantly epoxide (-O-) and hydroxyl (-OH) groups, and the edges decorated by oxygen species such as carbonyl (=O) and carboxyl (-OOH) groups [72]. GO is hygroscopic and it is capable of trapping large quantities of water molecules in the galleries of its lamellar structure [15]. The interlayer distance is found to range from 4 Å to 12 Å depending on the water content [71, 77]. The oxidation level (O:C ratio), fractions of each chemical species and their spatial distributions on the layer vary depending on synthesis, processing, and environmental conditions.

GO possesses intriguing properties and potential applications in nanoelectronics, optics, catalysis, nanomechanics, and energy storage [20, 24, 25, 76, 138].

1.2 Oxidized epitaxial graphene

Conventional GO contains – due to the exfoliation process and the multiple steps involved in its synthesis – a significant amount of defects [30, 80, 100]. In recent years, alternative

approaches have been explored to produce high-quality graphene oxide materials with controlled chemical and physical properties [55, 120, 123]. These novel forms of graphene oxide present a similar chemistry as conventional GO, but due to the strong effect of the synthesis procedure, they also show different structural and physical properties. Here, I relied on a selected set of experiments to elucidate at the atomic scale the structure and properties of oxidized epitaxial graphene (EGO).

1.2.1 Synthesis of EGO

EGO is obtained from EG by using the so-called Hummers oxidation method [60, 62]. In brief, a EG film is first dipped into H_2SO_4/ $NaNO_3$ solution placed in an iced water bath. Then, $KMnO_4$ is added to the solution, and the mixture is transferred to a 35 °C water bath for about 20 minutes. Deionized (DI) water (23 ml) is slowly added to the mixture. Finally, after 15 min, warm DI water (70 ml) and H_2O_2 (1.5 ml) are added to the mixture to terminate the reaction. The EGO sample is brought to air, rinsed with DI water, and dried in high-purity nitrogen gas.

1.2.2 Experimental information

EGO films with thicknesses ranging from 6 to 20 layers were characterized by using optical imaging, atomic force microscopy (AFM), Raman spectroscopy, Kelvin probe force microscopy (KPFM), UHV 4-point transport measurement, X-ray photoelectron spectroscopy (XPS), X-ray diffraction spectroscopy (XRD), and Infrared spectroscopy (IR) techniques. These experiments show that the EGO films are homogeneous, uniform, and insulating, they include a minimal amount of holes or edges, and the spatial distribution of oxygen species on the graphene layers presents some level of disorder. In particular, XPS (Figure 4(a)) shows that the predominant oxygen functionalities chemisorbed on the graphene layers in EGO are epoxide and hydroxyl groups (peak around 286.7 eV), and carbonyl or other edge oxygen species (binding energies larger than 289 eV) are present in very little amounts. The peak arising from non-oxidized C atoms is around 284.7 eV. Furthermore, XPS spectra of EGO taken at increasing aging times show that these oxide films are unstable at room temperature. According to spectral analysis, in particular, as-synthesized EGO films have O:C ratios of about 0.44, while aged EGO films present O:C ratios of about 0.38, indicating the occurrence of significant chemical reduction over a period of about one month. Moreover, the spectral analysis shows that, in addition to spontaneous reduction, the EGO films undergo significant structural changes with a longer life-time of about two months. These interesting experimental findings open the following questions:

1. What are the exact fractions of epoxide and hydroxyl groups (and possibly water species) in EGO? How do they change in time?

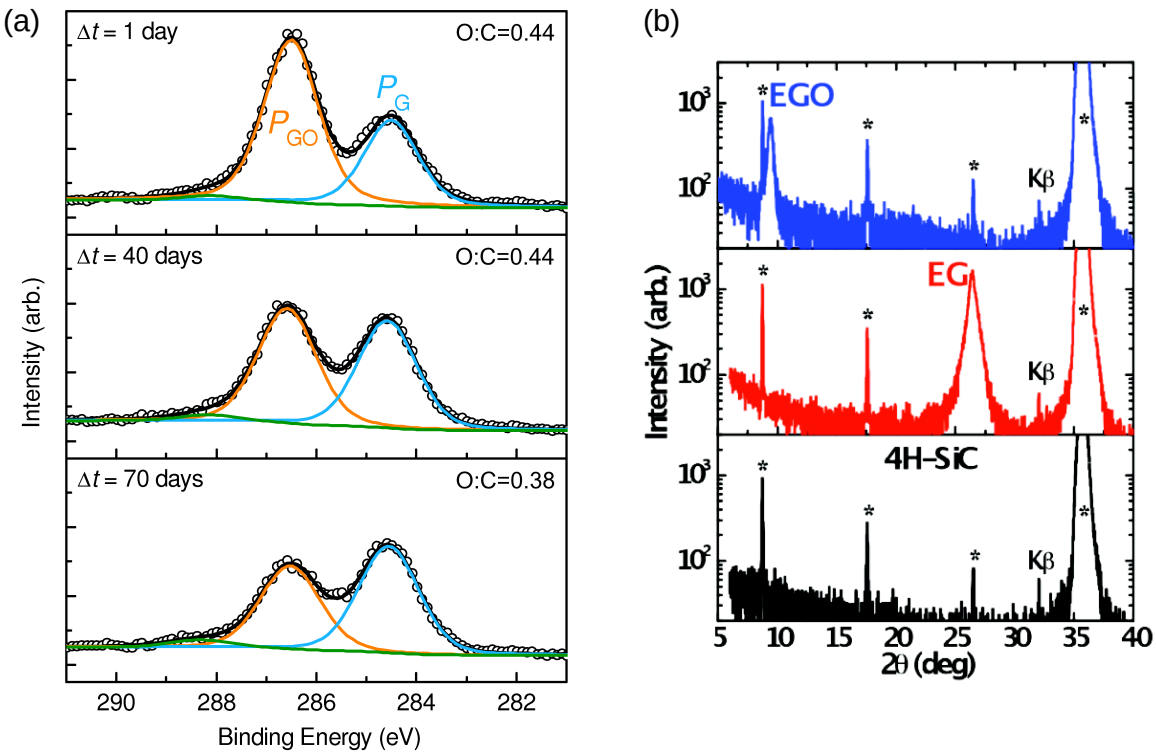

Figure 4: (a) Experimental C 1*s* XPS spectra of EGO films at increasing aging times at room temperature: 1 day, 40 days and 70 days after their synthesis. The three fitted components are assigned to unoxidized C (blue), C-O-C and C-OH (orange), and C=O (green). (b) XRD ω-2θ spectra of an 11($\pm$1)-layer EGO film (blue), a 12($\pm$1)-layer EG film (red), and a bare 4H-SiC (000$\bar{1}$) substrate (black). The asterisks refer to the peaks of the substrate.

2. What is the spatial distribution of these functionalities on the graphene layers? How does it change in time?

3. What is the mechanism underlying the metastable characteristics shown by the XPS spectra?

4. At room temperature, what is driving the structural (and possibly the chemical) changes in EGO?

5. Is aged EGO in air a chemically stable material?

The XRD and AFM measurements reveal that the EGO films aged at room temperature for several months acquire a multilayer structure whose quality is comparable to that of pristine EG films. Most interestingly, the XRD spectra (Figure 4(b)) shows that the interlayer distance of EGO is about 9.5 Å. This extraordinary large interlayer spacing does not change after heating the films up to temperatures of 140 °C, nor it does after drying the oxide films in N_2 for one night. The IR measurements also suggest the water content

in EGO is below 10% (with respect to the total number of C atoms). These interesting experimental findings open the following questions:

1. What is the origin of the large interlayer distance in aged EGO?

2. What is the vertical structure of the multilayer EGO films?

1.3 Thesis outline

In my thesis, I focused on the XPS and XRD measurements of EGO described above and I used density functional theory calculations to interpret the experimental results and elucidate the structural properties of EGO. To achieve a full understanding of the structure and chemical stability of EGO, I also developed a lattice-model-based Monte Carlo (MC) scheme to mimic the aging process of EGO layers and determine the quasi-equilibrium structure and free energy of the oxidized carbon layers. The goal of my thesis has been addressing the questions listed above.

The next chapter introduces density functional theory. Chapter III focuses on interpretation of the XPS spectra shown in Figure 4(a), and clarifying the fundamental questions arising from them. Chapter IV reports on an extensive DFT and MC study to unravel the intralayer structure and chemical stability of EGO. Chapter V focuses on interpretation of the XRD spectra of EGO shown in Figure 4(b), and elucidating the questions arising from them. In the last chapter, I summarize my thesis work and the main results that I have obtained, and propose possible future directions and development of my work.

CHAPTER II

DENSITY FUNCTIONAL THEORY

Density functional theory (DFT) is to date one of the most widely used methods to study the properties of molecules and solids from first principles. DFT treats the electron charge density, instead of the wavefunction, as the fundamental variable to solve the electronic quantum mechanical many-body problem. DFT was conceptually introduced by Thomas and Fermi [115], and in 1964 it was given a firm theoretical footing by Hohenberg and Kohn [54], who proved that the properties of a material or a molecular system are uniquely determined by the ground state electron density. One year later, Kohn and Sham [65] devised a simple method for finding the electron density through the use of an auxiliary system of non-interacting electrons confining the many-body effects in an exchange-correlation energy functional. In recent years, approximations of the exchange and correlation energy have been progressively improved, allowing DFT to achieve a high accuracy in descriptions of many classes of solid state systems at a relatively low computational cost.

In this chapter, I will briefly discuss the basic concepts, formalism, and a numerical implementation of density functional theory.

2.1 The electron many-body problem

The Hamiltonian of atoms, molecules or solids that contains M nuclei and N electrons – considering these nuclei and electrons as non-relativistic particles – can be written as follows:

$$\begin{aligned}\hat{H} &= -\frac{1}{2}\sum_{i=1}^{N}\nabla_i^2 - \frac{1}{2}\sum_{A=1}^{M}\frac{1}{M_A}\nabla_A^2 - \sum_{i=1}^{N}\sum_{A=1}^{M}\frac{Z_A}{r_{iA}} + \sum_{i>j}^{N}\frac{1}{r_{ij}} + \sum_{A>B}^{M}\frac{Z_A Z_B}{R_{AB}} \\ &= \hat{T}_e(\mathbf{x}) + \hat{T}_N(\mathbf{R}) + \hat{V}_{eN}(\mathbf{x},\mathbf{R}) + \hat{V}_{ee}(\mathbf{x}) + \hat{V}_{NN}(\mathbf{R}) \ ,\end{aligned} \tag{3}$$

where the first two terms are the kinetic energies of electrons and nuclei, respectively; the last three terms are the electrostatic potential between electron-nucleus, electron-electron and nucleus-nucleus, respectively. All the quantities are in atomic units. $\mathbf{x} = \{\mathbf{x}_1, \mathbf{x}_2, \cdots, \mathbf{x}_N\}$ and $\mathbf{R} = \{\mathbf{R}_1, \mathbf{R}_2, \cdots, \mathbf{R}_M\}$ represent the coordinates for all the electrons and nuclei, respectively. In principle, the wavefunction of a system can be obtained by solving the Schrödinger equation:

$$\hat{H}\Psi(\mathbf{x}_1, \mathbf{x}_2, \cdots, \mathbf{x}_N, \mathbf{R}_1, \mathbf{R}_2, \cdots, \mathbf{R}_M) = E_{tot}\Psi \ . \tag{4}$$

However, this task is impossible to carry out in practice, except for very small systems. The reason is that the wavefunction contains 3(N+M) degrees of freedom, and all the particles

are coupled by the Coulomb interactions. It is computational costly to calculate the energy and the structure even for a molecule consisting of a few atoms.

Equation (4) is largely simplified by the use of the Born-Oppenheimer approximation, which states that since the electrons are much lighter than the nuclei, the electrons response almost instantaneously to any change in the nuclear positions. In this approximation, the wavefunction of a system is written as:

$$\Psi(\mathbf{x}, \mathbf{R}) = \Phi(\mathbf{x}; \mathbf{R})\chi(\mathbf{R}) \ , \tag{5}$$

where $\Phi(\mathbf{x}; \mathbf{R})$ is the electronic wavefunction that depends parametrically on the nuclear positions. $\chi(\mathbf{R})$ is the nuclear component. Assuming a fixed nuclear configuration, it is possible to show that

$$[\hat{T}_e + \hat{V}_{ee}(\mathbf{x}) + \hat{V}_{eN}(\mathbf{x}, \mathbf{R})]\Phi_n(\mathbf{x}; \mathbf{R}) = E_n(\mathbf{R})\Phi_n(\mathbf{x}; \mathbf{R}) \ , \tag{6}$$

where the electronic eigenvalues $E_n(\mathbf{R})$ allow to construct the so-called "Born-Oppenheimer surfaces". For each energy surface, the nuclear wavefunctions can be then obtained from:

$$[\hat{T}_N + \hat{V}_{NN}(\mathbf{R}) + E_n(\mathbf{R})]\chi(\mathbf{R}) = E_{tot}\chi(\mathbf{R}) \ , \tag{7}$$

which gives information about the vibrational, rotational and translational motions of the nuclear system.

The ground state of electrons under a certain nuclear configuration can be found by the variational method, i.e. choosing a trial electronic wavefunction depending on a set of parameters, and varying these parameters such that the expectation value of the energy given by

$$E(\Phi) = \frac{\langle \Phi | \hat{H} | \Phi \rangle}{\langle \Phi | \Phi \rangle} \tag{8}$$

is minimal. Here the Hamiltonian has the form of that one in Equation (6). The wavefunction defined by such parameters is approximately the ground state electronic wavefunction, and the corresponding energy is the ground state energy. The Hartree-Fock and related methods write the trial wavefunctions as single Slater determinants:

$$\Phi(\mathbf{x}_1, \mathbf{x}_2, \cdots, \mathbf{x}_N) = \frac{1}{\sqrt{N!}} \begin{vmatrix} \phi_1(\mathbf{x}_1) & \phi_2(\mathbf{x}_1) & \cdots & \phi_N(\mathbf{x}_1) \\ \phi_1(\mathbf{x}_2) & \phi_2(\mathbf{x}_2) & \cdots & \phi_N(\mathbf{x}_2) \\ \vdots & \vdots & \ddots & \vdots \\ \phi_1(\mathbf{x}_N) & \phi_2(\mathbf{x}_N) & \cdots & \phi_N(\mathbf{x}_N) \end{vmatrix} \ , \tag{9}$$

where $\{\phi_i(\mathbf{x}_j)\}_{i,j=1}^N$ are the one-electron wavefunctions. An alternative way for treating the problem is to write the energy as a functional of electron density, and to minimize the energy functional. The electron charge density is associated to the wavefunctions via

$$n(\mathbf{r}) = \int |\Phi(\mathbf{r}, \mathbf{x}_2, \cdots, \mathbf{x}_N)|^2 d\mathbf{x}_2 \cdots d\mathbf{x}_N \ , \tag{10}$$

and it depends on only 3 spatial coordinates. This leads to another family of methods – density function theory.

2.2 The Hohenberg-Kohn theorems

The core of DFT is the two Hohenberg-Kohn theorems (H-K). According to Equation (6), the Hamiltonian of electrons can be written as

$$\hat{H} = (\hat{T}_e + \hat{V}_{ee}) + \hat{V}_{eN} = \hat{F} + \hat{V}_{ext} \ , \tag{11}$$

where $\hat{T}_e$, $\hat{V}_{ee}$, and $\hat{V}_{eN}$ are – as defined above – the kinetic energy of electrons, electron-electron Coulomb interaction, and electron-nucleus interaction, respectively. $\hat{F} = \hat{T}_e + \hat{V}_{ee}$ is an universal operator and is identical for all the systems containing the same number of electrons. $\hat{V}_{ext} \equiv \hat{V}_{eN}$ is hereafter referred to as the external potential. The Hamiltonian is completely determined by the number of electrons N and the external potential.

The first H-K theorem states that the ground state electron density uniquely determines the external potential V_{ext} and thus all properties of the system. The proof is straightforward: suppose two external potentials V_{ext}^1 and V_{ext}^2 differ by more than a constant and they give rise to the same electron density $n(\mathbf{r})$. The two potentials are associated to distinct Hamiltonians $\hat{H}_1$ and $\hat{H}_2$, and wavefunctions Φ_1 and Φ_2. According to the variational principle, only the ground state wavefunction gives the lowest energy, such that

$$E_1 = \langle \Phi_1 | \hat{H}_1 | \Phi_1 \rangle < \langle \Phi_2 | \hat{H}_1 | \Phi_2 \rangle \ . \tag{12}$$

Assuming a non-degenerate ground state, the inequality strictly holds. As the two Hamiltonians are related to an identical ground state density, there is

$$\begin{aligned} \langle \Phi_2 | \hat{H}_1 | \Phi_2 \rangle &= \langle \Phi_2 | \hat{H}_2 | \Phi_2 \rangle + \langle \Phi_2 | \hat{H}_1 - \hat{H}_2 | \Phi_2 \rangle \\ &= E_2 + \int [V_{ext}^1(\mathbf{r}) - V_{ext}^2(\mathbf{r})] n(\mathbf{r}) d\mathbf{r} \ . \end{aligned} \tag{13}$$

Exchanging the subscripts, one can also write

$$\langle \Phi_1 | \hat{H}_2 | \Phi_1 \rangle = E_1 + \int [V_{ext}^2(\mathbf{r}) - V_{ext}^1(\mathbf{r})] n(\mathbf{r}) d\mathbf{r} \ . \tag{14}$$

Adding Equation (13) and (14), and according to Equation (12), one obtains

$$E_1 + E_2 < E_2 + E_1 \ , \tag{15}$$

which is clearly a contradiction.

Since the ground state density $n(\mathbf{r})$ uniquely determines all the properties of the system including the total energy, the ground state energy can be written as a functional of $n(\mathbf{r})$ via

$$E[n] = \langle \Phi | \hat{F} + \hat{V}_{ext} | \Phi \rangle = F[n] + \int V_{ext}(\mathbf{r}) n(\mathbf{r}) d\mathbf{r} \tag{16}$$

with

$$F[n] = \langle\Phi|\hat{T}_e|\Phi\rangle + \langle\Phi|\hat{V}_{ee}|\Phi\rangle = T_e[n] + E_{ee}[n] \ , \tag{17}$$

where $T_e[n]$ is the kinetic energy functional of electrons, and $E_{ee}[n]$ is the electron-electron Coulomb interaction functional. The second H-K theorem states that the exact ground state electron density minimizes the energy functional E[n]. The proof is also trivial: suppose $n'(\mathbf{r})$ is an electron density other than the ground state one, associated to the wavefunction Φ'. By using the variational principle for the wavefunctions, there is

$$E[n] = \langle\Phi|\hat{H}|\Phi\rangle < \langle\Phi'|\hat{H}|\Phi'\rangle = E[n'] \ . \tag{18}$$

Therefore evaluation of E[n] at the ground state electron density yields the lowest energy value.

The H-K theorems are the basis of density functional formalism, and lay the groundwork for finding the ground state of a many-electron system via electron density. A direct variation of E[n] leads to

$$\frac{\delta}{\delta n(\mathbf{r})}\left[E[n(\mathbf{r})] - \mu\left(\int n(\mathbf{r})d\mathbf{r} - N\right)\right] = 0 \ , \tag{19}$$

where μ is the Lagrange multiplier associated with the constraint that the number of electrons N is conserved. Based on Equation (16), the corresponding Euler equation is therefore given by

$$\mu = \frac{\delta F[n(\mathbf{r})]}{\delta n(\mathbf{r})} + V_{ext}(\mathbf{r}) \ . \tag{20}$$

The universal functional $F[n(\mathbf{r})]$ can be written as

$$F[n(\mathbf{r})] = T_e[n] + E_H[n] + E_{nc}[n] \ , \tag{21}$$

where the Coulomb potential functional $E_{ee}[n]$ defined in Equation [17] is split into a classical term $E_H[n]$ due to the electrostatic interaction between electron clouds and equal to

$$E_H[n(\mathbf{r})] = \frac{1}{2}\int\int \frac{n(\mathbf{r})n(\mathbf{r}')}{|\mathbf{r}-\mathbf{r}'|}d\mathbf{r}d\mathbf{r}' \tag{22}$$

and a non-classical term $E_{nc}[n]$ equal to the difference between $E_{ee}[n]$ and $E_H[n]$.

2.3 The Kohn-Sham formalism

The difficulty of using Equations (19) – (21) lies on the fact that the kinetic energy functional and the non-classical term can not be written explicitly, as the electrons interact and their motion is correlated. A more practical approach for applying the H-K theorems was established by Kohn and Sham, who introduced the use of a fictitious system of non-interacting electrons to represent the ground state electron density $n(\mathbf{r})$ of the real interacting electrons system. The ground state wavefunction of this non-interacting system

is taken to be a single determinant of one-electron orbitals $\{\phi_i(\mathbf{r})\}_{i=1}^N$ (the KS orbitals, i denotes both the spatial and spin quantum numbers), with each orbital occupied by one electron, such that

$$n(\mathbf{r}) = \sum_{i=1}^{N} |\phi_i(\mathbf{r})|^2 \ . \tag{23}$$

Each electron is regarded as moving in an effective potential $V_{eff}(\mathbf{r})$, and satisfying the single-particle Schrödinger equations:

$$\left[-\frac{\hbar^2}{2m}\nabla^2 + V_{eff}(\mathbf{r})\right]\phi_i(\mathbf{r}) = \epsilon_i\phi_i(\mathbf{r}) \ . \tag{24}$$

$V_{eff}(\mathbf{r})$ can be determined by rewriting the energy functional as

$$E[n(\mathbf{r})] = T_s[n] + E_H[n] + E_{xc}[n] + \int V_{ext}(\mathbf{r})n(\mathbf{r})d\mathbf{r} \ , \tag{25}$$

where $T_s[n]$ is the kinetic energy functional of the non-interacting system. $E_{xc}[n]$ is called the exchange-correlation functional including all the unknown parts, and equals to

$$E_{xc}[n] = T_e[n] - T_s[n] + E_{ee}[n] - E_H[n] \ . \tag{26}$$

The universal functional F[n] is thus given by

$$F[n(\mathbf{r})] = T_s[n] + E_H[n] + E_{xc}[n] \ , \tag{27}$$

and Equation (20) now becomes

$$\mu = \frac{\delta T_s[n(\mathbf{r})]}{\delta n(\mathbf{r})} + V_{eff}(\mathbf{r}) \ , \tag{28}$$

where the effective potential $V_{eff}(\mathbf{r})$ for the non-interacting system equal to

$$V_{eff}(\mathbf{r}) = V_{ext}(\mathbf{r}) + V_H(\mathbf{r}) + V_{xc}(\mathbf{r}) \tag{29}$$

with the classical electrostatic term – Hartree potential – given by

$$V_H(\mathbf{r}) = \frac{\delta E_H[n(\mathbf{r})]}{\delta n(\mathbf{r})} = \int \frac{n(\mathbf{r}')}{|\mathbf{r}-\mathbf{r}'|}d\mathbf{r}' \tag{30}$$

and the exchange-correlation potential defined as

$$V_{xc}(\mathbf{r}) = \frac{\delta E_{xc}[n(\mathbf{r})]}{\delta n(\mathbf{r})} \ . \tag{31}$$

Obviously the electron density has to be known beforehand to calculate $V_{eff}(\mathbf{r})$, and the Kohn-Sham equations yield single-electron orbitals which in turn will satisfy this electron density. Therefore the Kohn-Sham scheme usually works in a self-consistent way: one starts with an initial guess for $n(\mathbf{r})$, and calculate the corresponding $V_{eff}(\mathbf{r})$ by using the formula (29) – (31); then solves the Kohn-Sham equations to obtain ϕ_i, and evaluate the new electron density via Equation (23). The iterations proceed until the output and input electron densities are identical within a certain numerical tolerance.

2.4 Local density and generalized gradient approximations of DFT

The major problem of applying Kohn-Sham DFT is that the exact exchange-correlation functional is not known except for the free electron gas. Kohn and Sham proposed that [65] if the electron density is sufficiently slowly varying, the exchange-correlation energy at a point $\mathbf{r}$ is simply equal to the exchange-correlation energy of a homogeneous electron gas (HEG) that has the same density at the point $\mathbf{r}$, such that

$$E_{xc}[n] = \int n(\mathbf{r})\epsilon_{xc}(n(\mathbf{r}))d\mathbf{r} \ , \tag{32}$$

where $\epsilon_{xc}(n)$ is the exchange-correlation energy per electron of HEG with density $n(\mathbf{r})$. This approximation uses only the local density to define $E_{xc}[n]$, and thus is called the local density approximation (LDA). Correspondingly there is

$$V_{xc}(\mathbf{r}) = \frac{\delta E_{xc}[n(\mathbf{r})]}{\delta n(\mathbf{r})} = \epsilon_{xc}(n) + n\frac{d\epsilon_{xc}(n)}{dn} \ . \tag{33}$$

$E_{xc}[n]$ is usually split into the exchange part and the correlation part:

$$E_{xc}[n] = E_x[n] + E_c[n] \ , \tag{34}$$

with the exchange functional $E_x[n]$ given by a simple analytic form for HEG based on the work by Dirac [23]:

$$E_x[n] = -\frac{0.458}{r_s} \ , \tag{35}$$

where r_s is the radius of a sphere containing one electron and given by $(4\pi/3)r_s^3 = 1/n$. For the correlation part, accurate values for $E_c[n]$ have been determined by Ceperly using Quantum Monte-Carlo techniques [14]. By interpolating these values, Perdew and Zunger [90] provide a simple expression for $E_c[n]$ as

$$\begin{aligned} E_c[n] &= A\ln r_s + B + Cr_s\ln r_s + Dr_s \ , \qquad r_s \le 1 \\ &= \gamma/(1+\beta_1\sqrt{r_s} + \beta_2 r_s) \ , \qquad r_s > 1 \end{aligned} \tag{36}$$

where r_s is defined as the above. The coefficient A, B, C, D, γ, β_1 and β_1 have been obtained for both the spin-polarized and spin-unpolarized homogeneous electron gas. LDA yields good results in geometries of molecules and solids, bulk moduli, and phonon frequencies within a few percent errors; it is less accurate in predicting ionization energies and cohesive energies with typical errors of 10-20%. LDA fails completely for highly correlated systems which are dominated by electron-electron interactions [64].

The generalized gradient approximation (GGA) gives a semi-local form of $E_{xc}[n]$ to incorporate the effects of inhomogeneities in electron density by applying gradient corrections, such that

$$E_{xc}[n] = \int n(\mathbf{r})\epsilon_{xc}(\mathbf{r})F[(n(\mathbf{r}), \nabla n(\mathbf{r})]d\mathbf{r} \ , \tag{37}$$

where ϵ_{xc} is taken from the HEG model; $F[(n(\mathbf{r}), \nabla n(\mathbf{r})]$ is an enhancement factor, depending on both local density and local gradient of density. Many works have been done to derive successful GGA of form (37), based on first principles calculations, or employing experimental data for parameterizations. Commonly used GGA functionals include PW91 proposed by Perdew and Wang [91], and PBE by Perdew, Burke and Ernzerhof [89]. GGA shows improvement over LDA in atomic energies and binding energies, and accounts for hydrogen bond, at a modest additional computational cost.

There are also many other types of functionals such as meta-GGA that includes the second derivative of electron density, and hybrid functional which incorporates a portion of exact exchange component from Hartree-Fock theory, and they show high precisions in particular cases. In summary, LDA and its improvements provide fairly good enough description of the exchange and correlation energies for large classes of systems, and enable DFT to be used for exploring the properties of these materials.

2.5 Technical and numerical aspects

2.5.1 Plane-wave basis set

To solve the Kohn-Sham equation, the one-electron wavefunction has to be expanded in a suitable basis set as

$$\phi_n(\mathbf{r}) = \sum_{i=1}^{M} c_{n,i}\psi_i(\mathbf{r}) \ , \tag{38}$$

where ϕ_n is the nth Kohn-Sham orbital and $\{\psi_i\}_{i=1}^{M}$ is the basis set. In molecular calculations, an atomic basis set is commonly used, which consists of a finite number of atomic orbitals with Gaussian form $e^{-\alpha r^2}$ or Slater form $e^{-\alpha r}$. For condensed matter systems, plane-wave basis is more suitable for describing infinite periodic structures. According to Bloch's theorem, the wavefunction of an electron in a periodic potential can be written as

$$\phi_{n,\mathbf{k}}(\mathbf{r}) = e^{i\mathbf{k}\cdot\mathbf{r}} u_{n,\mathbf{k}}(\mathbf{r}) \ , \tag{39}$$

where n is the band index, $\mathbf{k}$ is the wavevector, and $u_{n,\mathbf{k}}(\mathbf{r})$ is a function with the same periodicity of the potential, such that $u_{n,\mathbf{k}}(\mathbf{r}) = u_{n,\mathbf{k}}(\mathbf{r}+\mathbf{R})$, with $\mathbf{R}$ representing the lattice vector. Consequently $u_{n,\mathbf{k}}(\mathbf{r})$ can be expanded in a Fourier series:

$$u_{n,\mathbf{k}}(\mathbf{r}) = \sum_{\mathbf{G}} c_{n,\mathbf{G}}(\mathbf{k}) e^{i\mathbf{G}\cdot\mathbf{r}} \ , \tag{40}$$

where $\mathbf{G}$ is reciprocal lattice vectors defined by $\mathbf{G}\cdot\mathbf{R} = 2\pi m$ (m is an integer). The corresponding electron wavefunction is thus given by

$$\phi_{n,\mathbf{k}}(\mathbf{r}) = \sum_{\mathbf{G}} c_{n,\mathbf{k}+\mathbf{G}} e^{i(\mathbf{k}+\mathbf{G})\cdot\mathbf{r}} \ . \tag{41}$$

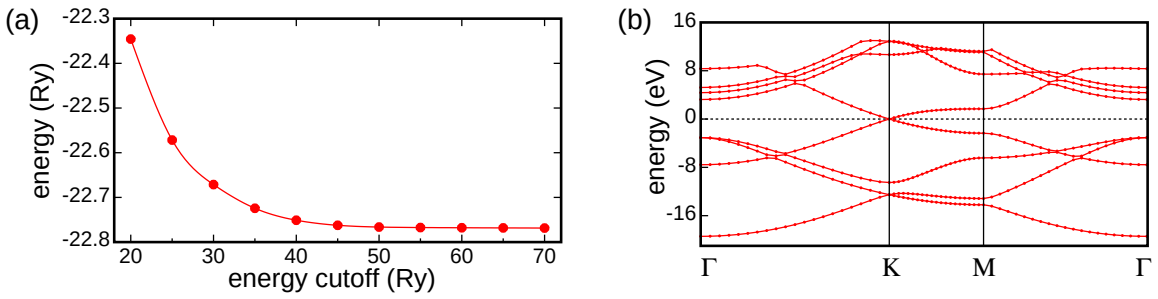

Figure 5: (a) DFT total energy vs. energy cutoff for graphene. (b) Electronic band structure of graphene calculated by DFT. Graphene in (a) and (b) is represented by its primitive unit cell, with a lattice constant of 2.47 Å. The Brillouin zone is sampled by a uniform 48×48×1 **k** point mesh.

The Kohn-Sham effective potential also has the lattice periodicity, and can be represented as

$$V_{eff}(\mathbf{r}) = \sum_{\mathbf{G}} \tilde{v}_{eff}(\mathbf{G}) e^{i\mathbf{G}\cdot\mathbf{r}} \ , \tag{42}$$

where $\tilde{v}_{eff} = \tilde{v}_{ext} + \tilde{v}_H + \tilde{v}_{xc}$. It is easy to show that such plane-wave expansions lead to a very simple form of Kohn-Sham equation:

$$\sum_{\mathbf{G}'} \left[\frac{1}{2} |\mathbf{k}+\mathbf{G}|^2 \delta_{\mathbf{G},\mathbf{G}'} + \tilde{v}_{eff}(\mathbf{G}-\mathbf{G}') \right] c_{n,\mathbf{k}+\mathbf{G}'} = \epsilon_n c_{n,\mathbf{k}+\mathbf{G}} \ , \tag{43}$$

which reduces the effort to a matrix diagonalization problem.

A complete plane-wave basis set includes infinite number of plane waves and is impossible to use in practice. Instead one can apply a set of plane waves which are restricted in a sphere in reciprocal space with a radius related to a cutoff energy E_{cut}, such that

$$\frac{\hbar^2}{2m} |\mathbf{k}+\mathbf{G}|^2 \leq E_{cut} \ . \tag{44}$$

This cutoff value and the volume of the supercell Ω determine the number of plane waves N_{PW} that will be used via

$$N_{PW} \sim \Omega E_{cut}^{\frac{3}{2}} \ . \tag{45}$$

Figure 5(a) shows an example of the convergence of the energy of graphene as the energy cutoff is varied.

Bloch's theorem allows one to consider only the electrons within a unit cell of solids. The energy values of ϵ_n as a function of **k** obtained by Equation [43] directly give the electronic band structure of the system (Figure 5(b) shows the band structure of graphene as an example.). Properties such as electron density and total energy are then computed by adding the contributions from – in principle – a infinite number of **k** vectors in the Brillouin zone. As wavefunctions vary slowly over small distances in **k**-space, the integrations can be performed as summations over certain finite and discrete **k** points. To appropriately sample

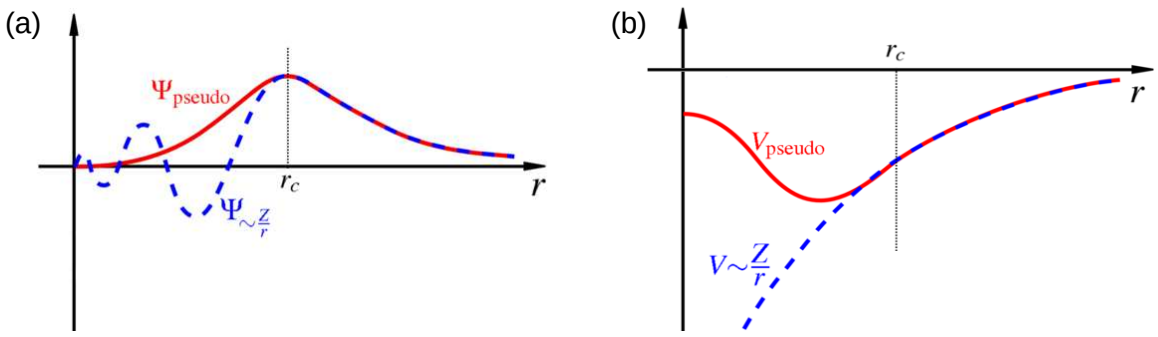

Figure 6: (a) Schematic illustration of all-electron wavefunction (blue) vs. pseudo wavefunction (red). (b) Nuclear Coulomb potential (blue) vs. pseudopotential (red).

the Brillouin zone, it is important to know how fast the integrand changes with respect to **k**. For metals, the energy dramatically vary in the region where the valence bands cross the Fermi level, thereby requiring a dense **k** mesh for description. For semiconductors and insulators, the electronic bands are relatively flat, and a uniform grid with a small number of **k** points is generally enough.

2.5.2 Pseudopotentials

A difficulty of using plane-wave basis is that electron wavefunctions rapidly oscillate in the core region, due to the strong Coulomb interaction and the orthogonality condition between the core states and valence states, which require a large number of plane waves for a precise description. To overcome this obstacle, we consider the facts that core electrons are tightly bound to nuclei and respond very little to the presence of neighboring atoms, while valence electrons strongly interact with the environment and dominate the physical properties of materials. Thus, core electrons can be viewed as frozen and forming together with nuclei as rigid non-polarizable ion cores; valence electrons feel this effective potential – pseudopotential [101], and are described by a set of pseudo wavefunctions with no radial nodes in the core region, as illustrated in Figure 6. The pseudopotential and pseudo wavefunctions are identical to the real ones outside a radius cutoff r_c. The smoothness of pseudo wavefunctions near the core dramatically reduce the number of plane waves needed for representation. When solving the Kohn-Sham equation, only valence electrons have to be treated explicitly. Therefore the pseudopotential technique can be used with both atomic basis and plane-wave basis set for saving computational efforts.

One of the most widely used methods for pseudopotential generation is based on first principles calculations [36]. The so-called norm-conserving pseudopotential is generated according to the following procedures:

(1) Perform an all-electron self-consistent DFT calculation for a free atom to obtain the ground state eigen-energies and wavefunctions by solving the Kohn-Sham equation. It

can be proved that the effective potential $V_{eff}(\mathbf{r})$ in the Kohn-Sham equation is spherically symmetric, such that the one-electron wavefunction can be split into a radial part and an angular part:

$$\phi_i(\mathbf{r}) = \frac{u_{nl}(r)}{r} Y_{lm}(\Omega) \ , \tag{46}$$

where n,l and m are the principle, angular, and magnetic quantum numbers, respectively. $Y_{lm}(\Omega)$ are the normalized spherical harmonics. It is easy to show the radial Kohn-Sham equation – for the nonrelativistic case – is given by

$$-\frac{\hbar^2}{2m}\frac{d^2u_{nl}(r)}{dr^2} + \left[\frac{\hbar^2}{2m}\frac{l(l+1)}{r^2} + V_{eff}(r) - \epsilon_{nl}\right] u_{nl}(r) = 0 \ . \tag{47}$$

The eigen-energies ϵ_{nl} and radial wavefunctions $u_{nl}(r)$ can thus be solved according to Equation (47).

(2) Construct radial pseudo wavefunctions for valence states to obtain a intermediate screened pseudopotential. The pseudo wavefunctions $u^{ps}_{nl}(r)$ are derived from the all-electron wavefunctions for valence states, such that

1. u^{ps}_{nl} and u_{nl} have the same eigen-energies:

$$\epsilon^{ps}_{nl} = \epsilon_{nl} \ . \tag{48}$$

2. u^{ps}_{nl} and u_{nl} have the same amplitude beyond the core cutoff radius r_c:

$$\phi^{ps}_{nl}(r) = \phi_{nl}(r) \quad for \quad r > r_c \ . \tag{49}$$

3. u^{ps}_{nl} is normalized, which implies the norm-conservation constraint:

$$\int_{r<r_c} |u^{ps}_{nl}(r)|^2 dr = \int_{r<r_c} |u_{nl}(r)|^2 dr \ . \tag{50}$$

4. The pseudo wavefunction contains no radial nodes.

The pseudo wavefunctions can be shown to satisfy a Schrödinger equation:

$$(\hat{H} + \hat{V}_{nl}) u^{ps}_{nl}(r) = \epsilon_{nl} u^{ps}_{nl}(r) \ , \tag{51}$$

where $\hat{H}$ is the Hamiltonian in the radial Kohn-Sham equation for the all-electron wavefunction. $\hat{V}_{nl}$ is a non-local potential given by

$$\hat{V}_{nl} = \sum_{n'l'}^{core} (\epsilon_{nl} - \epsilon_{n'l'}) |\chi_{n'l'}\rangle\langle\chi_{n'l'}| \ , \tag{52}$$

with $|\chi_{n'l'}\rangle$ representing the all-electron wavefunction for the core states. The screened pseudopotential is obtained by inverting Equation (51) with the created pseudo wavefunctions:

$$\begin{aligned} V^{scr}_{nl,tot}(r) &= V_{eff}(r) + V_{nl}(r) \\ &= \epsilon_{nl} - \frac{\hbar^2}{2m}\frac{l(l+1)}{r^2} + \frac{\hbar^2}{2m}\frac{1}{u_{nl}(r)}\frac{d^2u_{nl}(r)}{dr^2} \ . \end{aligned} \tag{53}$$

(3) The final pseudopotential is obtained by subtracting from the screened pseudopotential the electrostatic and the exchange-correlation contributions due to the valence electrons:

$$V^{ps}_{nl,tot}(r) = V^{scr}_{nl,tot}(r) - V_H(\rho^{ps}; r) - V_{xc}(\rho^{ps}; r) \ , \tag{54}$$

where ρ^{ps} is the valence electron density evaluated from the pseudo wavefunctions.

2.6 Dispersion interactions and DFT

The commonly used exchange-correlation functionals such as LDA and GGA do not describe the long-range dispersion interactions correctly [44]. Dispersion interactions arise from the attractions between two instantaneous dipole moment induced by electron oscillations, and have an asymptotic -1/R^6 dependence on the interatomic or intermolecular distance R. Dispersion interactions play an important role in the structures and hence define the properties of many chemical systems, such as layered crystals, molecular clusters, DNA and proteins.

To model multilayer graphene oxide, it is necessary to account for dispersion interactions. I adopted the semi-empirical dispersion-corrected DFT approach (hereafter referred to as DFT-D) [8, 43, 49]. In particular, an atom pairwise term describing the dispersion interactions is simply added to the total energy of the system, such that

$$E_{DFT-D} = E_{DFT} + E_{disp} \tag{55}$$

with

$$E_{disp} = -\frac{1}{2}\sum_{i,j} C_6^{i,j}[\sum_{\mathbf{R}} |\mathbf{r}_{i,j} + \mathbf{R}|^{-6} f_{damp}(|\mathbf{r}_{i,j} + \mathbf{R}|)] \ , \tag{56}$$

where E_{DFT-D} and E_{DFT} are the total energies given by DFT-D and DFT schemes, respectively. $\mathbf{r}_{ij}$ is the distance vector between atom i and j, $\mathbf{R}$ is the lattice vector, and C_6^{ij} is the dispersion coefficient for atom pair i and j. Damping function f_{damp} is used to avoid near-singularities for small $\mathbf{R}$, and determine the range of the dispersion force, which is given by

$$f_{damp}(|\mathbf{r}_{i,j} + \mathbf{R}|) = s_6 \cdot \{1 + exp[-d \cdot (\frac{|\mathbf{r}_{i,j} + \mathbf{R}|}{r_0} - 1)]\}^{-1} \ , \tag{57}$$

where s_6 is a global scaling factor depending only on the exchange-correlation functionals, r_0 is a cutoff radius over which the contribution to E_{disp} is negligible, and d is a global constant defining the steepness of the correction at small $\mathbf{R}$. I adopt parameters C_6^{ij} proposed by Grimme [43], $s_6 = 0.75$ and $d = 20$ for PBE functionals optimized by Barone [8], and r_0=100 Å.

To validate this method, I performed calculations on two reference systems: graphite and a water dimer. For graphite, I used a supercell containing four graphene layers in "AB" stacking, and 5 × 6 graphene unit cell for each layer. The Brillouin zone is sampled at Γ point. The optimized lattice parameters, computed bulk modulus and interlayer binding

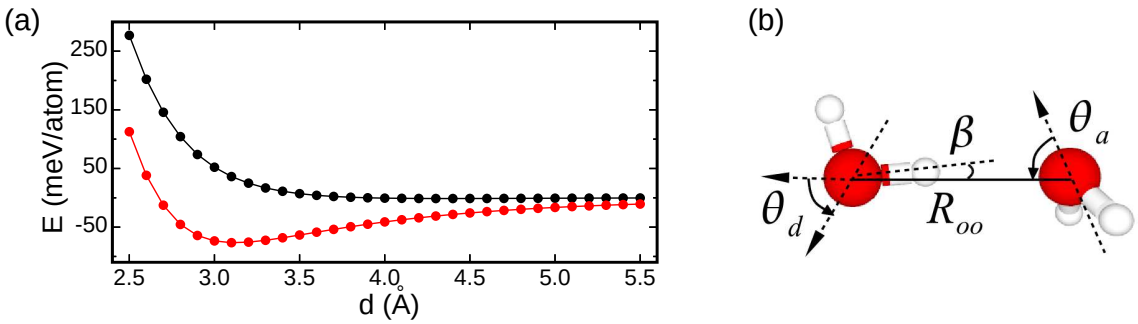

Figure 7: (a) Interlayer binding energy vs. interlayer distance in graphite calculated by DFT (black) and DFT-D (red) schemes. (b) Model structure of a water dimer. The values of geometrical parameters R_{oo}, β, θ_a, and θ_b obtained by DFT and DFT-D are reported in Table 2.

Table 1: Lattice parameters (a and c), bulk modulus (B), and interlayer binding energy (E_b) of graphite. Present results obtained by DFT and DFT-D are compared to the experimental values and results from other calculations.

	a(Å)	c(Å)	B(GPa)	E_b(meV/atom)
DFT	2.47	8.77	2	1
DFT-D	2.47	6.44	47	55
PBE [8]	2.46	9.62	1	1
PBE-D [8]	2.46	6.43	46	54
PW91-D [8]	2.45	6.69	–	83
VdW-DF [97]	2.47	7.52	12	24
Expt.	2.46 [57]	6.65 [57]	41 [38]	52 [130]

energy are reported in Table 1, compared with the results from DFT calculation, as well as theoretical and experimental values from literature. The energy curves as a function of interlayer distance in graphite are shown in Figure 7(a). Results show that inclusion of the dispersion correction provides the interlayer binding and stabilizes the system. The DFT-D curve (red) shows an energy minimum at about 3.22 Å and binding energy of 55 meV per C atom, in good agreement with experiment. The bulk modulus is obtained by fitting the energy curve (Figure 7(a)) with a Birch equation of state [10], and the calculated value is also close to the experimental value. The energies given by DFT (black) approach zero at large distances due to the absence of attraction, and thus overestimates the interlayer distance.

In the case of a water dimer, the two molecules interact via a hydrogen bond – the proton of one water molecule attracts the lone pair of the O of the other water molecule. Hydrogen bonds are stronger than dispersion interactions, and are treated in some degree in the semi-local GGA functionals [44]. Table 2 reports the geometrical parameters and binding energy of a water dimer calculated by DFT and DFT-D. The improvement of the

Table 2: Geometrical parameters and binding energy (E_0) of a water dimer. Present results obtained by DFT and DFT-D schemes are compared to the experimental values. E_0 is referred to the energy of two isolated water molecules in vacuum.

	R_{oo}(Å)	θ_a(°)	θ_d(°)	β(°)	E_0 (kcal/mol)
DFT	2.945	62.8	-57.4	5.3	-2.58
DFT-D	2.957	61.9	-56.3	4.3	-3.09
Expt.[21, 85]	2.976	57±10	-51±10	2±10	-5.4±0.7

results by DFT-D scheme over DFT is not as much as that for extended systems such as solids and biomolecules. Nevertheless, DFT complemented with the dispersion correction describes very well the long-range attractions, which is essential for correctly modeling multilayer graphene oxide systems.

2.7 Technical details of my DFT calculations

In this thesis, DFT calculations were carried out by using the QUANTUM-Espresso toolkit [41]. I adopted the generalized gradient approximation proposed by Perdew, Burke, and Ernzerhof (PBE) for the exchange-correlation functional. I used a plane-wave basis set with energy cutoff of 70 Ry, and norm-conserving pseudopotentials generated by the fhi98PP package [36] for all atomic species. For molecular systems (section 3.1.3), and disordered systems requiring large supercells for descriptions, I performed Γ point calculations by using the CP code of the QUANTUM-Espresso package. In particular, single-layer graphene oxide models are used in section 3.2.4, 4.2.1, 4.2.2, and section 4.2.3.4, represented by a orthorhombic supercell consisting of 5 × 6 graphene unit cells in the xy plane, and a vacuum region of 12 Å in the z direction. Periodic multilayer graphene oxide models are used in section 3.2.1 and section 5.1, represented by a supercell consisting of 4 graphene layers in "AB" stacking geometry, and each layer including 5 × 6 graphene unit cells. For solid systems with crystalline structures (section 4.2.3.1 and section 5.2), I chose the primitive unit cell for each case as the supercell, with a 3 × 3 × 3 Γ-centered uniform **k**-point mesh sampling the Brillouin zone, and I used the PWscf code of the QUANTUM-Espresso package for the calculations. Structural optimizations were performed by relaxing both the electronic and cell degrees of freedom. Self-consistent electronic iterations proceeded until the energy difference less than 2×10^{-7} eV. The ionic minimization was performed until the energy difference less than 0.002 eV and the forces on each atom less than 0.05 eV/Å. The performance of the pseudopotentials and convergence of the parameters were tested in advance.

CHAPTER III

CHEMICAL COMPOSITION AND STABILITY OF EGO FILMS

In this chapter, I will first introduce X-ray photoelectron spectroscopy (XPS) technique, the basic physics process, and methods for computing core-level shifts. Then I will address the questions opened by the experimental XPS results on the oxidized epitaxial graphene films.

3.1 X-ray photoelectron spectroscopy

X-ray photoelectron spectroscopy is a nondestructive technique that has been widely used for studying properties of atoms, molecules and solids. The technique involves irradiating a specimen with a flux of nearly monoenergetic X-ray photons, and measuring the kinetic energy and intensity of electrons that are ejected into the vacuum. The basic components of XPS instrument include a X-ray tube, an electron energy analyzer, an electron detector system, and the specimen in a UHV chamber (Figure 8(a)).

3.1.1 Basic concepts

The basic process of interest in XPS is the "photoelectric effect", a phenomenon discovered in 1887 by Heinrich Hertz and explained in 1905 by Albert Einstein. Invested by X-ray electromagnetic radiation, the core electrons in a material absorb the quantized energy $h\nu$ carried by the incident photons, and are emitted from the material, such that

$$A + h\nu \rightarrow A^+ + e^- \ , \tag{58}$$

where A and A^+ represent the neutral and ionized atom in the material before and after photoemission, respectively. ν is the photon frequency, and e^- is the emitted electron, also called "photoelectron". Conservation of energy requires that

$$E(A) + h\nu = E(A^+) + E_{kin}(e^-) \ , \tag{59}$$

where the energy of the photoelectron is present in the form of kinetic energy E_{kin}. E_{kin} depends on the photon energy, and the energy of the atomic (molecular) orbital level that the electron occupied prior the photoemission process. The binding energy of a core electron in the kth orbital level is thus defined as the energy difference between the ionized and neutral atom:

$$E_b^V(k) = E(A^+) - E(A) \ . \tag{60}$$

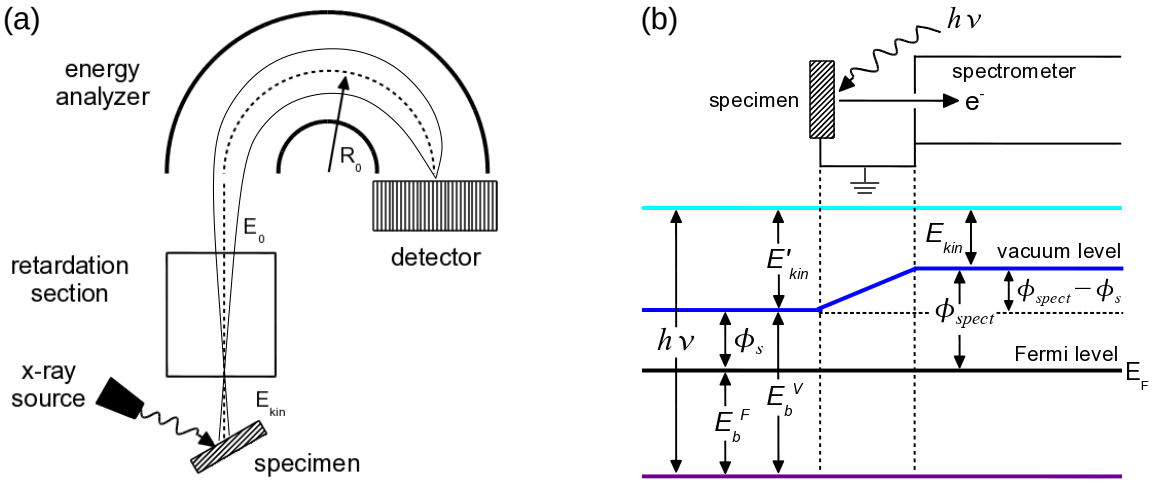

Figure 8: (a) Basic components of a XPS spectrometer system, including radiation source, specimen, electron energy analyzer, and detector. (b) Energy diagram of a metallic specimen in electrical equilibrium with a XPS spectrometer. The kinetic energy of photoelectrons are measured in the spectrometer, where the vacuum level may be different from that in the UHV chamber. Thus $E_b^V(k)$ can not be directly acquired. For gas phase molecules, $E_b^V(k)$ is obtained by measuring the kinetic energy of photoelectrons relative to that of a standard species with a precisely known ionization potential [126]. For solids, no such standards are available, and the binding energy is most commonly referred to the Fermi level of the specimen [13], which is in electrical contact with the spectrometer. For metallic materials, both Fermi levels are at equal energies. The Fermi-level referred binding energy $E_b^F(k)$ is given by $E_b^F(k) = h\nu - E_{kin} - \phi_{spect}$, where E_{kin} is the kinetic energy measured in the spectrometer; ϕ_{spect} is the work function of the spectrometer. The vacuum-referred binding energy $E_b^V(k)$ can be obtained by $E_b^V(k) = E_b^F(k) + \phi_s$, once the work function of the specimen ϕ_s is known. For semiconductors and insulators, the Fermi level is not well defined. The specimen may carry net charges as emitted photoelectrons are not replaced by electrons from the ground. Usually low energy electrons are used to flood the specimen to insure charge equilibrium.

This leads to the most commonly used photoelectric equation:

$$E_{kin} = h\nu - E_b^V(k) \ . \tag{61}$$

As each element has a set of characteristic core-level binding energy values, the measured distribution of photoelectrons with respect to the kinetic energy can be used to probe the elemental composition as well as the chemical state of the elements of a material. For solids, photoelectrons undergo inelastic scattering when traveling through the material toward the surface. The number of photoelectrons escaping a solid decays exponentially with depth increases, and typically only the top ∼10 nm of a material in contact with vacuum can be detected.

The core-electron binding energy in Equation (60) is commonly thought to arise from the initial-state and final-state effects. The initial-state effect considers a system upon photoemission (from the kth orbital level) having the remaining electrons "frozen" in their original states. In this first-order approximation, the binding energy $E_b^i(k)$ can be written as

$$E_b^i(k) = E^i(N-1,k) - E^i(N) \ , \tag{62}$$

where $E^i(N)$ is the energy of the initial system consisting of N electrons, and $E^i(N-1,k)$ is the energy of the system after photoemission, including a core-hole in the kth subshell and (N-1) electrons in the same "orbitals" as the initial system. After this initial stage of photoemission, the remaining electrons will relax, leading to the so-called "final-state effect". The wavefunctions and charge distributions of these electrons will be adjusted to decrease the energy of the final system $E^f(N-1,k)$. The binding energy $E_b^V(k)$ can thus be written as

$$E_b^V(k) = E_b^i(k) - E_{relax} \ , \tag{63}$$

where E_{relax} is the relaxation energy and equals to $E^i(N-1,k) - E^f(N-1,k)$. E_{relax}, though a second-order correction to the initial-state effect, has significant consequences in interpreting XPS data such as chemical shifts. As the whole process occurs on a time scale much shorter than that of the nuclear motion ($\sim 10^{-16}$ s compared to $\sim 10^{-13}$ s), the nuclear positions can be viewed as identical before and after photoemission [13].

3.1.2 Calculations of core-level shifts

Core-level shift or chemical shift is the change in the binding energy of a core electron of an element due to a change in the local chemical environment of the element [13]. For instance, Si in a silicon crystal and SiO_2 gives rise to a $2p$ binding energy of 99 eV and 102.3 eV, respectively. An element on the surface of a material may also have a core-level binding energy difference from that in the bulk due to the different coordination number [88]. Measurement of XPS core-level shifts has become one of the most widely used tools

for diagnosing oxidation states and local chemical and physical environment of elements in surface analysis. Many theoretical efforts have been made to interpret and calculate XPS chemical shifts [4, 19].

The point charge model is a very simple method to explain XPS chemical shifts. It was introduced by Siegbahn and Fadley, and it is based purely on classical electrostatics [33, 34]. The main idea is to evaluate the changes in the electrostatic potential in the core of an atom due to the changes of the valence electron density. The model considers only the influence of the oxidation state of the probed atoms on the chemical shift (the initial-state effect). It neglects the perturbations to the remaining electrons in the system caused by the removal of a core electron by photoemission (the final-state effect). In this method, an atom A is modeled as a hollow sphere of radius r_A with its surface uniformly charged by Q valence electrons. The potential energy of a core electron inside the sphere is given by

$$V = \frac{-eQ}{r_A} \ , \tag{64}$$

and the removal of an amount of charge from the valence shell equal to q_A will give rise to a chemical shift of

$$\Delta E_b = \frac{q_A e^2}{r_A} \ . \tag{65}$$

In case there are other ions close to the atom A, the chemical shift becomes

$$\Delta E_b = \frac{q_A e^2}{r_A} - \sum_C \frac{q_C e^2}{R_{AC}} \ , \tag{66}$$

where R_{AC} is the distance between an ion C and the atom A, and q_C is the amount of charge carried by this ion. According to this model, withdrawal (addition) of valence electrons will decrease (increase) the shielding of the nuclear charge, and thus increase (decrease) the core-level binding energy. Also chemical shifts for molecules or solids will be less than that of a free ion due to the additional shielding from electrons of atoms nearby [126]. Equation (66) can be used to estimate chemical shifts for a number of systems [33], and it achieves a certain degree of agreement with experiment.

3.1.2.1 Hartree-Fock method

A modern method to calculate core-level binding energies is through the direct computation of the energies of the initial state $E^i(N,k)$ and the final state $E^f(N-1,k)$. Relative chemical shifts can be obtained by taking the difference of binding energies of atoms at inequivalent sites (labeled by 1 and 2), as

$$\Delta E_b^V(k) = [E^f(N-1,k)_1 - E^i(N,k)_1] - [E^f(N-1,k)_2 - E^i(N,k)_2] \ . \tag{67}$$

The Hartree-Fock method is one of the most widely used methods for such calculations. In this method, the N-electron wavefunction is approximated by a single Slater determinant

of N one-electron orbitals. To compute $E^f(N-1,k)$, the wavefunction of the final core-hole state can be characterized as having a hole in the kth subshell, and be calculated self-consistently. In this way, both the initial-state and final-state effects are accounted. This approach has been used for determining binding energies and chemical shifts for atoms, small molecules and inorganic clusters, and provides results in fairly good agreement with experiment [59]. These calculations are computationally costly and are not suitable for large systems like solids.

A simple treatment is to consider only the initial-state effect, such that the wavefunctions of the remaining (N-1) electrons are instantaneously unchanged; and assume the orbital for the kth-subshell hole is the same as the initial one-electron orbital where photoemission occurs. The total energy of the initial system is given by the Hartree-Fock energy [114]:

$$E^{HF}(N) = \sum_{i=1}^{N} \epsilon_i - \frac{1}{2} \sum_{i,j} [J_{i,j} - K_{i,j}] \ , \tag{68}$$

where ϵ_i is the orbital energy of the ith level. $J_{i,j}$ and $K_{i,j}$ arise from two-electron integrals, and are related to Coulomb and exchange energies, respectively. With the above two assumptions, the ionized system with a kth-subshell hole has an energy of $E^{HF}(N-1,k)$ given by the same formula as $E^{HF}(N)$, with the index k eliminated from the summations in Equation (68). It is not difficult to show the binding energy is just equal to the negative of the kth orbital energy, leading to the Koopmans' Theorem [13]:

$$E_b^i(k) = E^{HF}(N-1,k) - E^{HF}(N,k) = -\epsilon_k \ . \tag{69}$$

The chemical shift is thus approximated as

$$\Delta E_b^V(k) \approx -[(\epsilon_k)_1 - (\epsilon_k)_2] \ . \tag{70}$$

As the contribution from core-hole relaxation is – in many cases – considerably smaller than the contribution from the initial-state effect, the Koopman's theorem are good approximations for predicting chemical shifts for a variety of systems [59] .

3.1.2.2 Density functional theory method

Density functional theory offers an alternative way to calculate binding energies and chemical shifts that accurately accounts for the final-state effect. The method is based on Slater's transition state formalism for the evaluation of electronic excitation energies [107]. Within a Kohn-Sham DFT formalism, the total energy of a system is an analytic function of the occupation numbers of the KS orbitals:

$$E = E(n_1, n_2, \cdots, n_N) \ , \tag{71}$$

where n_i is the occupation number for the one-electron-like molecular orbital $\phi_i(\mathbf{r})$. Assuming a photoemission process where, for instance, a core electron from $i =$ 1st level is ejected,

the energies of the initial and final states are E(1,1,1,$\cdots$,1) and E(0,1,1,$\cdots$,1), respectively. The core-level binding energy is thus equal to

$$E_b^V = E(0,1,1,\cdots,1) - E(1,1,1,\cdots,1) \ . \tag{72}$$

By taking advantage of the analytical dependence of E on n_i, one can write:

$$E(0,1,1,\cdots,1) = E(\frac{1}{2},1,1,\cdots,1) - \frac{1}{2}\frac{\partial E}{\partial n_1} + \frac{1}{2!}(\frac{1}{2})^2\frac{\partial^2 E}{\partial^2 n_1} - \frac{1}{3!}(\frac{1}{2})^3\frac{\partial^3 E}{\partial^3 n_1} + \cdots \ , \tag{73}$$

where the partial derivatives are evaluated at $(\frac{1}{2},1,1,\cdots,1)$. The Taylor expansion of E(1,1,1,$\cdots$,1) around $(\frac{1}{2},1,1,\cdots,1)$ includes the same terms as that in Equation (73) but with all the signs positive. By taking the difference of these Taylor series, the even order terms cancel out, leaving

$$E_b^V = -\frac{\partial E}{\partial n_1} + (\delta n_1)^3 \ . \tag{74}$$

The Janak's theorem [56] proves that the derivative of the DFT total energy with respect to the occupation number of a KS orbital is equal to the orbital energy:

$$\partial E/\partial n_i = \epsilon_i \ , \tag{75}$$

where ϵ_i is the Kohn-Sham orbital energy (Equation (24)). Therefore, by keeping only the first term in Equation (74), the binding energy E_b^V can be obtained by computing ϵ_i at a fractional occupation 1/2. For core-level excitations, the error can be minimized by using [17, 125]

$$E_b^V = -\frac{1}{4}\frac{\partial E}{\partial n_i}\bigg|_{n_i=1} - \frac{3}{4}\frac{\partial E}{\partial n_i}\bigg|_{n_i=\frac{1}{3}} \ . \tag{76}$$

This method has been used to calculate core-level binding energies and chemical shifts of a large number of systems, achieving an impressive accuracy [18, 117].

3.1.3 A pseudopotential approach for calculating core-level shifts

In this thesis work, core-level shifts are calculated by using the core-excited pseudopotential technique [47, 88, 116]. This method does not require all-electron calculations, and it is suitable to study large systems such as graphene oxide. A core-level shift calculated through the use of this technique accounts for the vertical photoexcitation transition and includes the core-hole relaxation effects.

The main idea of this method is to use a pseudopotential that simulates the presence of a screened 1s hole in the core for the ionized C^+ (or O^+) species. The core-level binding energy at a C (or O) site in a molecular or material system is the difference in total energy between the ionized state $E[C^+]$ and the neutral state $E[C]$ (Equation (72)). The core-level shift ΔC_{1s} at the selected C site relative to the reference C is then calculated as

$$\Delta C_{1s} = (E[C^+] - E[C]) - (E[C^+]_{ref} - E[C]_{ref}) \ , \tag{77}$$

where $E[C^+]_{ref}$ and $E[C]_{ref}$ are the DFT total energies of the ionized and neutral systems at the reference C site, respectively.

In details, two separate calculations are performed in order to obtain the core-level binding energy at a selected C site:

1. $E[C]$ is computed by a regular structure optimization and total energy calculation of the system, where all the atoms are described by the normal pseudopotentials.

2. Under the optimized structure of the neutral state, $E[C^+]$ is calculated by replacing the pseudopotential of the selected C with the modified pseudopotential. Electrons are fully relaxed to screen the core hole, and the ionic positions are fixed assuming the vertical transition during the photoemission. A uniform negative charge is applied to the background to maintain the overall charge neutrality, which is required by the periodic boundary conditions.

The pseudopotentials are generated following the procedure described in section 2.5.2, using an electronic structure of $1s^2\ 2s^2\ 2p^2$ for a free C atom in the case of the normal pseudopotential, while for the modified pseudopotential, using an electronic structure of $1s^1\ 2s^2\ 2p^2$ for a free C^+ ion instead. Eventually, core-level shifts are obtained by comparing the binding energies values at interested C sites to that of the reference C.

To test the performance of this method, I calculated the C 1s and O 1s core-level shifts for a set of organic molecules that include C, O and H. Each molecule is put in a cubic supercell with a lattice size of 20 Å. The chemical shifts are obtained by referring the C (O) 1s binding energies of the molecules to that of the C (O) in the CO molecule. Overall, the computed C 1s and O 1s core-level shifts are in good agreement with the experimental values (Figure 9, and Table 3 and 4), with an absolute mean error less than 0.2 eV (3%) and 0.1 eV (2%), respectively, over a range of about 6 eV.

The core-level shifts reported in Table 3 and 4 can be interpreted by using the point charge model. For C 1s chemical shifts, the degree of oxidation of C in the molecules considered in Figure 9 follows: CO > carboxylic acid (-COOH) > aldehyde (-CHO) > alcohol (-COH) > alkene (-C=C-) > benzene. According to the point charge model, C with a lower oxidation degree feels more nuclear shielding upon photoemission, and thus exhibits a lower C 1s binding energy. Consistently, the table shows that the C 1s chemical shifts of the above molecules with respective to CO are in turn getting larger (toward lower binding energies). In the case of O 1s chemical shifts, the O species in the selected molecules have the same oxidation number (-2), and the electron relaxation about the core hole plays a dominant role in the chemical shifts. More relaxation occurs in the system of larger sizes, since the screening charges can be taken further away from the core [13], resulting in lower binding energies. As shown in the table, the O 1s chemical shift with respect to CO (toward lower binding energies) is larger in acetaldehyde (CH_3COH) than that in

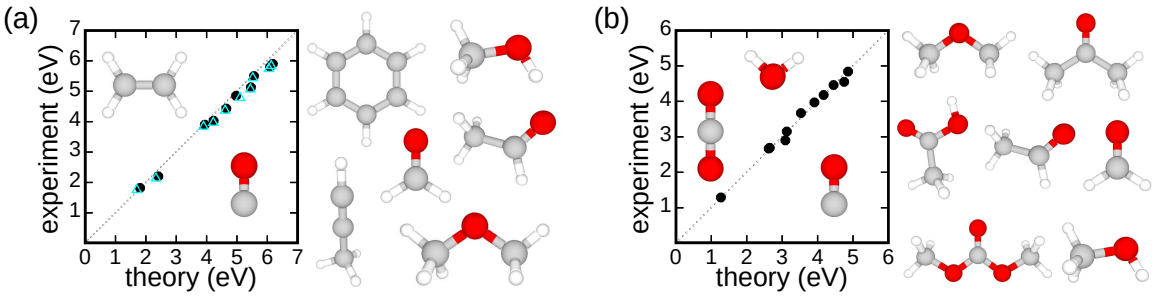

Figure 9: Experimental vs. computed (a) C 1*s* and (b) O 1*s* chemical shifts of C and O in selected molecules, shown by the ball-and-stick illustration. Grey, red and white colors (hereafter) represent C, O and H atoms, respectively. The energy shifts are referred to that of C and O in the CO molecule. Black discs and cyan triangles are computed values by accounting for the vertical photoexcitation transition and the adiabatic effect, respectively. To calculate the latter quantities, the geometry of the ionized system is fully relaxed, and E[C^+] is computed under the new structure. Chemical shifts obtained by using the two schemes are very close, with difference less than 0.1 eV on average. Given the good performance of the vertical transition scheme, the adiabatic effects will not be considered in the following work.

Table 3: C 1*s* core-level energy shifts (in eV) of C atoms in selected molecules. The chemical shifts are referred to that of C in CO. ΔC_{1s} and $\Delta^a C_{1s}$ are calculated values by accounting for the vertical transition and adiabatic effect, respectively.

	Chemical formula	ΔC_{1s}	$\Delta^a C_{1s}$	expt.[6]
formaldehyde	CH_2O	1.81	1.70	1.82
methanol	CH_3OH	3.94	3.90	3.90
ethylene	C_2H_4	5.56	5.52	5.50
acetaldehyde	CH_3C^*OH	2.41	2.33	2.20
	C^*H_3COH	4.97	5.10	4.85
dimethyl ether	$(CH_3)_2O$	4.23	4.22	4.03
methylacetylene	CH_3CC^*H	6.09	6.05	5.80
	CH_3C^*CH	5.46	5.44	5.13
	C^*H_3CCH	4.65	4.61	4.43
benzene	C_6H_6	6.18	6.13	5.90

Table 4: O 1s core-level energy shifts (in eV) of O atoms in selected molecules. The chemical shifts are referred to that of O in CO. ΔO is calculated values by accounting for the vertical transition.

	Chemical formula	ΔO	expt.[6]
carbon dioxide	CO_2	1.27	1.29
water	H_2O	2.65	2.69
formaldehyde	CH_2O	3.13	3.15
acetaldehyde	CH_3COH	4.17	4.18
acetic acid	CH_3CO^*OH	4.45	4.46
	CH_3COO^*H	2.62	2.67
methanol	CH_3OH	3.53	3.67
ethanol	CH_3CH_2OH	3.91	3.97
dimethyl ether	$(CH_3)_2O$	4.86	4.84
dimethyl carbonate	$(CH_3O)_2CO^*$	4.75	4.55
	$(CH_3O^*)_2CO$	3.09	2.90

formaldehyde (CH_2O), and also is larger in ethanol (CH_3CH_2OH) than that in methanol (CH_3OH).

In summary, the calculations on molecules suggest that the core-excited pseudopotential approach provides reliable results on the core-level shifts of C and O species in various chemical states. This method is used to compute the C 1s and O 1s XPS spectra of EGO models to interpret the experimental results shown in Figure 4(a), as will be discussed in the following section.

3.2 Calculations of XPS spectra for multilayer EGO films

As discussed in Chapter I (section 1.2.2), the experimental XPS spectra (Figure 4(a)) shows that the oxidized epitaxial graphene (EGO) films stored at room temperature undergo spontaneous reduction – the O:C ratio drops from 0.44 in as-synthesized EGO, to 0.38 in EGO aged for about one month, and remains little changed thereafter. The evolution of C 1s XPS spectra also shows the increase (decrease) of the unoxidized (oxidized) C species during a two-month period, indicating structural modifications with a longer life-time in the EGO films. However, it is impossible to determine from the experiment the fractions of epoxide, hydroxyl and water species in the as-synthesized EGO films; how they change with time; what values these fractions attain in the aged EGO. Moreover, the mechanism underlying the observed metastable characteristics of the EGO films is a big question mark. To solve these puzzles, I performed DFT calculations to compute the C 1s and O 1s XPS spectra for multilayer EGO models with various chemical compositions, based on the core-excited pseudopotential approach described previously. I extracted the fractions of epoxide, hydroxyl and water species of the EGO films from the comparison of XPS between theory

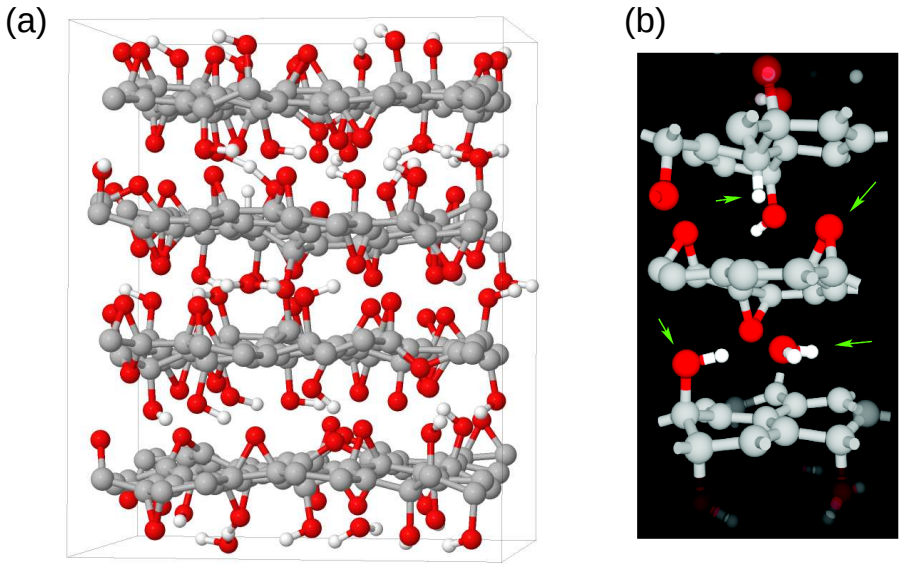

Figure 10: (a) Model structure of EGO generated from DFT-D. (b) A selected region of the same model showing the predominant chemical species present in EGO; clockwise from the top and indicated by the green arrows: a C-H species, an epoxide group, a water molecule, and a hydroxyl group.

and experiment. Based on these information, I further proposed a reduction mechanism to explain the metastability of this new material.

3.2.1 Model structures of multilayer EGO films

To model the EGO films, I ignored the surface and interface effects, and I used periodic atomistic structures of bulk GO to represent the interior of the EGO films. To generate the model structures, I used an orthorhombic supercell consisting of 4-layer graphite in "AB" stacking geometry and 5 $\times$ 6 graphene unit cells per layer. Epoxide, hydroxyl and water species are randomly distributed on or in-between the carbon layers (Figure 10). The fractions of each type of oxygen species are selected according to two criterions:

1. The ratio of the total number of O atoms to the total number C atoms in the EGO model equals to the experimental value of the O:C ratio.

2. The fraction of C-O bonds with respect to the total number of C atoms in the EGO model equals to the ratio of the area of C-O-C/C-OH peak to the total area of C 1s XPS spectra obtained from experiment (this ratio is hereafter denoted as P_{GO}).

Carbonyl groups are not considered in the models, since their concentration is small in the EGO films. The model structures are fully optimized by DFT-D using the variable-cell Car-Parrinello damped molecular dynamics simulation for both electronic and cell degrees of

Table 5: Chemical, geometrical, and energetic information of model structures of as-synthesized EGO generated from DFT-D. The models have an O:C ratio of 0.44. The fractions of C-O-C, C-OH, and H_2O species are referred to the total number of C atoms. Mean interlayer separation, average intralayer vertical buckling, and mean interlayer binding energy are indicated by d, Δd, and E_b, respectively.

Model	C-O-C	C-OH	H_2O	d(Å)	Δd(Å)	E_b(meV/Å^2)
A	0.26	0.18	0.00	4.43	0.30	44.2
B	0.26	0.16	0.02	4.48	0.30	45.1
C	0.30	0.13	0.02	4.45	0.35	32.5
D	0.31	0.06	0.07	4.63	0.38	33.4

Table 6: Chemical, geometrical, and energetic information of model structures of aged EGO generated from DFT-D. The models have an O:C ratio of 0.38. Labels are the same as that in Table 5.

Model	C-O-C	C-OH	H_2O	d(Å)	Δd(Å)	E_{bind}(meV/Å^2)
E	0.10	0.27	0.01	4.55	0.28	49.5
F	0.25	0.05	0.08	4.69	0.38	38.0
G	0.18	0.20	0.00	4.55	0.31	37.3

freedom. Unfavorable ionic configurations are eliminated through the relaxation. Graphitic layers are buckled and expanded due to the adsorbed oxygen functionalities.

By using this strategy, I generated a total of seven EGO models, with an O:C ratio equal to 0.44 in model A-D, representing the as-synthesized EGO films with aging time of 1 day, and an O:C ratio of 0.38 in model E-G, modeling the aged EGO films with aging time of 70 days. For each O:C ratio, the model structures include various fractions of -O-, -OH and H_2O species. The chemical composition, interlayer distance, mean vertical buckling of carbon planes, and interlayer binding energy of the EGO models are reported in Table 5 and 6. With the dispersion correction accounting for the long-range attractions between graphitic layers, the obtained interlayer distances for the EGO models range from 4.4 Å to 4.7 Å, depending on the water content. Binding energies are between 32 meV/Å^2 and 50 meV/Å^2, a little larger than the value for graphite (30 meV/Å^2), due to the presence of oxygen species. Mean vertical buckling is evaluated as the root-mean-square deviation of the z coordinate (out-of-plane direction) of C atoms on each layer. Larger buckling is found for the models containing larger fractions of epoxide groups.

3.2.2 Computed XPS spectra for as-synthesized EGO

The XPS spectra of the EGO models are calculated in the following procedure: First, the C 1s and O 1s core-level shifts are computed at each C and O site for the optimized EGO

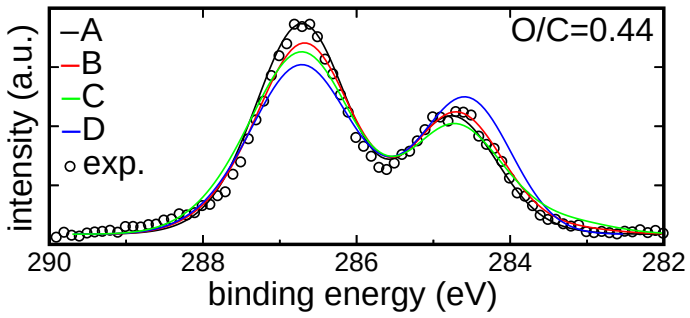

Figure 11: Experimental (circles) and computed (lines) C 1*s* XPS spectra of as-synthesized EGO. Shirley background is subtracted from the experimental data. The chemical compositions of the models are reported in Table 5.

structures, based on the core-excited pseudopotential approach described previously. Then, for each model, the individual energy shift is broadened by a Gaussian function with a width of 0.5 eV [135]. Finally, the obtained XPS spectra is rigidly translated along the energy axis to achieve best match with the experimental spectra for comparison.

Figure 11 shows the computed C 1*s* XPS spectra (lines) for the as-synthesized EGO models in comparison with the experimental data (circles). Model A including no water best reproduces the experimental spectra. The fractions of -O- and -OH in this model equal to 0.26 and 0.18, respectively, yielding the fraction of oxidized C – P_{GO} – of 0.66, very close to the experimental value of 0.64. As the water content increases, model B, C and D keep P_{GO} values of 0.64, 0.65 and 0.61, respectively, by increasing the amount of -O- and decreasing the amount of -OH species. However, their spectra lose intensity in the C-O-C/C-OH peak, and the accord with the experiment worsens steadily as increasing the concentration of water.

To understand the origin of the disagreement, the computed C 1*s* spectra are further decomposed according to the oxidation states presenting in the model structures (Figure 12). The red, blue, green and magenta lines represent the XPS components arising from unoxidized C, C-O-C and C-OH, C bonding to an ether group (C-O'-C), and doubly oxidized C which simultaneously bond to an epoxide (or hydroxyl) and an ether group, respectively (Figure 13). The C 1*s* binding energies are found to be about -0.9 eV for C-O'-C, and 0.9 eV for doubly oxidized C, both referred to that of C-O-C/C-OH. This means a large number of ether and doubly oxidized C species will broaden and shorten the overall peak contributed by oxidized C atoms. Consistently, model A-D contain C-O'-C species of 4%, 5%, 6% and 7%, and 3%, 5%, 7% and 7% for doubly oxidized C, respectively. The occurrence of these two chemical species is due to the high concentration of epoxide groups, which induce large stress and form agglomerations on the carbon basal planes. At a fixed O:C ratio, to allow more water and meanwhile keep P_{GO} as about 0.64 in the EGO models, it is necessary to increase the fraction of -O- and decrease the fraction of -OH, which in turn inevitably leads

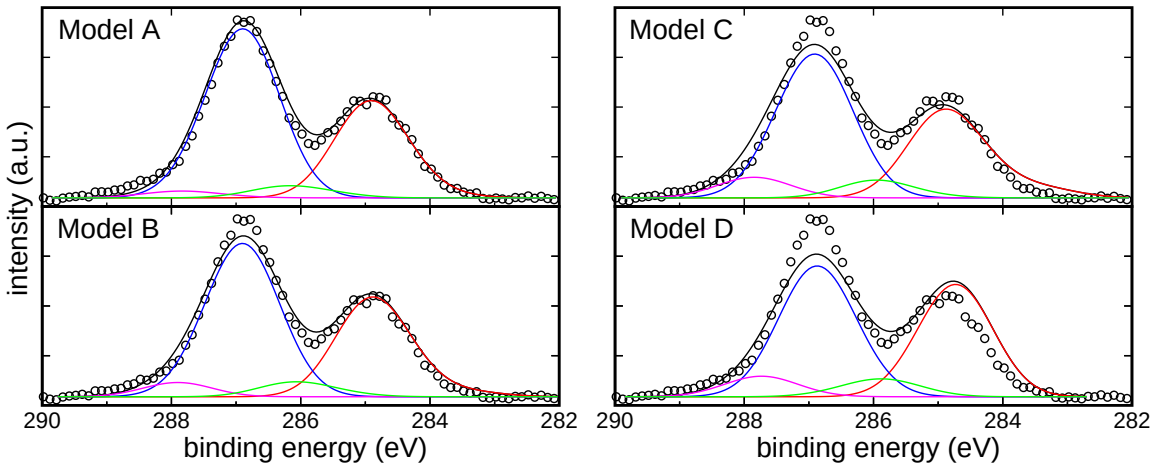

Figure 12: Calculated C 1*s* XPS spectra (black line) of model A-D, compared with the experimental spectra of as-synthesized EGO (circles). The computed spectra are decomposed in four peaks: unoxidized C (red line), C-O-C and C-OH (blue line), C bonding to ether groups (green line), and doubly oxidized C species (magenta line).

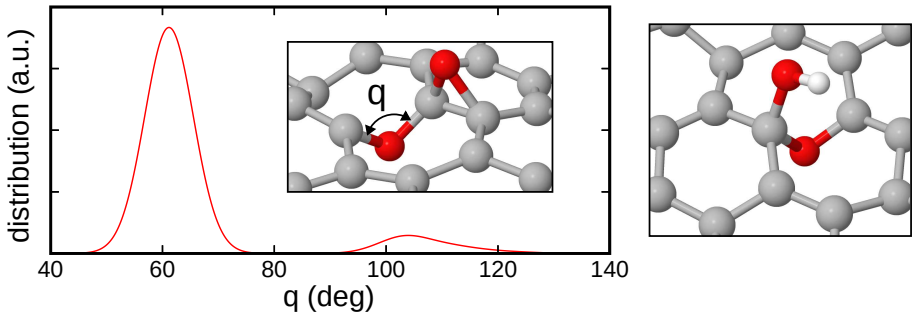

Figure 13: Distribution of C-O-C bond angle extracted from the EGO models. Epoxide and ether groups are clearly distinguishable by this geometrical parameter. The atomistic structures of doubly oxidized C species are shown as inset and on the right.

to the formation of C-O'-C and doubly oxidized C species, and hence to a deterioration of the agreement between theory and experiment.

Based on the calculations on model A-D, the as-synthesized EGO films contains water no larger than 2%, and fractions of epoxide and hydroxyl groups are estimated to be about 26% and 18%, respectively. The success of this estimation relies on the fact that the C 1*s* XPS spectra shows a fairly large P_{GO} value for the as-synthesized EGO films with an O:C ratio of 0.44. Increasing or decreasing the concentration of epoxide groups from 26% results in less intensity in the C-O-C/C-OH peak, and deteriorates the agreement with the experiment.

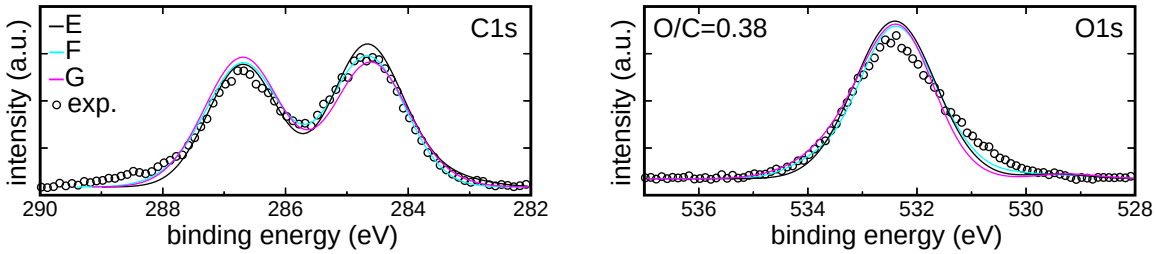

Figure 14: Experimental (circles) and computed (lines) C 1*s* (left) and O 1*s* (right) XPS spectra of aged EGO. Shirley background is subtracted from the experimental data. The chemical compositions of the models are reported in Table 6.

3.2.3 Computed XPS spectra for aged EGO

Similar analysis is carried out to elucidate the chemical composition of the aged EGO (Figure 14). In this case, however, the aged EGO films have an O:C ratio of 0.38, and P_{GO} of about 0.45. The comparison between computed and experimental XPS spectra shows that the aged EGO may incorporate fractions of water molecules up to about 8%. In particular, under the assumption of little water, model E is rich in -OH (27%) and deprived of -O- (10%) species, yielding P_{GO} of 0.44, very close to the experimental value; while model G contains 20% -O- and 18% -OH groups, with P_{GO} of 0.52, in less agreement with the experiment. On the contrary, to accommodate H_2O and meanwhile keep P_{GO} of about 0.45, the EGO models have to include more -O- and less -OH species. Model F gives an upper limit of the water content – about 8% – for the aged EGO films, with 25% -O- and 5% -OH groups, and P_{GO} of 0.51.

The O 1*s* XPS spectra can neither help to determine the water content for the aged EGO. The O species in water molecules intercalated in-between the carbon planes exhibits the same O 1*s* binding energy as that in -O- and -OH groups, and thus they are indistinguishable from the O 1*s* XPS spectra. The major difference between the computed and experimental O 1*s* spectra around 531 eV arise from carbonyl groups, whose chemical shifts relative to that of -O-/-OH is about -1.8 eV [3], and these oxygen functionalities are not considered in the EGO models. Ether groups show an O 1*s* energy shift of about 1.6 eV referred to that of -O-/-OH groups. The fractions of ether groups in model E-G are 1%, 4% and 3%, respectively, with the value for model E most close to the experimental value (1%). However, the differences in the O 1*s* XPS spectra arising from ether species are very small between the EGO models.

According to these results, the aged EGO films may contain 0-8% water, with fractions of -OH and -O- species varying from 0.27 and 0.1, to 0.05 and 0.25, respectively. In addition, Table 5 and 6 indicate that the total fraction of hydrogen P_H – present in the form of either hydroxyl or water species – is larger in the aged EGO than that in the as-synthesized EGO

films. A simple analysis corroborates this result:

$$\begin{aligned} P_O + P_{OH} + P_{H_2O} &\approx P_{oxygen} \\ 2P_O + P_{OH} &\approx P_{GO} \ , \end{aligned} \tag{78}$$

where P_O, P_{OH} and P_{H_2O} are the fractions of epoxide, hydroxyl and water species, respectively, relative to the total number of C atoms. P_{oxygen} is the O:C ratio. P_{GO} is the fraction of oxidized C. Only the C atoms that directly make a bond with oxygen functionalities are considered to contribute to P_{GO}, and the contributions from carbonyl groups are neglected. The term associated with P_O can be eliminated by rearrangement of the two equations, yielding

$$P_{OH} + 2P_{H_2O} = 2P_{oxygen} - P_{GO} = P_H \ . \tag{79}$$

Using the experimental values of P_{oxygen} and P_{GO}, P_H is estimated to be about 0.23 for the as-synthesized EGO and 0.31 for the aged EGO. The increase of H content in hydroxyl and water species leads to a hypothesis that there is an excess of hydrogen in the as-synthesized EGO films, most probably present in the form of C-H species. Calculations show C-H species in the EGO models exhibit C $1s$ binding energies very close to that of sp^2 C atoms. These hydrogen species may react with epoxide and hydroxyl groups, leading to the observed spontaneous reduction, and structural modifications in the EGO films.

3.2.4 Proposed reduction mechanism

To corroborate the hypothesis that C-H species is the key to explain the metastable characteristics of the EGO films, I performed DFT calculations to compute the energies involved in the diffusion process of isolated C-H, hydroxyl and epoxide species on a single-layer graphene, as well as in the binary reactions between a C-H species and either an epoxide or a hydroxyl group on graphene (Figure 15). Energy barriers are computed by using the nudged elastic band (NEB) method (see section 4.1.1.2) based on DFT scheme. The calculations show that the diffusion barriers for a single C-H, -OH, and -O- group on graphene are 1.0 eV, 0.5, and 0.8 eV, respectively. The energy barrier for C-H species is obtained by excluding the vibrational zero-point energy of 0.3 eV. The H proton in a -OH group is known to be able to transfer to a adjacent -O- group with an energy barrier of only 0.3 eV [134]. Hence both -O- and -OH species migrate rapidly on graphene, providing the chance for the encounter and making reactions with other chemical species. The two binary reactions: {-O-} + {-H} $\rightarrow$ {-OH} and {-OH} + {-H} $\rightarrow$ {H_2O} are found to be energetically favored by 2.4 eV and 3.9 eV, respectively, both involving an activation energy of about 0.5 eV.

These result support our hypothesis and analyses. According to these results, the availability of C-H species in the as-synthesized EGO films triggers the reactions of -O- and -OH groups at room temperature, leading in time to an increase of H_2O molecules, and

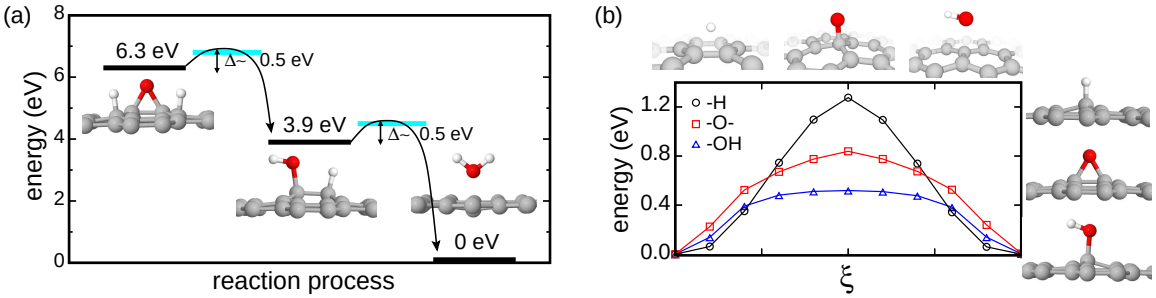

Figure 15: (a) DFT energy diagram of the reduction process in EGO. The line segments show the energy levels of the reactants and products (black), and the transition states (cyan) of the two reactions, all referred to that of a H_2O molecule physisorbed on graphene. The corresponding optimized atomic configurations are shown next to their energy levels. (b) The diffusion processes of individual -H, -O- and -OH species on graphene given by NEB-DFT calculations. The optimized structures of the three species in equilibrium and transition state are shown on the right and top of the energy profile, respectively.

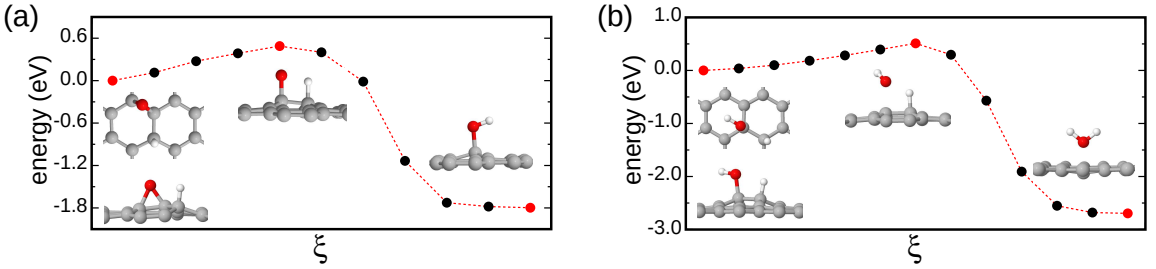

Figure 16: Energy profiles of the reaction processes of (a) -H and -O- to the formation of -OH, (b) -H and -OH to the formation of a physisorbed water on graphene, obtained by NEB-DFT calculations. The atomic configurations of the initial state (top and side views), transition state and final state are shown as inset next to their corresponding energy points marked by red discs. The energy values are referred to that of the initial state.

meanwhile a decrease of -O- species. The formation and release of water would explain the spontaneous reduction of the EGO films, while the decreasing number of epoxide in EGO would explain the structural modifications and the fact that these changes exhibit a longer life-time than the reduction process.

3.3 Summary of main results

The comparisons between computed and experimental XPS spectra show that the as-synthesized EGO films contain little amount of water (less than 2%), with fractions of epoxide and hydroxyl groups equal to 0.26 and 0.18, respectively. The aged EGO films may incorporate water molecules up to 8%, with fractions of epoxide and hydroxyl species varying from 0.10 and 0.27, to 0.25 and 0.05, respectively. The total amount of hydrogen – in the form of either hydroxyl or water species – increase from 0.23 in the as-synthesized EGO to 0.31 in the aged EGO. The increase of the hydrogen content may be due to the excess of C-H species in the EGO films, which favors the reactions with epoxide and hydroxyl groups, leading to the formation of hydroxyl and water species, respectively. Formation and desorption of water molecules would explain the spontaneous reduction of the EGO films, while the consumption of epoxide species would result in structural modifications with a longer life-time. The presence of C-H species in graphene oxide has been confirmed by the infrared spectroscopy measurements [62]. The proposed reduction mechanism can be further corroborated experimentally by replacing hydrogen with deuterium in the sulfuric acid solution for the synthesis of EGO. The additional mass of hydrogen would lead to slower diffusion processes (smaller vibrational frequencies) for both C-H species and hydroxyl groups, and therefore it would slow down the chemical and structural changes of EGO observable by XPS. This additional experiment would corroborate our findings and it would give further insight on the nature of the mechanisms leading to the changes in graphene oxide. Overall, these studies provide a better understanding of the room-temperature metastability of EGO, and suggest a route for controlling the reduction level by gauging the hydrogen content in EGO.

CHAPTER IV

ORIGIN OF CHEMICAL AND KINETIC STABILITY OF EGO

In the previous work, I elucidated the metastable characteristics, and chemical compositions of the EGO films. It is still not well understood what are the driving forces for the chemical and structural modifications in EGO at room temperature, and what is the spatial distribution of oxygen functionalities in aged EGO that attains quasi-equilibrium. In this chapter, I will address these questions by systematic studies of the chemical and kinetic stability of EGO at T=300 K and p=1 bar. In particular, I employed the transition state theory to interpret the kinetics of chemical reactions occurring in EGO, and I used the nudged elastic band method to compute the minimum energy path, transition states, and energy barriers for possible reaction processes. Moreover, I developed a lattice-model Monte Carlo scheme to mimic the aging process in EGO at mild temperatures (T$\leq$ 70 °C), and determined the quasi-equilibrium intralayer structure of the oxidized layers. These methods will be introduced in the first section of this chapter.

4.1 Methods

4.1.1 Calculation of chemical reaction rates

4.1.1.1 Transition state theory

The kinetics of the chemical and structural evolution in EGO depends on the rates of diffusion processes of oxygen species, and the rates of chemical reactions occurring in the material. Most of these processes involve energy barriers of a few tenth eV or even larger, and they take place, at room temperature, at a much slower rate than atomic vibrations. It is inefficient to study these "rare events" by direct molecular dynamics simulations.

Transition state theory (TST) provides a simple route to estimate reaction rates of rare events. It was developed in 1935 by Eyring and by Evans and Polanyi [32, 31]. TST focuses on the activated complexes at the saddle point of the potential energy surface in a statistical way without considering the details of atomic vibrations. For simplicity, Figure 17(a) shows a 2D potential energy surface of a system. Each energy point corresponds to a possible configuration of the system. Regions of darkest gray are the local minima and correspond to stable configurations or equilibrium states, where the system spends most of its time. Regions of light gray have high energies and the system rarely visits. During the vibration around the local minima, the system occasionally hops from one local minima to another by crossing the saddle point. There are infinite number of trajectories for such a hopping. The path with the highest transition probability is the one along which the change

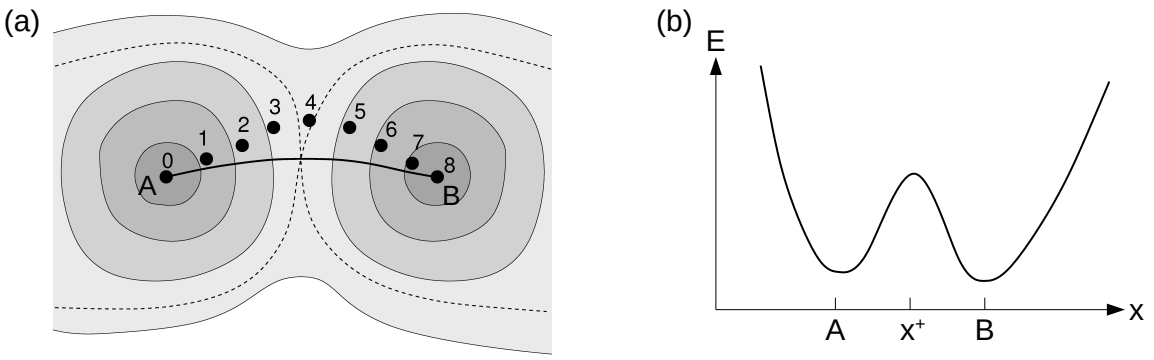

Figure 17: (a) A two-dimensional potential energy landscape. Regions A and B shown in dark gray are two local minima, connected by the minimum energy path (MEP) indicated by the dark line. The dashed curves represent the energy surface equal to the transition state energy. The black discs labeled by numbers represent the images used in a NEB calculation. (b) One-dimensional energy profile of a MEP.

in energy during the motion is minimized, and is called the minimum energy path (MEP) for the process.

Figure 17(b) shows a schematic one-dimensional (1D) energy profile of a MEP from basin A to B. The saddle point at $x^\dagger$ is called the transition state (TS). All the points on the left (right) of the transition state are referred to as state A (B). TST gives the rate of hopping from state A to state B as

$$k_{A\to B} = (probability\ of\ being\ in\ TS) \times (flux\ out\ of\ TS)\ . \tag{80}$$

The flux of atoms out of the transition state can be estimated as [105]

$$\frac{1}{2} \times (average\ thermal\ velocity\ of\ hopping\ atom)\ per\ unit\ length\ , \tag{81}$$

where the factor of one-half comes from the fact that only half of the atoms are moving from state A to B. According to the Maxwell-Boltzmann distribution, the average velocity of atoms in a system in the thermodynamic equilibrium at temperature T is $\sqrt{\frac{2k_BT}{\pi m}}$, where k_B is the Boltzmann constant, and m is the mass of the atom. The probability for finding an atom in the transition state is defined relative to all possible positions of the atom in state A. The probability for observing an atom at any particular position x is

$$p(x) \propto exp[-\frac{E(x)}{k_BT}]\ . \tag{82}$$

The probability of finding an atom at $x = x^\dagger$ is thus given by

$$p(x^\dagger) = \frac{e^{-\beta E(x^\dagger)}}{\int_A e^{-\beta E(x)}}\ , \tag{83}$$

where $\beta = 1/k_B T$, and the integral is taken over all the positions within state A. Putting all of these together, one obtains

$$k_{A\to B} = \frac{1}{2}\sqrt{\frac{2}{\beta\pi m}}\frac{e^{-\beta E(x^\dagger)}}{\int_A e^{-\beta E(x)}} \,. \tag{84}$$

For tightly bound solid systems, the harmonic approximation to TST can be applied. Consider the 1D problem illustrated in Figure 17(b), the energy is expanded around the minimum A as

$$E(x) \simeq E_A + \frac{K}{2}(x - x_A)^2 \,, \tag{85}$$

where the parameter K is related to the vibrational frequency ν of the atom around the minimum via $\nu = \frac{1}{2\pi}\sqrt{\frac{K}{m}}$. This gives an explicit form of $k_{A\to B}$ as

$$k_{A\to B} = \nu \cdot exp(-\frac{E^\dagger - E_A}{k_B T}) \,, \tag{86}$$

which is the so-called "harmonic transition state theory" (HTST). $E^\dagger$ and E_A represent the transition state energy $E(x^\dagger)$ and the potential minimum $E(x_A)$, respectively. $\Delta E = E^\dagger - E_A$ is known as the activation energy or energy barrier of the reaction process. For multiple dimensions, Equation (85) has to be adjusted by using multivariable Taylor series, and it is not difficult to show that [105]

$$k_{A\to B} = \frac{\prod_{i=1}^{N}\nu_i}{\prod_{i=1}^{N-1}\nu_i{}^\dagger} \;\; exp(-\frac{\Delta E}{k_B T}) \,, \tag{87}$$

where ν_i and $\nu_i{}^\dagger$ are the normal mode frequencies associated with the energy minimum and the saddle point, respectively.

Equation (87) allows a qualitative estimation of the reaction rate once ν and ΔE are known [67, 118]. The critical part is to locate the transition state. One of the most widely used methods to find the minimum energy path and transition states is the nudged elastic band method, which is applied in this thesis work and will be briefly introduced as follows.

4.1.1.2 The nudged elastic band method

The nudged elastic band (NEB) method finds the entire minimum energy path between an initial state and a known final state by creating a string of images connecting the two minima, and these images are evenly spaced along the MEP [78, 79]. For instance, the smooth line connecting minima A and B in Figure 17(a) represents the MEP. Points 1-7 are the images to be optimized to mimic the MEP. The forces on these images are given by $\mathbf{F} = -\nabla E$. The MEP are obtained only if the forces on each images are oriented along the path. This could be achieved by constructing an objective function [58]

$$S(\mathbf{R}_1, ..., \mathbf{R}_N) = \sum_{i=1}^{N-1} E(\mathbf{R}_i) + \sum_{i=1}^{N}\frac{K}{2}(\mathbf{R}_i - \mathbf{R}_{i-1})^2 \,, \tag{88}$$

and minimizing it with respect to the intermediate images $\mathbf{R}_1$,...,$\mathbf{R}_{N-1}$. $E(\mathbf{R}_i)$ is the total energy of the ith image, and K is the stiffness of the springs connecting the images. The end points $\mathbf{R}_0$ and $\mathbf{R}_N$, corresponding to the initial and final states, remain fixed through the minimization. Equation (88) is the so-called the "plain elastic band method". The total force acting on the ith image is

$$\mathbf{F}_i = -\nabla E(\mathbf{R}_i) + \mathbf{F}_i{}^s \ , \tag{89}$$

where the first term is referred to as the true force, and the second term is the force by the springs, and equals to

$$\mathbf{F}_i{}^s = K(\mathbf{R}_{i+1} - \mathbf{R}_i) - K(\mathbf{R}_i - \mathbf{R}_{i-1}) \ . \tag{90}$$

The choice of the spring constant K is essential for correctly locating the saddle point. When using a too soft elastic band, the true force along the path leads to the images sliding down from the barrier region toward the two end points, and hence reduces the resolution of the path in the region of greatest importance. Another problem is known as "corner cutting". In the regions where the MEP is curved, the spring force perpendicular to the path pulls the images off the MEP, yielding a shorter path than the real MEP and overestimating the activation energy.

These problems can be cured by using the "nudging" strategy, i.e. projecting out the parallel component of the true force and the perpendicular component of the spring force, such that the total force on the ith image becomes

$$\mathbf{F}_{i,update} = -\nabla E(\mathbf{R}_i)|_\perp + (\mathbf{F}_i{}^s)_{||} \ . \tag{91}$$

Using a unit vector $\hat{\tau}_i$ representing the direction along the path for image i, the perpendicular component of the true force is given by

$$-\nabla E(\mathbf{R}_i)|_\perp = -\nabla E(\mathbf{R}_i) + \nabla E(\mathbf{R}_i) \cdot \hat{\tau}_i \hat{\tau}_i \ , \tag{92}$$

and the parallel component of the spring force is

$$(\mathbf{F}_i{}^s)_{||} = \mathbf{F}_i{}^s \cdot \hat{\tau}_i \hat{\tau}_i \ . \tag{93}$$

In this way, the term $-\nabla E(\mathbf{R}_i)|_\perp$ adjusts the images to approach the MEP, and the term $(\mathbf{F}_i{}^s)_{||}$ keeps the images evenly spread out along the path. Once the update force is minimized to zero for every image, all the images lie on the MEP.

The NEB method gives a discrete representation of the MEP, and the energy of the saddle point has to be estimated by interpolation. This may become problematic when the energy profile around the saddle point is narrow with respect to the MEP length, such that few images are around the saddle point. The climbing image NEB (CI-NEB) method makes

improvement over the NEB method – it gives a precise estimation of the saddle point at no extra computational cost [52]. After a few iterations using the regular NEB, the image with the highest energy i_{max} is identified. Then the update force on this image is not given by Equation (91), but by

$$\mathbf{F}_{i_{max},update} = -\nabla E(R_{i_{max}}) + 2\nabla E(\mathbf{R}_{i_{max}})|_{||} = -\nabla E(\mathbf{R}_{i_{max}}) + 2\nabla E(\mathbf{R}_{i_{max}}) \cdot \hat{\tau}_{i_{max}} \hat{\tau}_{i_{max}} \ , \tag{94}$$

which is the true force with perpendicular component plus the inverted parallel component along the path. The image i_{max} is not affected by the spring force. Therefore this climbing image is adjusted toward the highest energy and eventually converges to the real saddle point. Since the climbing image and all the other images are relaxed simultaneously, there is no additional cost of the computational efforts.

The NEB and CI-NEB methods have been applied to a variety of systems [51, 103, 119], and achieved great success in predicting the MEP and transition states, and thus help better understanding the long time dynamics of materials. In this thesis, I employed the CI-NEB method incorporated in the PWscf code in QUANTUM-Expresso package to investigate possible chemical reactions in graphene oxide systems.

4.1.2 The Metropolis Monte Carlo algorithm

Monte Carlo (MC) methods include a class of algorithms relying on repeated random number sampling to compute results. It was first developed for estimating integrals that can not be evaluated analytically. Consider a 1D integral:

$$F = \int_a^b dx f(x) \ , \tag{95}$$

which can also be written as

$$F = \int_a^b dx \left(\frac{f(x)}{\rho(x)} \right) \rho(x) dx \ . \tag{96}$$

$\rho(x)$ is an arbitrary probability density function. The integral can be estimated by performing a number of trials, each consisting of choosing a random number x_i from the distribution $\rho(x)$ in the range of (x_a, x_b), and making the average:

$$F = \langle \frac{f(x)}{\rho(x)} \rangle_{trials} = \frac{1}{N} \sum_{i=1}^{N} \frac{f(x_i)}{\rho(x_i)} \ . \tag{97}$$

The equation returns to the exact value of the integral when the total number of trials N is infinite large. A simple choice of $\rho(x)$ is a uniform distribution:

$$\rho(x) = \frac{1}{x_b - x_a}, \quad x_a \leq x \leq x_b \ , \tag{98}$$

and the integral is approximated as

$$F \approx \frac{x_b - x_a}{N} \sum_{i=1}^{N} f(x_i) \ . \tag{99}$$

For functions $f(x)$ having significant weights in only a few regions, a uniform sampling becomes inefficient (a large amount of computational efforts are wasted sampling the region where $f(x)$ is extremely small). Consider, for instance, the expectation value of a quantity A for a canonical ensemble:

$$\langle A \rangle_{NVT} = \int d\xi \ A(\xi) \ \rho(\xi) \ , \tag{100}$$

with

$$\rho(\xi) = \frac{exp\{-\beta E(\xi)\}}{\int d\xi \ exp\{-\beta E(\xi)\}} = \frac{exp\{-\beta E(\xi)\}}{Z} \ . \tag{101}$$

$E(\xi)$ is the total energy of the system at a given configuration ξ (ξ could be spatial coordinates, spins, and etc.). Z is the canonical partition function. For most functions $A(\xi)$, the integrand will be significant where $\rho(\xi)$ is significant. Sampling configurations at a distribution of $\rho(\xi)$ may be a good choice for efficient estimation of the integral via

$$\langle A \rangle_{NVT} = \langle A \rangle_{trials} = \frac{1}{N} \sum_{i=1}^{N} A(\xi_i) \ . \tag{102}$$

The Metropolis algorithm provides a route to generate a set of configurations of the system that satisfy a given distribution $\rho(\xi)$. The procedure is as follows:

1. Pick an initial configuration ξ_n.

2. Pick a trial configuration ξ_t, and compute the probability of accepting the trial configuration P_{ξ_n,ξ_t} via

$$P_{\xi_n,\xi_t} = \begin{cases} 1, & \rho(\xi_t) \geq \rho(\xi_n) \\ \rho(\xi_t)/\rho(\xi_n), & \rho(\xi_t) < \rho(\xi_n) \ . \end{cases} \tag{103}$$

   Call a random number p with a value between 0 and 1. Make $\xi_{n+1} = \xi_t$ if p $\leq P_{\xi_n,\xi_t}$. Otherwise, make $\xi_{n+1} = \xi_n$.

3. Go to step 2 replacing ξ_n by ξ_{n+1}.

After repeating step 3 for sufficient times, the generated ensemble tends to the distribution $\rho(\xi)$. This can be proved by considering an ensemble of N configurations, with N(ξ) members at the configuration ξ. Now apply the algorithm to this ensemble to generate more configurations. The net changes in the number of configuration ξ due to any other configuration ξ' equals to

$$\Delta N(\xi) = N(\xi') P_{\xi',\xi} - N(\xi) P_{\xi,\xi'} \ . \tag{104}$$

$P_{\xi',\xi}$ is the probability of accepting a trial configuration, and according to its definition by Equation (103), there is

$$\Delta N(\xi) = \begin{cases} N(\xi')\rho(\xi)/\rho(\xi') - N(\xi), & \rho(\xi') \geq \rho(\xi) \\ N(\xi') - N(\xi)\rho(\xi')/\rho(\xi), & \rho(\xi') < \rho(\xi) \ . \end{cases} \tag{105}$$

It gives $\Delta N(\xi)$=0 when $N(\xi)/N(\xi') = \rho(\xi)/\rho(\xi')$, i.e. the algorithm does not change the relative population of each configuration when the ensemble distribution attains the equilibrium distribution. It gives $\Delta N(\xi) > 0$ when $N(\xi)/N(\xi') < \rho(\xi)/\rho(\xi')$, i.e. the algorithm evolves the distribution towards equilibrium by increasing the number of configuration ξ (decreasing the number of configuration ξ when $N(\xi)/N(\xi') > \rho(\xi)/\rho(\xi')$).

In this thesis work, I used the Metropolis Monte Carlo algorithm to mimic the aging process in the EGO films at mild temperatures (T$\leq$ 70 °C), and to determine the quasi-equilibrium intralayer structure of EGO. The details of the methodology will be discussed in section 4.2.3.

4.2 Stability of graphene oxide: kinetics and thermodynamics

4.2.1 Isolated oxygen species on graphene

To investigate the stability of graphene oxide this complex system, I first considered a single-layer graphene with dilute oxidation. I used a large graphene layer chemisorbed by a single epoxide or a hydroxyl group to model this situation. The binding energy of the chemisorbed epoxide or hydroxyl group is defined as:

$${E_b}^{DFT} = E(g+O) - E(g) - \frac{1}{2}E(O_2) \tag{106}$$

and

$${E_b}^{DFT} = E(g+OH) - E(g) - \frac{1}{2}[\frac{1}{2}E(O_2) + E(H_2O)] \ , \tag{107}$$

respectively. In these equations, $E(g+O)$ and $E(g+OH)$ refer to the DFT energies of an epoxide and a hydroxyl group on graphene, respectively, $E(g)$ is the energy of pristine graphene, and $E(O_2)$ and $E(H_2O)$ are the DFT energies of the O_2 and H_2O molecules in vacuum, respectively. The binding energies are found to be 0.9 eV and 1.2 eV for epoxide and hydroxyl species, respectively, indicating that the chemisorption of the two functional groups on graphene is energetically unfavored. However, DFT total energies are evaluated at zero-temperature and zero-pressure. A more realistic situation is to consider a GO layer in the environment of gaseous O_2 and H_2O at T=300 K and p=1 bar. The thermodynamic stability of GO can be analyzed using the Gibbs free energy of formation $\Delta G(T,p)$, which is defined, for an arbitrary distribution of N_e amount of epoxide and N_h amount of hydroxyl groups on graphene, as

$$\Delta G(T,p) = G(GO) - G(g) - \frac{1}{2}N_e\mu_{O_2} - \frac{1}{2}N_h(\frac{1}{2}\mu_{O_2} + \mu_{H_2O}) \ , \tag{108}$$

where $G(GO)$ and $G(g)$ are the Gibbs free energies of GO and graphene, respectively. μ_{O_2} and μ_{H_2O} are the chemical potentials of gaseous O_2 and H_2O, respectively.

To calculate the Gibbs free energies, I used [93]

$$G(T,p) = F(T,V) + pV(T,p) \ . \tag{109}$$

The contribution of the pV term to $\Delta G(T,p)$ is negligible since the change of volume ΔV for solids is very small. The Helmholtz free energy $F(T,V)$ for GO with a specific configuration of epoxide and hydroxyl groups can be written as

$$F(T,V) = E^{DFT} + F^{vib.}(T,V) \ , \tag{110}$$

where E^{DFT} is the DFT total energy, corresponding to the Helmholtz free energy at zero temperature and neglecting zero-point vibrations. $F^{vib.}(T,V)$ comprises all contributions due to the vibrations and it is equal to

$$F^{vib.}(T,V) = E^{vib.}(T,V) - TS^{vib.}(T,V) \ , \tag{111}$$

where $E^{vib.}(T,V)$ and $S^{vib.}(T,V)$ are the vibrational energy and entropy, respectively, and both can be calculated from the partition function of an N-atomic system via

$$E^{vib.}(T,V,N) = -\frac{\partial}{\partial\beta} lnZ \tag{112}$$

and

$$S^{vib.}(T,V,N) = k_B(lnZ + \beta E^{vib.}) \ . \tag{113}$$

In the harmonic approximation, the partition function is given by [1]

$$Z = \sum_{i=1}^{3N} \int \frac{d\mathbf{k}}{(2\pi)^3} \sum_{n=0}^{\infty} e^{-(n+\frac{1}{2})\beta\hbar\omega_i(\mathbf{k})} \ , \tag{114}$$

where $\omega_i(\mathbf{k})$ are the $3N$ vibrational modes of the system. It is not difficult to show that

$$F^{vib.}(T,\omega) = \hbar\omega(\frac{1}{2} + \frac{1}{e^{\beta\hbar\omega}-1}) - k_BT[\frac{\beta\hbar\omega}{e^{\beta\hbar\omega}-1} - ln(1-e^{-\beta\hbar\omega})] \ , \tag{115}$$

according to which $F^{vib.}(T,V)$ can be obtained by an integral over the vibrational frequencies.

The phonon vibrational modes were calculated for pristine graphene and an epoxide group chemisorbed on graphene using the PH code in QUANTUM-Expresso package, which gives the value of $\Delta F^{vib} = F^{vib.}(g+O) - F^{vib.}(g)$ as -0.1 eV at T=300 K, indicating the vibrational contribution to ΔG is much smaller than the contribution from DFT total energies. I tested this assumption by a few GO systems including more oxygen functionalities in random distributions, and obtained ΔF^{vib} ranging from 0 to -0.1 eV per oxygen. Considering the phonon calculations are computationally costly, I used ΔF^{vib} = -0.1 eV per oxygen species for GO systems with any arbitrary chemical compositions.

To calculate the chemical potentials of gaseous molecules, I assumed O_2 and H_2O as ideal gas, and I used [5]

$$\mu(T,p) = \mu(T,p^0) + k_B T ln(\frac{p}{p^0}) \ , \tag{116}$$

which indicates the chemical potential at any pressure can be obtained if $\mu(T,p)$ at a given pressure p^0 is known. $\mu(T,p^0)$ by definition is equal to

$$\mu(T,p^0) = \mu(0K,p^0) + \Delta\mu(\Delta T,p^0) \ , \tag{117}$$

where $\mu(0K,p^0)$ is the enthalpy at T=0 K, and for ideal gas it can be referred to as DFT total energy E^{DFT}. $\Delta\mu(\Delta T,p^0)$ is the Gibbs free energy change from 0 K to T, and is given by

$$\Delta\mu(\Delta T,p^0) = [H(T,p^0) - H(0K,p^0)] - T[S(T,p^0) - S(0K,p^0))] \ . \tag{118}$$

The enthalpy and entropy at standard pressure (p^0 = 1 atm) and at any temperature are available in thermochemical tables [113], according to which $\Delta\mu(\Delta T,p^0)$ for O_2 is -0.54 eV, and for H_2O is -0.48 eV at T=300 K and p^0 = 1 atm. Considering a normal atmosphere consisting of about 21% O_2 and 1% H_2O, the pressure term in Equation (116) yields additional corrections of -0.04 eV for O_2 and -0.12 eV for H_2O.

According to the above analysis, the Gibbs free energy of formation for GO with arbitrary functionalizations is eventually given by

$$\begin{aligned} \Delta G =& [E(GO) - E(g) - \frac{1}{2}N_e E(O_2) - \frac{1}{2}N_h(\frac{1}{2}E(O_2) + E(H_2O))]_{DFT} \\ &+ [F^{vib.}(GO) - F^{vib.}(g)] + [0.3N_e + 0.5N_h] \ , \end{aligned} \tag{119}$$

where the first square bracket includes terms from DFT total energies. The second one arise from the vibrations and is approximated as -0.1 eV per oxygen. The last bracket corresponds to the entropic and enthalpic contributions (keep one digit) from O_2 and H_2O. This equation gives ΔG values for the simplest case – an isolated epoxide or a hydroxyl group chemisorbed on graphene – of 1.1 eV and 1.6 eV, respectively. The results indicate that graphene layers with sparse and homogeneous epoxide and hydroxyl functionalizations are thermodynamically unstable at T=300 K and p=1 bar. Oxygen species on the carbon layer are prone to dissociate as gaseous molecules.

The kinetics of the decomposition process is largely controlled by the diffusion of oxygen functional groups. As discussed in Chapter III, the diffusion barriers for individual epoxide and hydroxyl groups on graphene are around 0.8 eV and 0.5 eV, respectively. The vibrational frequencies for the two species are on the order of 10^{13} per second. Based on the harmonic transition state theory (for 1D case), the migration rates for epoxide and hydroxyl species at T=300 K are approximately 0.01 and 10^4 hops per second, respectively. These rough values provide an idea of how fast the functional groups diffuse on graphene. In reality, energy barriers may be affected by neighboring species, the buckling of carbon

planes, and defects in the material, and hence the diffusion rates can be largely different. Further research is necessary for better understanding the influence of the local chemical and physical environment in GO on the migration rates of oxygen functionalities.

4.2.2 Dimeric oxygen species on graphene

4.2.2.1 Decomposition reactions

The diffusion of epoxide and hydroxyl groups provides the chance that they can meet the other oxygen species and make reactions. Possible decomposition reaction pathways between dimeric epoxide-epoxide (O-O), hydroxyl-hydroxyl (OH-OH) and epoxide-hydroxyl (O-OH) species are investigated by CI-NEB (DFT) calculations, with 11 images mimicking the MEP (Figure 18). The Gibbs energy of formation is calculated by using Equation (119). Results show that association of two individual oxygen functionalities into dimeric species increases the stability of the system. However, the chemisorbed oxygen species are still unstable compared to the gaseous molecules.

At mild temperatures, the most efficient decomposition pathway is the reaction from two -OH groups on one side of graphene to the formation of a H_2O molecule and an -O- group on graphene (Figure 18(b)). The reactions are exothermic by 0.4 eV and 0.6 eV, for the two -OH reactants in ortho- and para-position, involving activation energies of 0.5 eV and 0.4 eV, respectively (atomic configurations are shown in Figure 22). Formation of O_2 from two -O- groups on graphene (Figure 18(a)) is an alternative route for decompositions, but it is much slower at mild temperatures, and it involves electronic transitions. In particular, the reaction involves a first energy barrier of 1 eV for the two -O- groups to get close enough to make a bond, and then another barrier of 0.6 eV for the bonded oxygen to desorb as a gaseous molecule (Figure 19). The whole reaction is exothermic by 1.6 eV, assuming the O_2 product is in the triplet state. I used spin-polarized DFT to locate the crossing point of the singlet and triplet potential energy surfaces (PES) of this reaction process (Figure 19). The spin conversion is found to occur during the desorption of the oxygen molecule. The probability of the single-to-triplet transition can be estimated based on the Landau-Zener theory [61, 86, 131]

$$p_{s-t} = 2\left[1 - \exp\left(-\frac{V^2}{hv|F_s - F_t|}\right)\right], \tag{120}$$

where V is small perturbation coupling the two PESs, and I used for V the spin-orbit matrix element [68] of 122 cm^{-1} between the singlet and triplet states for O_2. h is Planck constant. v is the velocity of O_2 and can be estimated using Maxwell-Boltzmann distribution at T=300 K. F_s and F_t are the slopes of the two PESs at the crossing point. The probability is finally obtained as about 0.004 per passage. As O_2 in the singlet state has higher energy than one in the triplet state by about 0.4 eV, formation of O_2 becomes less energetically favored due to the poor rate of spin conversion, and in some cases (reaction within oxygen agglomerates)

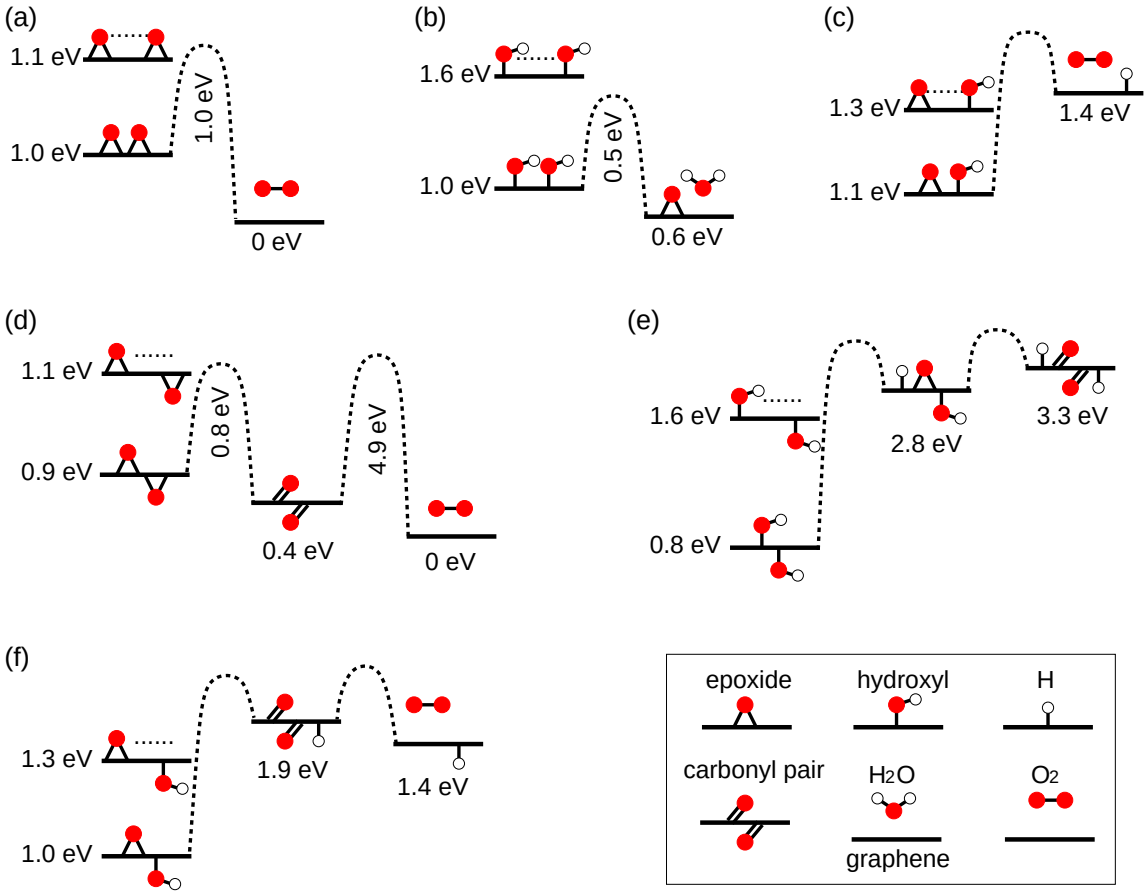

Figure 18: Binary decomposition reactions between epoxide and hydroxyl groups on one side or on both sides of graphene. Energy values correspond to ΔG per oxygen functional group computed via Equation (119). Relevant energy barriers are obtained by NEB-DFT calculations.

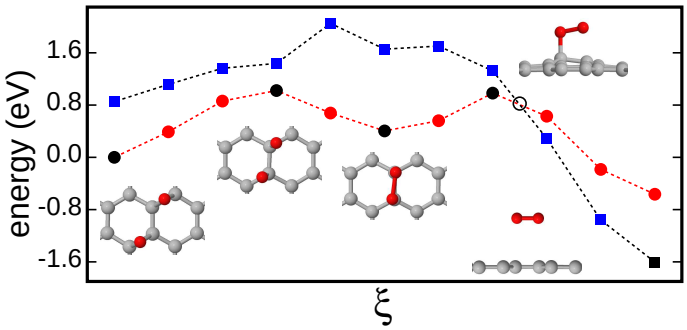

Figure 19: The energy profile and optimized atomic configurations in the reaction process to the formation of a O_2 molecule from two epoxide groups on graphene, by NEB-DFT calculations. The red and blue curves are the potential energy surfaces for the two oxygen in singlet and triplet state, respectively. The zero energy level is shifted to the energy of the initial system in singlet state. The atomic configurations of the initial state, transition states, metastable state, and final state are shown next to their corresponding energy points marked by the black filled symbols. The crossing point of the two potential energy surfaces is circled.

may be endothermic as that will be discussed later.

All the other reactions ((Figure 18 (c), (e) and (f)) are endothermic involving large energy barriers, and thus are unlikely to occur at mild temperatures. In particular, the reaction from two -O- groups on the opposite sides of graphene leads to the formation of a carbonyl pair (Figure 18(d)). This reaction is exothermic by 0.8 eV, and involves an activation energy of about 0.8 eV. Further transformation from a carbonyl pair into a O_2 molecule needs to overcome a barrier as large as 4.9 eV, comparable to the energy costs for oxygen species breaking through the graphene network and switching the side onto which they are chemisorbed. Therefore, formation of stable intermediate species such as carbonyl and ether groups are the factors that hinder a complete reduction of GO materials [3].

4.2.2.2 Pair-wise association energies

In energetic terms, Figure 18 also suggests that large attractions exist between oxygen species staying in close proximity to each other. To explore these interactions, I calculated the association energy ΔE for O-O, OH-OH and O-OH dimers in all possible atomic configurations, with the two oxygen units separated by up to four C=C bonds (Figure 20, 21, 22 and 23). The association energy ΔE is defined as

$$\Delta E = E(g + I_1 + I_2 + \cdots + I_N) - \left[\sum_{i=1}^{N} E(g + I_i) - (N-1)E(g)\right] , \qquad (121)$$

where $E(g + I_1 + I_2 +, \cdots, I_N)$ is the energy of a graphene layer chemisorbed by N amount of oxygen functional groups in a specific configuration. $E(g + I_i)$ is the energy of an isolated oxygen species chemisorbed on graphene. E(g) is the energy of pristine graphene. Therefore

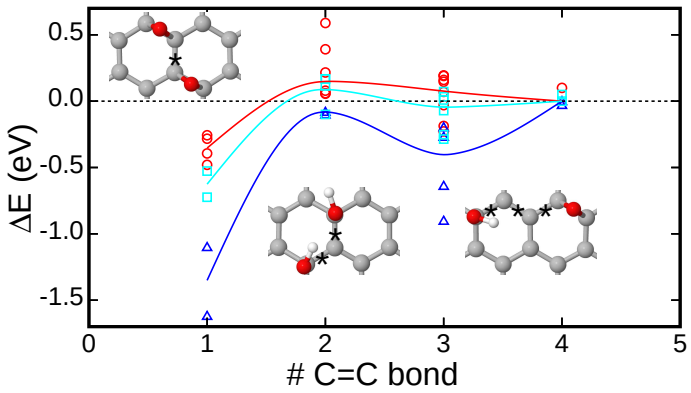

Figure 20: Pair-wise association energy (symbols) of binary epoxide-epoxide (red), hydroxyl-hydroxyl (blue), and epoxide-hydroxyl (cyan) complexes on graphene with the two oxygen species separated by up to 4 C=C bonds. Energy values are referred to that of two isolated oxygen units on graphene. Insets show examples of binary complexes having functional groups separated by one, two, and three C=C bonds (asterisks). Detailed energetic information and atomic configurations are shown in Figure 21, 22 and 23. Solid lines are guide to the eye.

ΔE measures the energy gain by bringing the oxygen functionalities from where they are infinite distant away from each other on graphene to that specific configuration.

The overall interactions between two oxygen species exhibit damped-oscillative behaviors with respect to the number of C=C bonds separated between the two oxygen units (Figure 20). In particular, pairs of functional groups in the first-nearest neighbors (C=C bond equal to one) experience the largest attractions. The attractions are stronger for two oxygen species on the opposite sides of graphene than those on the same side. O-O and O-OH pairs feel repulsions when the two oxygen units are separated by two and three C=C bonds. For instance, an O-O pair with the two -O- groups staying in one hexagon facing each other induce large strains in the underlying carbon plane, resulting in repulsions of 0.4-0.6 eV (Figure 21). These interactions are short-ranged and quickly decay to negligible values when two oxygen species are separated by four C=C bonds. On the average, the attractions in OH-OH pairs are stronger than that in O-OH pairs, which in turn are larger than that in O-O pairs.

The interactions between oxygen functional groups are the results of non-trivial competition of strains in the graphene plane and electronic effects, such as the charge redistribution over the oxygen species and the carbon backbone. For two dimeric oxygen groups staying at same distance but in different relative positions, the association energies are scattered over wide energy intervals (up to 0.5 eV). It may become even more complicated for a trimer, a tetramer and big clusters of oxygen functionalities on graphene. At mild temperatures, these interactions govern the transportation of epoxide and hydroxyl groups on graphene. In particular, large attractions drive oxygen species to aggregate on graphene, providing

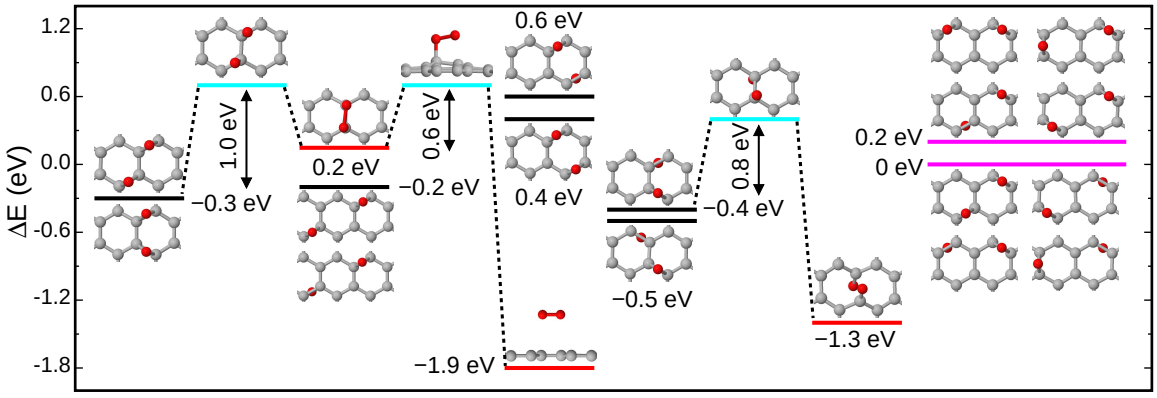

Figure 21: Pair-wise association energy of epoxide groups on graphene. The atomic configurations are shown next to their corresponding energy levels indicated by line segments. Cyan colored line segments represent the transition states leading to the formation of either a O_2 molecule (left) or a carbonyl-pair species (right).

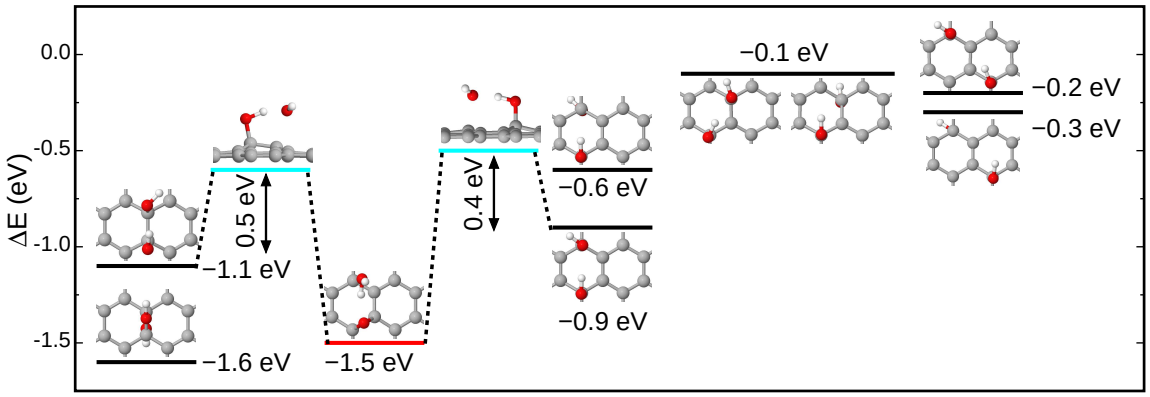

Figure 22: Pair-wise association energy of hydroxyl groups on graphene. Same as Figure 21; cyan colored segments indicate the transition states to the formation of a H_2O molecule and an epoxide species.

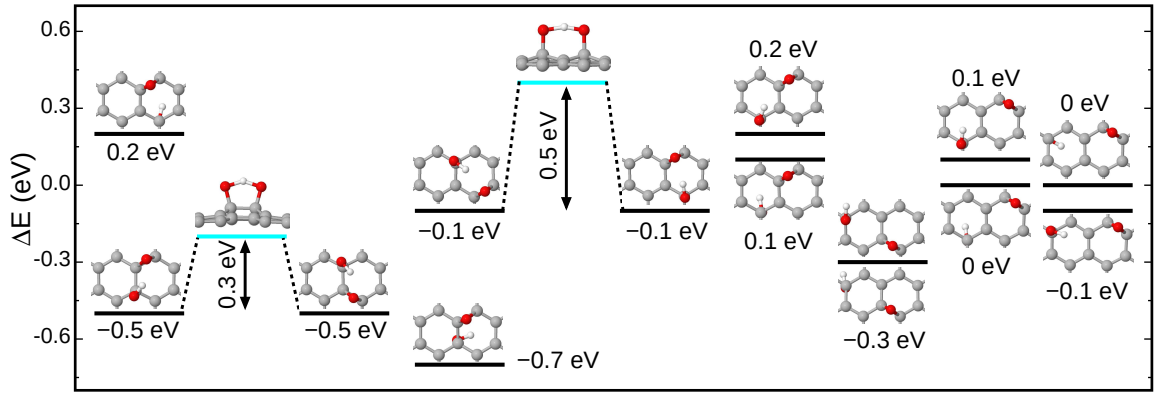

Figure 23: Pair-wise association energy of an epoxide and a hydroxyl group on graphene. Same as Figure 21; cyan colored segments indicate the transition states leading to proton transfer between neighboring hydroxyl and epoxide species.

the chance for making reactions. Therefore the interactions between oxygen functionalities are the origin of the metastable characteristics observed in the EGO films.

4.2.3 Graphene oxide with arbitrary chemical compositions

4.2.3.1 A simplistic energy scheme

For GO at high oxidation levels, DFT calculations become inefficient, as there are infinite ways to pattern the oxygen functionalities and large supercells are necessary for modeling the system. To overcome this obstacle, I developed a simple energy scheme to predict the energy of GO with arbitrary distributions of -O- and -OH species. The central idea is to assume a pairwise interaction between oxygen species [134]:

$$\Delta E^{(2)} = \sum_{I,J} E_{IJ,K} \ , \tag{122}$$

where $\Delta E^{(2)}$ represents the approximated association energy of a single-layer graphene functionalized with epoxide and hydroxyl groups in a specific configuration. $E_{IJ,K}$ is the binary association energies in Figure 21, 22 and 23, and the sum is taken over any pair of oxygen species IJ in relative position K in the system.

Meanwhile, I make two *ad hoc* corrections: First, mild repulsions in O-O pairs as indicated by magenta line segments in Figure 21 are excluded when applying Equation (122). Second, a penalty energy of 0.3 eV is added to each $E_{IJ,K}$ term for OH-OH complexes. The reason for the latter is that in agglomerates of three or more -OH groups on graphene, the orientation of each -OH group can not be as optimized as that in a dimeric situation. The energy could be lifted by as much as 0.3 eV when the orientation of a -OH group in a OH-OH pair is altered (Figure 24).

I tested this simplistic energy scheme for a large number of GO models, including trimeric and tetrameric oxygen functionalities on graphene, as well as crystalline structures at partial and fully oxidization levels. The approximated association energies $\Delta E^{(2)}$ based on the simplistic energy scheme (Equation (122)) are compared to the exact values ΔE obtained by DFT (Equation (121)) for these models. The results are summarized in Figure 25, and the full energetic information and atomistic structures are reported in Figure 26. With the two *ad hoc* corrections, Equation (122) predicts association energies with a mean absolute error of less than 0.1 eV per oxygen species compared with the DFT values (maximal error less than 0.2 eV per oxygen species). The comparisons show that the two corrections are necessary to account for – approximately and on average – the decreasing and increasing energies due to the strains and electronic effects in agglomerates containing more than two oxygen functional groups. Further investigations in the relation of the interactions between oxygen species with these complex factors are no doubt helpful for better description of GO systems.

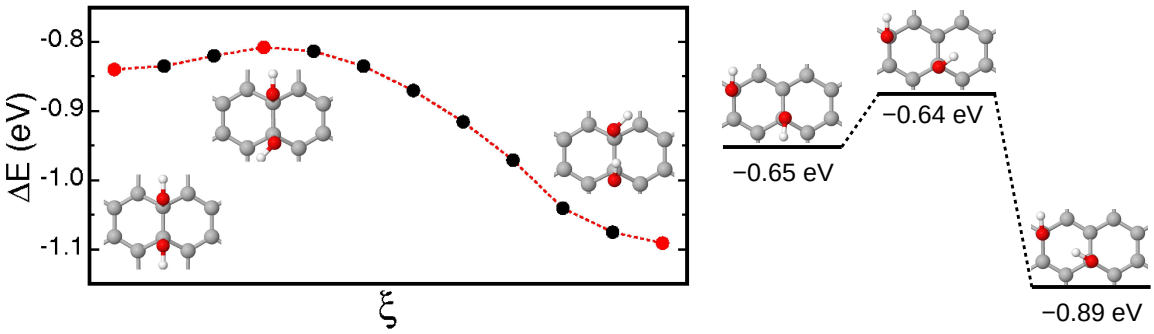

Figure 24: Role of O-H bond orientation on the association energy of two neighboring hydroxyl species. Left panel, energy profile obtained from NEB-DFT calculations of two -OH groups in ortho-position whose O-H bonds undergo rotations in the plane parallel with the graphene layer. Optimized atomic configurations of the two stable configurations and the transition state are shown next to their corresponding energy points indicated by red discs. Right panel, stable configurations of two -OH groups in para-position showing different relative orientations of O-H bonds by DFT calculations. All the energy values are referred to that of two isolated -OH groups on graphene.

This energy scheme provides a simple and convenient route to estimate the energy of a single-layer graphene with arbitrary epoxide and hydroxyl functionalizations. It better applies for EGO systems, which present well-structured carbon layers, and include minimal defects and defected oxygen species (such as carbonyl, carboxyl, and ether groups).

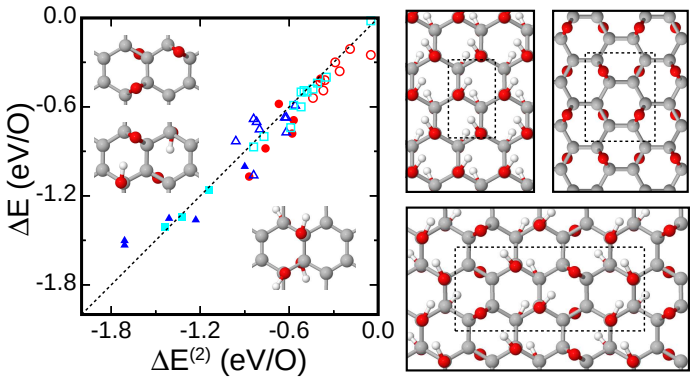

Figure 25: Association energy of single-layer graphene with epoxide-only (red), hydroxyl-only (blue), and mixed epoxide-hydroxyl (cyan) functionalizations as computed by both DFT (ΔE) and the simplistic energy scheme ($\Delta E^{(2)}$). Filled and empty symbols refer to crystalline structures, and small clusters of trimeric and tetrameric oxygen species on graphene, respectively. Selected model structures are shown as insets and on the right side. Full information is reported in Figure 26.

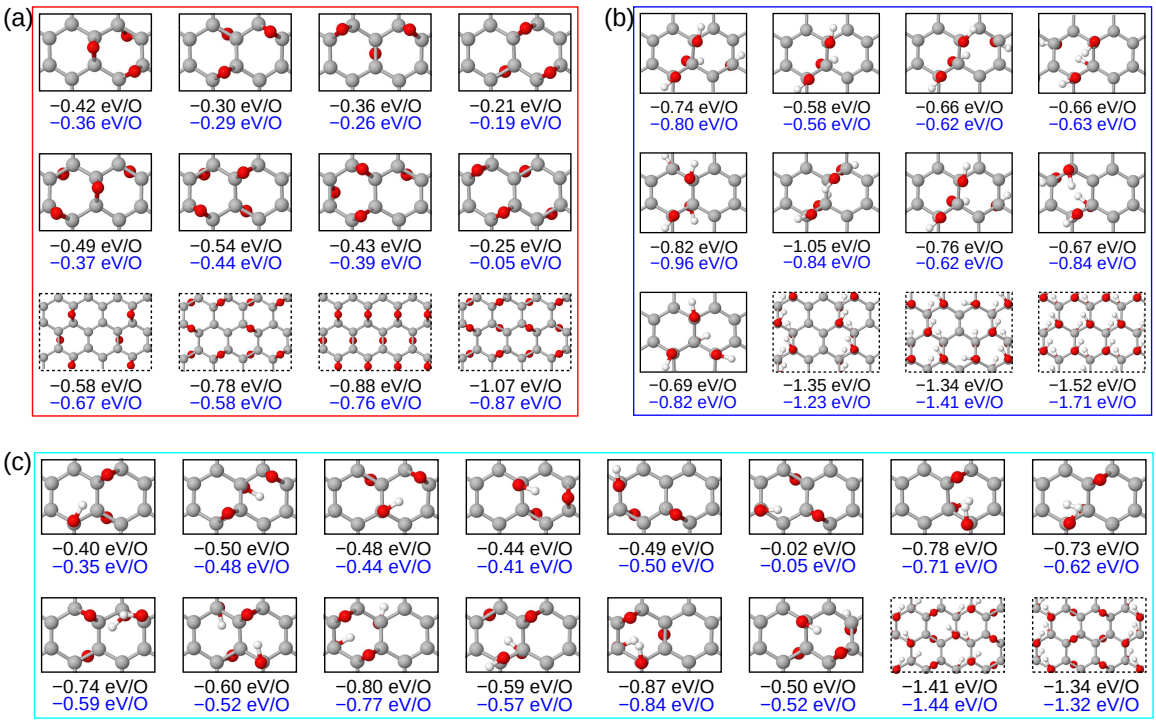

Figure 26: Association energies per oxygen species obtained by DFT (black) and the simplistic energy scheme based on Equation (122) (blue) for single-layer graphene with (a) epoxide-only, (b) hydroxyl-only, and (c) mixed epoxide-hydroxyl functionalizations. Models of crystalline structures (enclosed in dashed boxes) have O:C ratios of – from left to right – in (a) 0.25, 0.375, 0.5 and 0.5; in (b) 0.5, 0.75, and 1.0; and in (c) 0.75 and 0.67, with hydroxyl:epoxide ratios of 2:1 and 1:1, respectively.

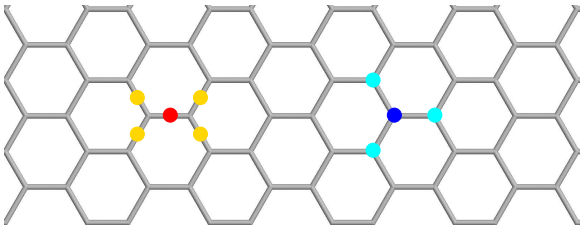

Figure 27: The stable configurations of an epoxide (red sphere) and a hydroxyl group (blue sphere) on graphene lattice. The four nearest-neighbor stable sites are marked by orange spheres for the epoxide group. The three nearest-neighbor stable sites are marked by cyan spheres for the hydroxyl group.

4.2.3.2 A lattice-model Monte Carlo method

To study the chemical and kinetic stability of EGO, I used a lattice-model Monte Carlo method to mimic the aging process in the EGO films, and to generate the quasi-equilibrium intralayer structure of the oxidized layers. To do that, I considered a single-layer graphene functionalized with selected number of epoxide and hydroxyl groups. I used a canonical ensemble to calculate the properties of EGO systems (Equation (100) and (101)). I implemented the Metropolis algorithm to generate ensembles of EGO structures satisfying the distribution given by Equation (101). The energy of EGO $E(\xi)$ at any given configuration ξ was evaluated based on the simplistic energy scheme mentioned earlier.

The details of this method is as follows. I used a periodic supercell of a single-layer graphene including 12×21 unit cells to achieve good statistics and to eliminate surface effects. Selected number of epoxide and hydroxyl groups are initially randomly distributed on the graphene layer. The oxygen functionalities are only allowed to stay at their stable sites – an epoxide group bridges two nearest-neighbor C atoms, and a hydroxyl group stays on the right top of a C atom (Figure 27). For each Monte Carlo step, one oxygen functional group is randomly picked, and makes a trial jump to one of its nearest-neighbor stable sites. Epoxide and hydroxyl groups are picked at equal probabilities, assuming their diffusion rates on graphene are approximately the same (considering the hydrogen proton in a hydroxyl group can transfer to a neighboring epoxide group). The probability of accepting the trial jump, according to Equation (101) and (103), is given by

$$P_{\xi,\xi'} = \begin{cases} 1, & \Delta E \leq 0 \\ exp\{-\beta \Delta E\}, & \Delta E > 0 \end{cases} \tag{123}$$

where $\Delta E = E(\xi') - E(\xi)$ is the energy change of the EGO system upon the movement of the selected oxygen species (I). ΔE is obtained based on the simplistic energy scheme (Equation (122)), by computing the interactions of the selected species I with all the other

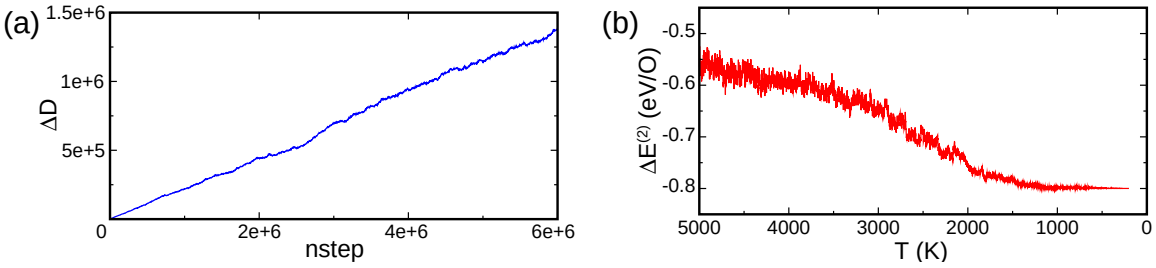

Figure 28: (a) Total square displacement vs. Monte Carlo steps of epoxide groups on a lattice model during the melting process at T=5000 K. The system is considered to be completely melted when the average displacement per oxygen species is over half of the supercell dimension. (b) Energy of a EGO model calculated by Equation (122) vs. T during the quenching process.

species J (and J') in the system before (and after) the move, via

$$\Delta E = \sum_{J'} E_{IJ',K'} - \sum_{J} E_{IJ,K} \ , \tag{124}$$

where the sum is taken over all the oxygen species except for the selected one I. The ensemble that attains equilibrium will in principle consist of EGO structures following the normalized Boltzmann distribution (Equation (101)) at a given temperature.

Direct applying the above algorithm at T=300 K takes a long time for the EGO system to reach equilibrium, as the transition of EGO from one local energy minima to another involves barriers much larger than the thermal energy. To accelerate the simulations, I used a simulated annealing strategy. While the above algorithm still applies, the oxygen functionalities of the system are first randomized at high temperatures (above the melting temperature – 5000 K for graphene with epoxide-functionalizations, and 10000 K for graphene with hydroxyl- or mixed epoxide-hydroxyl functionalizations). Then restarting from the melted structure, the system is slowly quenched from that high temperature to 200 K (Figure 28). In this simulated annealing process, only diffusion of oxygen functional groups is allowed, while decomposition reactions are not permitted. Therefore this strategy does not change the physics of the EGO system. This strategy evolves the system toward lowest energies (which have dominant weights in the canonical average), and it mimics a long-time aging process in the EGO films at mild temperatures (T$\leq$ 70 °C). The obtained equilibrium structures can be considered as the intralayer structures of our aged EGO films.

I used this lattice-model Metropolis Monte Carlo method combined with the simulated annealing strategy to generate EGO models at different oxidation levels, and including various fractions of epoxide and hydroxyl groups.

4.2.3.3 Intralayer structure and stability of aged EGO

The intralayer structures of aged EGO models obtained by the MC simulations as well as their chemical stabilities are reported in Figure 29. The Gibbs free energy of formation is calculated via

$$\Delta G = \Delta E + N_e \mu_e + N_h \mu_h \ , \tag{125}$$

where ΔE is the association energy defined in Equation (121), and μ_e and μ_h are the Gibbs free energy of formation for a single epoxide and a hydroxyl group on graphene, respectively, with respect to gaseous O_2 and H_2O at T=300 K and p=1 bar. As the association energy can be estimated by using the simplistic energy scheme (Equation (122)), the Gibbs free energy of formation is approximated as

$$\Delta G^{(2)} = \Delta E^{(2)} + N_e \mu_e + N_h \mu_h \ . \tag{126}$$

The MC simulations show that aging at mild temperatures leads to a non-homogeneous phase in the EGO models consisting of highly oxidized domains, which present local order and long-range disorder, surrounded by pristine graphene regions. For EGO with epoxide-only or hydroxyl-only functionalizations (Figure 29(a) and (b)), the chemical stability of the system increases with the O:C ratio, and reaches equilibrium with gaseous O_2 and H_2O at T=300 K and p=1 bar in the case of fully oxidized crystalline structures (Figure 30). The agglomeration of oxygen functionalities enhances the chemical stability of EGO. To show this, I calculated ΔG (Equation (125)) of selected EGO models with homogeneous oxidation (black curves in Figure 29(a) and (b)). In detail, I chose the structures in Figure 26(a) and (b), including a monomer, dimer, trimer and tetramer of epoxide or hydroxyl groups on graphene, as well as crystalline structures with O:C ratios of 0.25, 0.375 and 0.5 for epoxide-functionalization, and 0.3, 0.5, 0.67, 0.75 and 1.0 for hydroxyl-functionalization. Results show that the homogeneously oxidized graphene layers have increasing chemical stability with the O:C ratio, and they are less stable than the MC models with inhomogeneous oxidation at the same O:C ratio.

In the case of mixed epoxide-hydroxyl functionalizations (Figure 29(c)), I considered two O:C ratios – 0.3 and 0.4, with various relative fractions of -O- and -OH groups. Strong OH-OH attractions lead to the phase segregation: formation – within the highly oxidized domains – of regions rich in -O- and -OH species, with maximized boundaries between the two regions. The chemical stability of EGO increases with the fractions of -OH groups at a certain oxidation level.

The agglomeration of oxygen species also influences the kinetic stability of EGO. Even though the aged and partially oxidized EGO remains unstable with respect to the gas phase, the decomposition reactions are inhibited by the local order of the highly oxidized domains (Figure 31). By analysis of the EGO models obtained from MC simulations, I

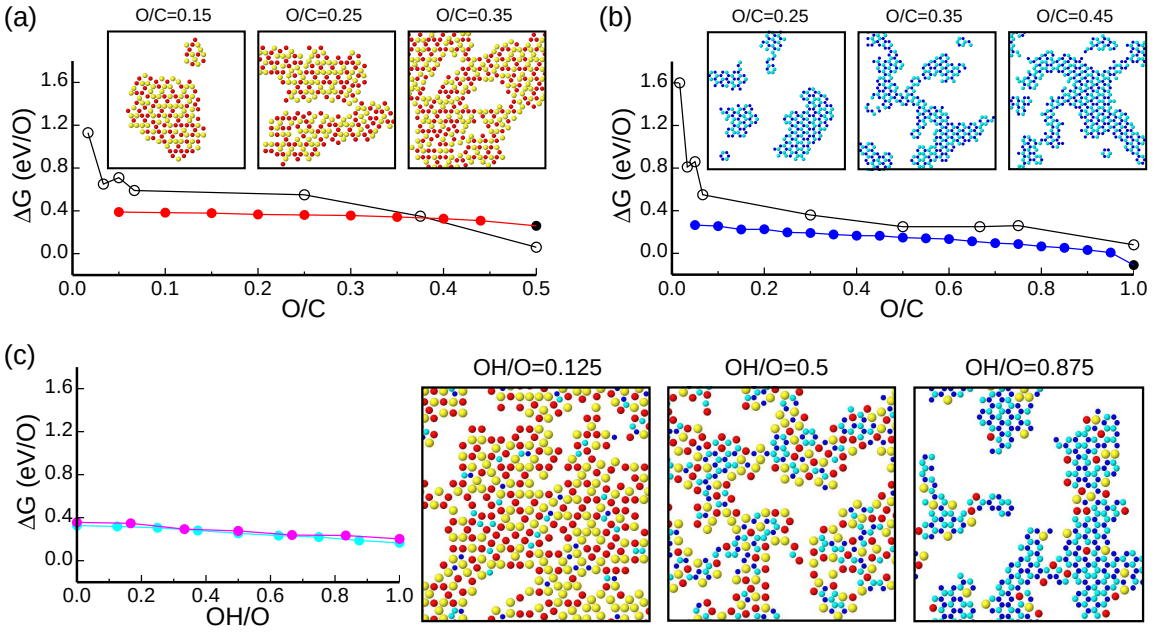

Figure 29: (a) ΔG (per oxygen species) of single-layer graphene with epoxide functionalization. Black and red symbols show ΔG of hand-made structures calculated by DFT (Equation (125)), and EGO models generated by Monte Carlo simulations (Equation (126)), respectively. Selected EGO models from MC simulations are shown as insets: red and yellow discs represent -O- groups facing upward and downward the graphene plane, respectively; the graphene lattice is not shown. The black filled disc is evaluated by Equation (126) using the model structure shown in Figure 30(a). (b) Same as (a) for hydroxyl-functionalized graphene. In the insets, -OH species facing upward and downward the graphene plane are shown in blue and cyan, respectively. The black filled disc is evaluated using the model structure shown in Figure 30(b). (c) ΔG of mixed epoxide-hydroxyl functionalized graphene by MC simulations, with O:C ratios of 0.3 (magenta) and 0.4 (cyan). Insets show selected models with an O:C ratio of 0.4 and different relative fractions of -OH and -O- groups (OH/O refers to the fraction of -OH groups relative to the total amount of oxygen).

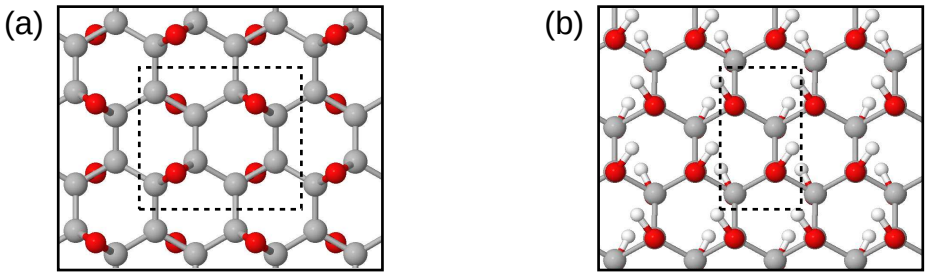

Figure 30: Crystalline structure of graphene fully covered by (a) epoxide and (b) hydroxyl groups. Dashed boxes indicate the primitive unit cells. These two phases are found to be most energetically favored in the proposed single-layer GO models [108, 128].

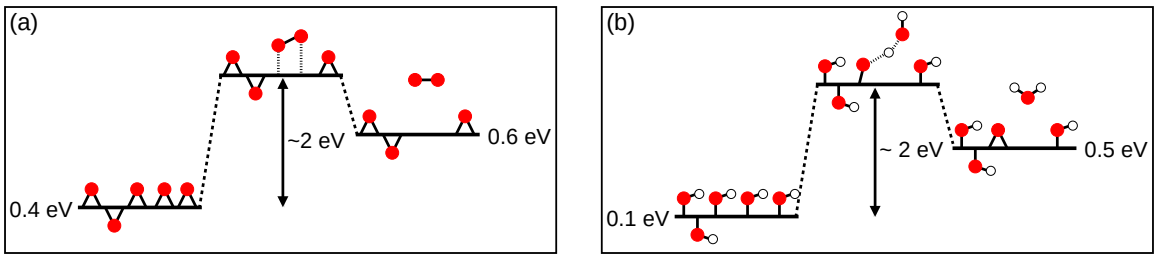

Figure 31: (a) Schematic energy diagram of the binary reaction from two epoxide groups embedded in highly oxidized domains in aged EGO. ΔG (per oxygen species) of reactants and products correspond to the averages extracted from the aged EGO models with epoxide-functionalization generated by Monte Carlo simulations. (b) Same as (a) in the case of two hydroxyl groups embedded in highly oxidized regions of aged EGO with hydroxyl-functionalization. The activation energies are extracted from NEB-DFT calculations based on the models in Figure 32.

found that the reactions from two nearest-neighboring -O- or -OH groups within oxygen agglomerates and on the same side of graphene become – on average – endothermic by about 0.6 eV and 0.8 eV, respectively, due to the large attractions from the oxygen species close to the reactants. NEB calculations show that the activation energies for these reactions are elevated to as large as 2 eV (details are discussed in the next section). Also as functional groups favor staying on the opposite sides of graphene with respect to their neighbors, the spatial correlation reduces the fractions of -O- and -OH groups eligible for making reactions to about 0.3 and 0.2 (referred to the total oxygen content), respectively.

These results reveal that the origin of the kinetic stability of EGO arises from the interactions between oxygen species. Sparsely and homogeneously functionalized graphene layers are thermodynamically unstable in ambient conditions. The attractions between oxygen functionalities drive the oxygen species to aggregate on the carbon plane, providing the chance for encounter and making decomposition reactions. As the oxygen species form agglomerations on graphene, the reactions to the formation of O_2 and H_2O are in turn hindered by both energetic and geometrical factors. Therefore the material is stabilized through this aging process.

4.2.3.4 Comparison with DFT models

To support the picture (Figure 31) obtained by Monte Carlo simulations, I performed DFT calculations on two model structures (Figure 32). Model (a) is a single-layer graphene with mixed epoxide-hydroxyl functionalizations, having an O:C ratio of 0.42, and fractions of -OH and -O- groups equal to 0.17 and 0.25, respectively. Model (b) is a single-layer graphene with epoxide functionalizations, with an O:C ratio of 0.25. Six pairs of oxygen species are selected from the two models, which are eligible for making reactions to form O_2, H_2O or a carbonyl pair. The energy barriers of these reactions are calculated by using the CI-NEB

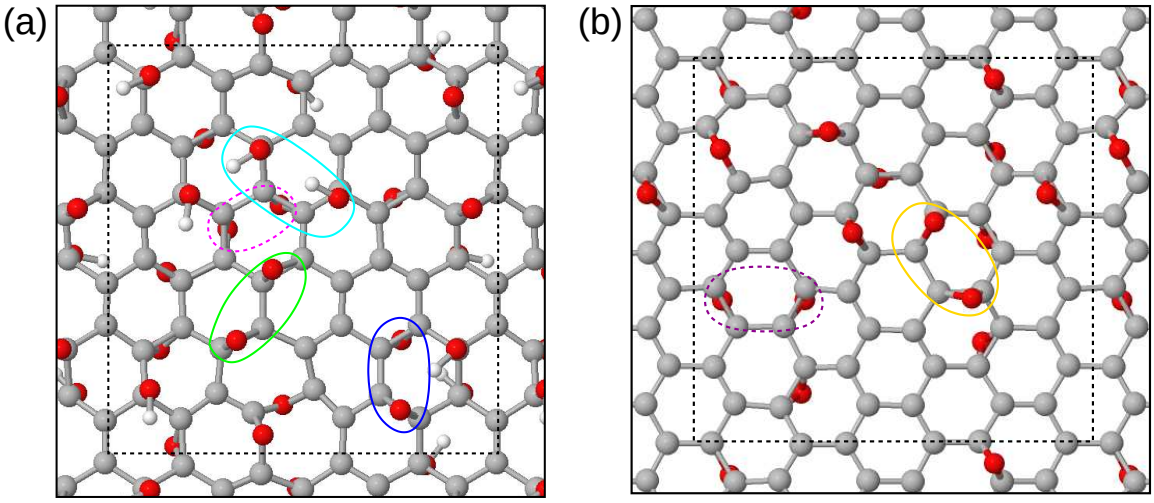

Figure 32: Single-layer EGO models generated by DFT. (a) A EGO model with an O:C ratio of 0.42 (fractions of hydroxyl and epoxide groups are 0.17 and 0.25, respectively). (b) A EGO model with an O:C ratio of 0.25 including epoxide groups only. The dashed frames indicate the supercell used in DFT calculations. Colored ellipses show selected pairs of oxygen species, which are eligible for the reactions to form O_2, H_2O (cyan), and a carbonyl-pair (blue), for computing the energy barriers using the NEB method.

(DFT) method. For each case, the energy change of the system upon the reaction obtained by DFT is compared to that estimated by the simplistic energy scheme based on Equation (122) (Figure 33).

NEB calculations show that the reaction from two -OH groups embedded in oxygen agglomerates (Figure 33(a)) to the formation of H_2O leads to an increase in energy of the system by 1.3 eV, and involves an energy barrier of 1.7 eV. The simplistic energy scheme estimates the energy change of the system upon the reaction as 1.3 eV, the same as the DFT value. Furthermore, the energy scheme shows that the total attraction between the two -OH reactants and their neighboring oxygen species is as large as -3.5 eV, while the energy gain by forming a H_2O molecule and an -O- group is only -2.2 eV. Consequently, the decomposition reaction is endothermic, and the activation energy becomes larger than that of the reaction in sparsely oxidized regions (0.5 eV, Figure 18(b)) due to the attractive forces.

For reactions to the formation of O_2, I chose reactants in different local environment. Figure 33(b) indicates two -O- groups in the interior of oxygen agglomerates. NEB calculations show that the reaction from these two -O- species is endothermic by 0.2 eV, and the energy barrier is 1.6 eV. The simplistic energy scheme gives the energy change of the system upon the reaction as 0.7 eV, which is qualitatively in good agreement with the DFT result. On the contrary, the two -O- groups on the surface of oxygen agglomerates (Figure 33(c)) feel less attraction – only -1.4 eV, given by the simplistic energy scheme, while their

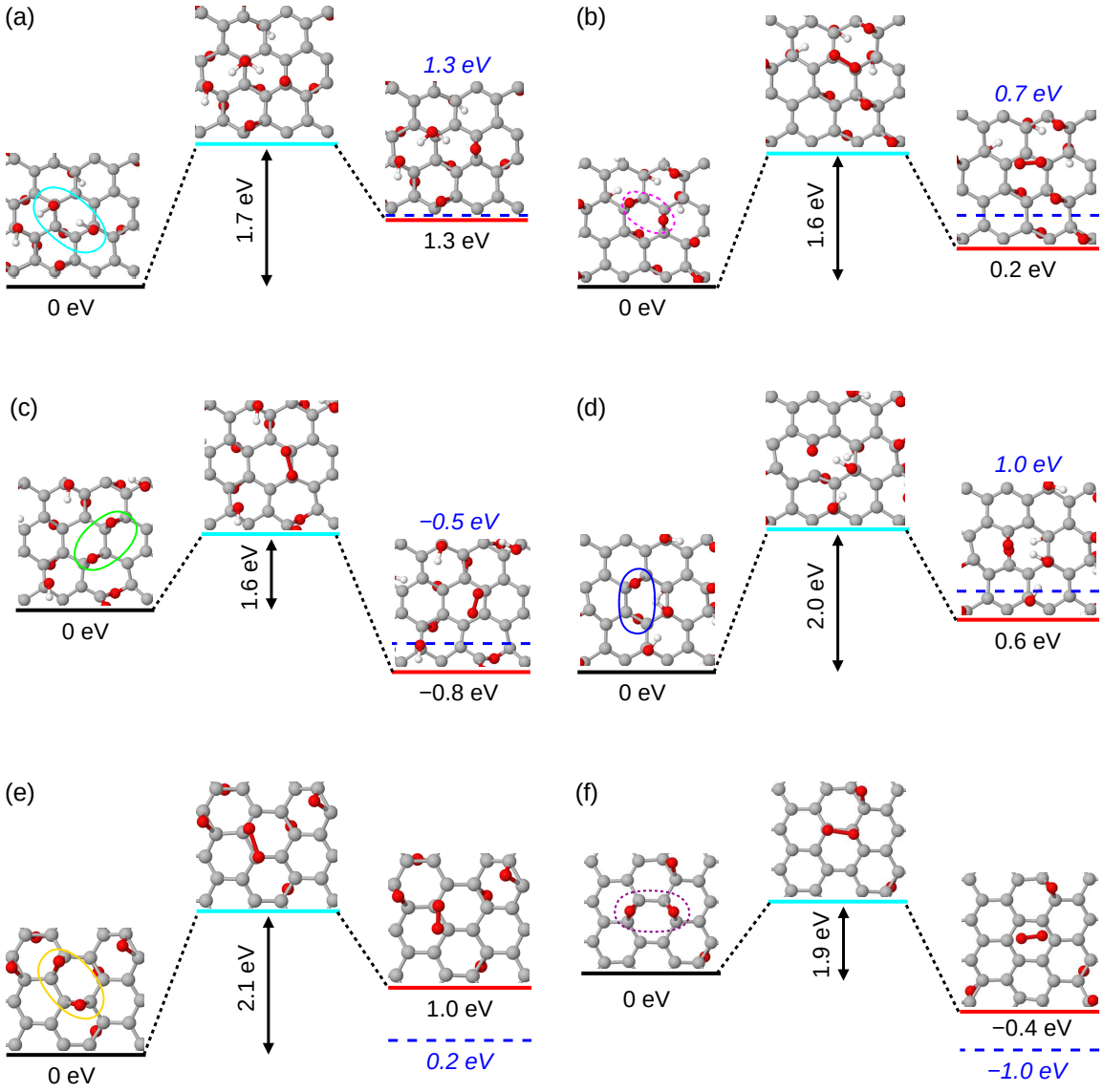

Figure 33: NEB-DFT calculations of reactions in EGO models in Figure 32: (a) Two -OH groups forming a H_2O molecule and an -O- group. (b), (c), (e) and (f) Two -O- groups forming a O_2 molecule. (d) Two -O- groups forming a carbonyl pair. Line segments show the energy levels of reactants (black), transition state (cyan), and products (red). The corresponding energy values (in black) are shown below the line segments. Blue dashed line segments and energy values in blue indicate the energy of products estimated by the simplistic energy scheme based on Equation (122). All the energies are referred to that of the initial state in each case.

reaction to the formation of O_2 yields an energy gain of -1.9 eV. Therefore the decomposition reaction is energetically favored by 0.5 eV, consistent with the DFT result of 0.8 eV. Similarly, the reaction is exothermic when the two -O- reactants stay in a highly oxidized region (Figure 33(e)), and is endothermic in the region of dilute oxidation (Figure 33(f)).

Reaction to the formation of a carbonyl pair also becomes energetically unfavored in agglomerates of oxygen functionalities. NEB calculation shows that the energy of the system increases by 0.6 eV upon the reaction, and the activation energy is as large as 2 eV. The simplistic energy scheme gives an energy change of the system as 1.0 eV, close to the DFT value.

These DFT calculations corroborate the picture given by the Monte Carlo simulations (Figure 29) that the aggregation of oxygen species enhances the chemical and kinetic stability of EGO systems. Reactions within highly oxidized domains become endothermic, and the energy barriers are increased significantly compared to that of the reactions in sparsely oxidized regions. The attractions between oxygen functionalities are the origin of the metastability of EGO. Meanwhile the DFT results validate the simplistic energy scheme. Equation (122) yields estimated energies qualitatively in good agreement with the DFT values.

4.3 Summary of main results

In this chapter, I investigated the origin of the metastability of EGO, the intralayer structure, and the chemical and kinetic stability of this material at T=300 K and p=1 bar, based on DFT calculations and Monte Carlo simulations. Studies show that graphene with sparse and homogeneous functionalization is unstable in air in ambient conditions. Oxygen species are prone to dissociate as H_2O and O_2 molecules, through internal reactions – most efficiently – from two neighboring hydroxyl or two epoxide groups on one side of graphene. Large attractions are found to exist between oxygen species in close proximity to each other, and they are the driving forces for functional groups to aggregate on graphene, providing the chance for encounter and making reactions. MC simulations show that the aging process at mild temperatures leads to a non-homogeneous phase in EGO consisting of highly oxidized domains surrounded by pristine graphene regions. The chemical stability of EGO increases with the O:C ratio, nearly reaching equilibrium with the gaseous atmosphere of O_2 and H_2O for the ordered and fully oxidized layers. Although partially oxidized EGO remains unstable with respect to the gas phase, further reactions are hindered within the highly oxidized regions – the local order and spatial correlations reduce the percentages of epoxide and hydroxyl groups geometrically eligible for making decomposition reactions to 30% and 20%, respectively. The reactions for the eligible pairs of epoxides or hydroxyls become on average endothermic by about 0.6 eV and 0.8 eV, respectively. The energy barriers associated to the reactions, in the interior of oxidized domains, are elevated to as large as 2

eV. All these results indicate that the origin of the kinetic stability of EGO stems from the attractions between oxygen functionalities. These interactions stabilize energetically pairs of oxygen species susceptible to form O_2 or H_2O, rendering the decomposition processes endothermic and unlikely.

In the MC simulations, we made a few approximations. First, we considered epoxide and hydroxyl groups as the only oxygen functionalities on graphene. Defects such as carbonyl, ether, and carboxyl were omitted. This approximation is based on the experimental XPS spectra, which indicate that the EGO films contains little amount of carbonyl and carboxyl species (below 4%). They are at the edges of graphene sheets and are immobile [3]. The computed XPS spectra of EGO models also suggest that the concentration of ether groups in EGO is less than 4%. In addition, previous experimental studies show that these defected species are inert at temperatures up to 1000 °C [2, 3, 40]. Therefore, it is reasonable to assume that these chemical species are unlikely to participate in the diffusion or reaction processes occurring on the regular sp^2 regions of the graphene sheets. Second, we considered an initial configuration mimicking the structure of as-synthesized EGO consisting of a random distribution of epoxide and hydroxyl groups on graphene. This assumption relies on the facts that: (1) Raman measurements of the as-synthesized EGO films show a prominent D band with a broad G band, which is a fingerprint of the disorder in the films. (2) The C 1*s* XPS spectra of the EGO films show a broad peak of the C species bonded to epoxide or hydroxyl groups. This is an indication that the oxidized C species stay in various local environments rather than an ordered pattern. (3) The synthesis process of the EGO films involves aggressive chemical treatments, which is very likely to cause disorder in the oxide films. Third, we used a simulated annealing strategy to accelerate the MC simulations, and we assumed that the obtained equilibrium structure models the oxide layers of the EGO films aged at room temperature for a few months or annealed at mild temperatures ($\leq$ 70 °C). Recent experiments observed a homogeneous to non-homogeneous phase transition in graphene oxide under a mild thermal treatment ($50 - 80$ °C) [66]. This corroborates our findings based on the MC simulations.

In conclusion, these studies provide deeper insight into the metastability of EGO systems, and suggest that aging at mild temperatures is a nondestructive way to control the structure and properties of EGO.

CHAPTER V

THE INTERLAYER STRUCTURE OF EGO FILMS

As discussed in Chapter I (section 1.2.2), XRD and AFM measurements show that the EGO films preserve the order of the carbon lattice, number of layers, and spatial coherence lengths of the pristine EG films, and in ambient conditions, the interlayer separation of the well-registered oxidized layers is unexpectedly as large as 9-10 Å (Figure 4(b)). XPS and IR measurements indicate that the EGO films reach equilibrium structures with an O:C ratio of 0.38, and contain minimal fractions of water, estimated to be no larger than 10% with respect to the total number of C atoms [136]. These observations contrast the properties exhibited by conventional GO made by exfoliation of graphite oxide, whose interlayer distance is about 5-6 Å when the material contains little amount of water, and achieves >9 Å only when the material incorporates large and detectable quantities of water of more than 20 wt% [11, 20, 77].

In this chapter, I will interpret these experimental results by investigation of the origin of the large interlayer distances in the EGO films, and unraveling the interlayer structure of this material. In particular, I systematically studied the interlayer spacing of EGO models consisting of stacks of either homogeneously or non-homogeneously oxidized carbon layers, and incorporating various water contents, based on the DFT-D scheme.

5.1 EGO models with homogeneously oxidized layers

I first considered EGO models with graphene layers hosting a homogeneous distribution of epoxide and hydroxyl groups. In Chapter III, I built a total of seven such EGO models having an O:C ratio of either 0.44 or 0.38, with up to 8% water molecules intercalated in-between the oxidized layers (Table 5 and 6). In these models, the ones with little water exhibit interlayer distances of about 4.5 Å (model A, B, C, E and G). The models containing 8% water, and rich in epoxide groups and deprived of hydroxyl species (model D and F), have interlayer distances of only 4.7 Å, close to the dehydrated EGO models, and far less than the measured values of 9-10 Å in the EGO films.

To gain more insight in the relation of interlayer spacing of EGO with its oxidation level, fractions and distribution of oxygen functional groups, and the water content, I considered an additional EGO model (Figure 34). This model has an O:C ratio of 0.46, rich in hydroxyl groups (fraction equal to 0.28), and incorporating 10% water molecules. This model is generated by using the same strategy as that for the EGO models shown in Chapter III. The only difference is that instead of random distribution, the epoxide and hydroxyl groups

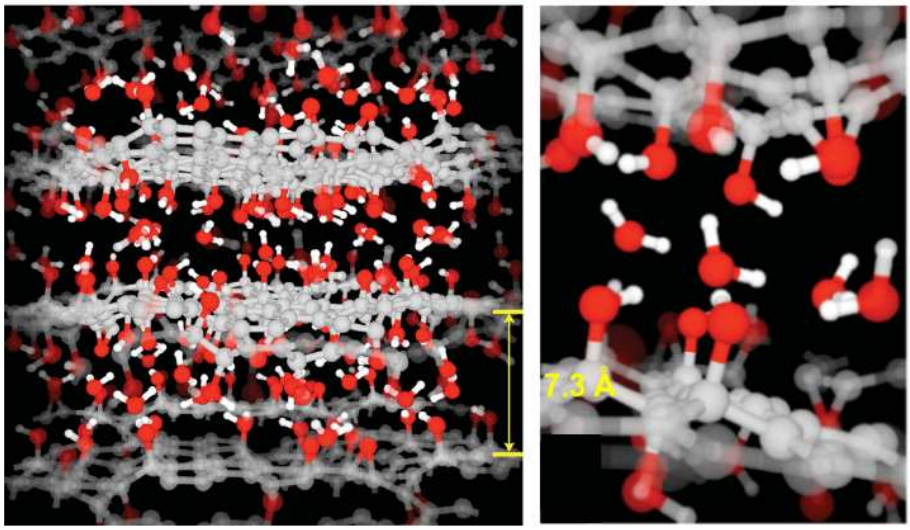

Figure 34: A EGO model generated by the DFT-D scheme, presenting a homogeneous lateral distribution of oxygen functionalities, with an O:C ratio of 0.46, fractions of epoxide and hydroxyl groups equal to 0.08 and 0.28, respectively, and a water content of 10%. The optimized structure shows an average interlayer spacing of 7.3 Å. Right panel, selected region of the EGO model showing a large concentration of hydroxyl groups and water molecules.

are arranged to form small agglomerates (sizes of agglomerates $\sim$ a few angstrom) on the graphene layers, and water molecules are initially intercalated in-between the oxygen agglomerates from the nearest-neighbor carbon layers. The model structure is fully optimized by the DFT-D scheme. The interlayer distance of this model attains 7.3 Å, due to the large concentrations of hydroxyl and water species, as well as the local aggregation of oxygen functional groups on the carbon layers. However, the spatial distribution of epoxide and hydroxyl groups is not compact and organized enough to form mechanically stable traps for water molecules bridging and holding nearest-neighbor layers at distances larger than 9 Å.

These results, consistent with the other experimental and theoretical studies of conventional GO, show that the interlayer distance of graphene oxide depends on the oxidation level, fractions and distributions of epoxide and hydroxyl groups, and the water content. These results also reveal that for graphene oxide systems consisting of homogeneously oxidized carbon layers with O:C ratios as much as 0.5, a water content up to 10% is insufficient to support a large spacing of 9 Å between the oxidized layers. Therefore the models with a homogeneous intralayer structure can not explain our XRD, AFM and IR results on the EGO films.

5.2 EGO models with non-homogeneously oxidized layers

The failure of EGO models with homogeneous oxidation inspires us that the aged EGO films may indeed present an non-homogeneous intralayer structure. Studies in Chapter

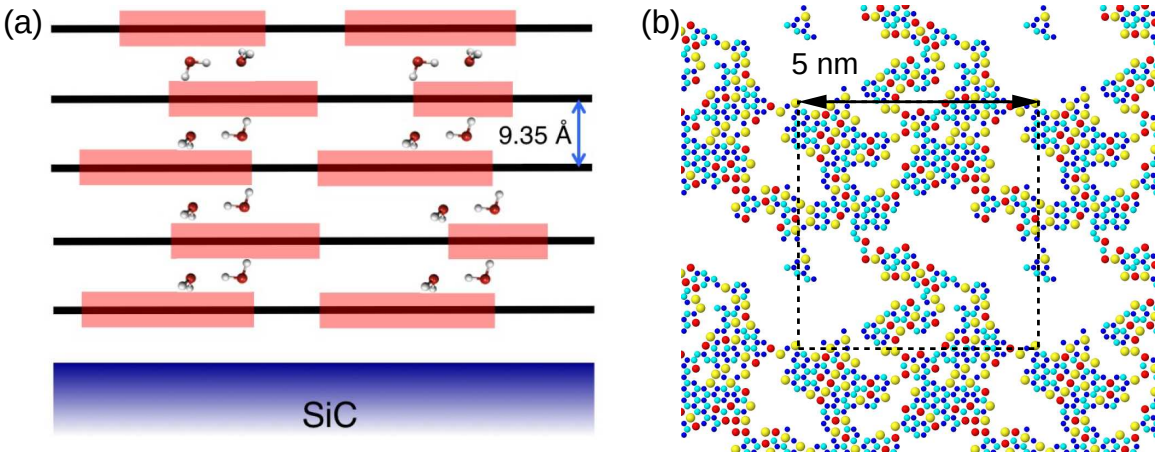

Figure 35: (a) Schematic representation of a multilayer EGO film consisting of non-homogeneously oxidized regions rich in hydroxyl species (red regions), and connected by trapped water molecules. (b) In-plane structure of aged EGO generated by Monte Carlo simulation as described in Chapter IV, with an O:C ratio of 0.38, and fractions of hydroxyl and epoxide species equal to 0.27 and 0.11, respectively. The dashed box indicates the supercell used in the simulation with dimensions of about 5 nm.

IV show that epoxide and hydroxyl groups are prone to aggregate on graphene due to the large attractions between oxygen species, such that aging or annealing at mild temperatures leads to phase segregation in EGO – formation of highly oxidized domains surrounded by pristine graphene regions. Figure 35(b) shows a graphene oxide layer presenting a realistic composition – an O:C ratio of 0.38, and fractions of epoxide and hydroxyl species equal to 0.11 and 0.27, respectively – generated by using the aforementioned Monte Carlo scheme in Chapter IV. The intralayer structure exhibits an interpenetrating network of highly oxidized and non-oxidized domains with nanometer dimensions. In multilayer EGO systems, these nanosized oxidized domains may be largely overlapped in the out-of-plane direction as illustrated in Figure 35(a), which may alter the mechanism for water molecules to be intercalated in the material, and hence influence the interlayer distance of EGO.

To understand the effect of this non-homogeneous intralayer structure on the interlayer separation of EGO, I considered simple models of periodic stacks of graphene layers fully covered by hydroxyl or epoxide groups (Figure 36 and 37). The in-plane structures adopt the ordered phases proposed by [128]. Models of "type 1" and "type 2" have graphene layers in "AA" and "AB" stacking geometries, respectively. Various fractions of water molecules – 0, 6.25%, 12.5% and 25% – are intercalated in-between the layers in each type of models. These structures represent the highly oxidized regions of the EGO films rich in hydroxyl or epoxide species, and the oxidized domains on the nearest-neighbor layers are connected by forming a hydrogen-bonding network through the intercalated water molecules. The DFT-D scheme is used to optimize the structure of these EGO models, and to calculate their interlayer distances.

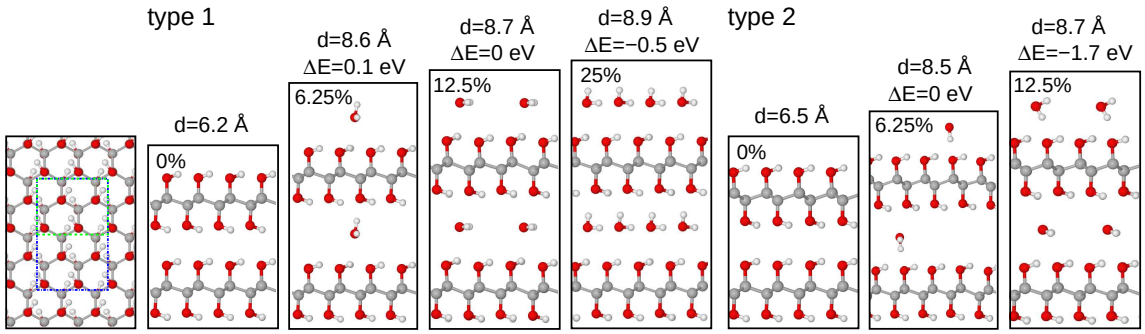

Figure 36: Periodic model structures of EGO films fully oxidized with hydroxyl groups including increasing amount of water. First panel on the left shows the in-plane structure of these models. The colored dashed rectangles indicate the planar dimensions of the supercells for the EGO models including 6.25% (blue), and 0%, 12.5% and 25% (green) of water. The optimized interlayer distances by DFT-D are reported on top of each model. In the case of the hydrated EGO models, the (zero-temperature and zero-pressure) enthalpy difference per water molecule (ΔE) between the hydrated and dehydrated structures is also reported. The structures on the left and right side present "type 1" and "type 2" stacking geometries, respectively.

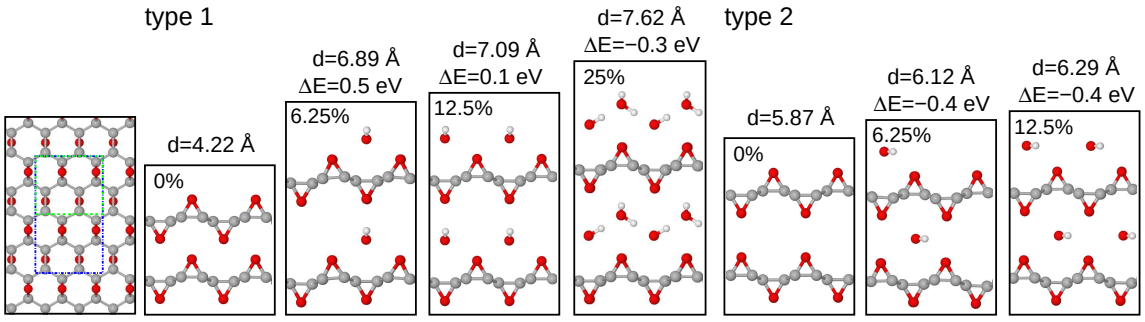

Figure 37: Same as Figure 36, for EGO models containing epoxide functionalities.

Calculations show that the EGO models with hydroxyl-functionalization and including no water exhibit zero-temperature interlayer distances of about 6.2-6.5 Å, with little dependence on the stacking order. By incorporation of 6.25% water, the interlayer spacing rises to 8.6 Å, significantly different from that of the dehydrated models, and increases very little for larger water contents. These results can be understood as that the highly oxidized domains rich in hydroxyl groups form rigid oxide layers on both sides of graphene planes with a mean thickness of 2 Å. Incorporation of even a small amount of water ($\leq$ 6.25%) leads to the formation of an additional water layer sandwiched between the oxidized carbon planes, and expands the interlayer spacing by over 2 Å. As long as the intercalated water molecules remain in a monolayer, increasing the water content does not affect much the interlayer distance.

On the other hand, an epoxide group bridges two carbon atoms with a mean height of only 1.4 Å. Consequently, EGO models with epoxide-functionalization have smaller interlayer distances than those with hydroxyl-functionalization, and the interlayer separation depends on both the stacking geometry and water content. In particular, models including no water present interlayer distances of 4.2 Å and 5.9 Å for "AA" and "AB" stacking, respectively. By including up to 25% water in these models, the interlayer distance reaches "only" 7.6 Å, due to the sparse distribution of epoxide species (compared to hydroxyl groups).

Trapping water molecules at oxidized regions of the multilayer EGO films is favored energetically. Figure 36 and 37 report the (zero-temperature and zero-pressure) enthalpy difference ΔE between the hydrated and dehydrated EGO models. ΔE is obtained by referring the energy of a hydrated model to that of a water molecule in vacuum and the dry model. These relative enthalpy values show that there is an enthalpic driving force leading water molecules in EGO to move away from non-oxidized regions and accumulate at oxidized regions of the lamellar film. Interestingly, the enthalpic driving force to expand interlayer separation and trap water molecules is larger at oxidized domains of EGO rich in hydroxyl rather than epoxide groups; in both cases the enthalpy gain per water molecule increases with the water content.

Overall, these results support the picture shown in Figure 35, that the EGO films consist of oxidized carbon layers presenting – at the nanoscale – a non-homogeneous oxidation comprising highly oxidized areas rich in hydroxyl species surrounded by nano-domains of non-oxidized graphene. A small amount of water (<10%) forming strong hydrogen bonds with hydroxyl groups on nearest-neighbor layers would be sufficient to separate an interlayer spacing up to 9 Å, thereby explaining the XRD, AFM and IR experimental results.

5.3 Summary of main results

In this chapter, I investigated the interlayer structure of multilayer EGO films that age at room temperature for several months. XRD, AFM and IR measurement show that

these EGO films inherit the lateral order, number of layers and film registry of pristine graphene, and they exhibit interlayer distances of 9-10 Å, in spite of the minimal concentration of water molecules (<10%) intercalated in the films. DFT-D calculations show that the EGO films most probably consist of oxidized carbon layers, which at the nanoscale present phase separation in highly oxidized and non-oxidized graphene domains, as well as a non-homogeneous distribution of water molecules intercalated in-between the oxidized regions of nearest-neighbor layers. The highly oxidized domains are rich in hydroxyl species, which are prone to trap water molecules. Thanks to the film planarity and mesoscopic homogeneity, only a small amount of water (<10%) would be sufficient to achieve interlayer distances of larger than 9 Å.

The inhomogeneous distribution of water molecules affects the mechanical properties of EGO. Very recent AFM measurements show that the aged EGO films present an out-of-plane Young's modulus (c_{33}) of about 23.5 GPa in the ambient conditions (relative humidity of 10%) (unpublished results). Our calculations show that the EGO models fully covered by hydroxyl groups (Figure 36) have c_{33} values of 13.4 GPa and 18.2 GPa by including 6.25% and 12.5% water, respectively, in agreement with the experiment. In contrast, previous molecular dynamic simulation studies of graphene oxide with homogeneously oxidized carbon layers show that GO with an O:C ratio of 0.3 and 10% water has an interlayer distance of about 7 Å, and a c_{33} value of only 4.8 GPa [77]. These results corroborate our model structure of EGO shown in Figure 35. These studies also reveal that the EGO films possess chemical and structural properties very different from conventional GO. The peculiar structure of EGO may create new properties for this material, which require more studies to understand and utilize for future applications.

CHAPTER VI

CONCLUSION

6.1 Summary

In this thesis work, I investigated the chemical and structural properties of oxidized epitaxial graphene films by density functional theory studies and Monte Carlo simulations. The EGO films are made by Hummers oxidation of graphene that is epitaxially grown on the C face of SiC substrate. Experimental measurements including XPS, AFM, XRD, and IR techniques show that these EGO films preserve the lateral and vertical uniformity of the unoxidized graphene films, and include minimal defects, holes and edges. The EGO films are metastable at room temperature and undergo spontaneous reduction and chemical and structural modifications during a period of about two months. The EGO films that attain quasi-equilibrium structures exhibit interlayer distances of 9-10 Å, with water contents less than 10%.

DFT calculations show that the as-synthesized EGO films contain little amount of water (<2%), and present predominant epoxide and hydroxyl groups, and most probably a certain amount of hydrogen species on the carbon layers. At room temperature, epoxide and hydroxyl groups are able to diffuse on the oxidized layers, and make reactions with the hydrogen species, leading to the formation and desorption of water molecules, and a reduction of 6% oxygen content during one month. After consumption of hydrogen species, the EGO films reach chemical equilibrium through the internal reactions to the formation of H_2O and O_2 molecules, which result in structural changes in EGO persisting for a longer life-time.

Further studies show that the metastability of EGO arises from the large attractions between oxygen species – they drive functional groups to agglomerate on graphene and provide the chance for encounter and making reactions. At mild temperatures ($\leq 70\,^{\circ}\mathrm{C}$), the aging process leads to a non-homogeneous oxidation in EGO consisting – at the nanoscale – of highly oxidized domains surrounded by pristine graphene regions. This redistribution enhances both the chemical and kinetic stability of EGO: within the oxidized regions, the local order and spatial correlation reduce the number of reacting sites; for the pairs of oxygen species susceptible to form O_2 or H_2O, decomposition processes become endothermic and involve large energy barriers due to the attractions from neighboring oxygen functionalities. Consequently, further decomposition is largely inhibited and the material is stabilized through this aging process.

The non-homogeneous intralayer structure of EGO also influences its interlayer spacing.

Calculations show that the oxidized domains in EGO are most probably rich in hydroxyl species, and are prone to trap water molecules. A small amount of water (<10%) forming strong hydrogen bonds with the hydroxyl species on the nearest-neighbor layers would be sufficient to have interlayer spacing up to 9 Å.

These investigations help better understanding the chemical and structural properties of EGO. They suggest promising routes to control the reduction process and to control the structure and properties of EGO without creation of lattice damage by gauging the hydrogen content, and aging the films at mild temperatures, respectively. They shine light in producing new forms of functionalized graphene that are suitable for high-performance electronics as well as many other technologies.

6.2 Future Considerations

There are a few directions deserved further studies to better understand EGO this new material. The first direction is about water. Developing computational methods to determine the exact water content in EGO will be useful for analyzing the chemical compositions of EGO. Possible strategies include simulating the infrared spectral signature or elastic signature of EGO with respect to the water content, and compare with the experimental results. Also a few interesting questions regarding to water remain unanswered, such as the mechanism for water molecules to desorb from the EGO films, the mechanism for water to transport from non-oxidized regions to oxidized regions of EGO, and the chemical stability of the hydrogen bonding network formed by water molecules connecting the oxidized domains on the nearest-neighbor layers. The second direction is to refine the simplistic energy scheme for better predictions of the energy of EGO systems. Studies of the interactions between oxygen species on nearest-neighbor carbon layers will be helpful for modeling the 3D structure of the EGO films. The third direction is to simulate the time-evolution of the aging process in EGO by using kinetic Monte Carlo strategies. Such simulations require a full knowledge of the diffusion and reaction barriers for oxygen species in various local environment, which are challenging but will be useful for experimental control of the aging or annealing process. Last, the peculiar structure may induce new properties for EGO. Both experimental and theoretical works are desired to explore these properties, and thus utilize EGO for future applications.

REFERENCES

[1] Ashcroft, N. W. and Mermin, N. D., *Solid State Physics*. Belmont, CA: Brooks/Cole, Cengage Learning, 1976.

[2] Bagri, A., Grantab, R., Medhekar, N. V., and Shenoy, V. B., "Stability and formation mechanisms of carbonyl- and hydroxyl-decorated holes in graphene oxide," *J. Phys. Chem. C*, vol. 114, pp. 12053–12061, 2010.

[3] Bagri, A., Mattevi, C., Acik, M., Chabal, Y. J., Chhowalla, M., and Shenoy, V. B., "Structural evolution during the reduction of chemically derived graphene oxide," *Nature Chem.*, vol. 2, pp. 581–587, 2010.

[4] Bagus, P. S., Ilton, E. S., and Nelin, C. J., "The interpretation of XPS spectra: Insights into materials properties," *Surface Science Reports*, vol. 68, pp. 273–304, 2013.

[5] Bailey, C. L., Mukhopadhyay, S., Wander, A., Searle, B. G., and Harrison, N. M., "Structure and stability of α-AlF_3 surfaces," *J. Phys. Chem. C*, vol. 113, pp. 4976–4983, 2009.

[6] Bakke, A., Chem, H., and Jolly, W., "A table of absolute core-electron binding-energies for gaseous atoms and molecules," *J. Electron Spectrosc.*, vol. 20, pp. 333–366, 1980.

[7] Balandin, A. A., "Thermal properties of graphene and nanostructured carbon materials," *Nat. Mater.*, vol. 10, pp. 569–581, 2011.

[8] Barone, V., Casarin, M., Forrer, D., Pavone, M., Sambi, M., and Vittadini, A., "Role and effective treatment of dispersive forces in materials: polyethylene and graphite crystals as test cases," *J. Comput. Chem.*, vol. 30, pp. 934–939, 2009.

[9] Berger, C., Song, Z., Li, T., Li, X., Ogbazghi, A. Y., Feng, R., Dai, Z., Marchenkov, A. N., Conrad, E. H., First, P. N., and de Heer, W. A., "Ultrathin epitaxial graphite: 2D electron gas properties and a route toward graphene-based nanoelectronics," *J. Phys. Chem. B*, vol. 108, pp. 19912–19916, 2004.

[10] Birch, F., "Finite elastic strain of cubic crystals," *Phys. Rev.*, vol. 71, pp. 809–824, 1947.

[11] Boukhvalov, D. W. and Katsnelson, M. I., "Modeling of graphite oxide," *J. Am. Chem. Soc.*, vol. 130, pp. 10697–10701, 2008.

[12] Brodie, B. C., "On the atomic weight of graphite," *Phil. Trans. R. Soc. Lond.*, vol. 149, pp. 249–260, 1859.

[13] Brundle, C. R. and Baker, A. D., *Electron Spectroscopy: Theory, Techniques and Applications*, vol. 2. London: Academic Press, 1978.

[14] Ceperley, D. M. and Alder, B. J., "Ground state of the electron gas by a stochastic method," *Phys. Rev. Lett.*, vol. 45, pp. 566–569, 1980.

[15] Cerveny, S., Barroso-Bujans, F., Alegría, Á., and Colmenero, J., "Dynamics of water intercalated in graphite oxide," *J. Phys. Chem. C.*, vol. 114, pp. 2604–2612, 2010.

[16] Chen, C., Rosenblatt, S., Bolotin, K. I., Kalb, W., Kim, P., Kymissis, I., Stormer, H., Heinz, T. F., and Hone, J., "Performance of monolayer graphene nanomechanical resonators with electrical readout," *Nature Nanotechnology*, vol. 4, pp. 861–867, 2009.

[17] Chong, D. P., "Accurate calculation of core-electron binding energies by the density-functional method,"

[18] Chong, D. P., "Density functional calculation of core electron binding energies of C, N, O, and F," *J. Chem. Phys.*, vol. 103, pp. 1842–1845, 1995.

[19] Citrin, P. H. and Thomas, T. D., "X-ray photoelectron spectroscopy of alkali halides," *J. Chem. Phys.*, vol. 57, pp. 4446–4461, 1982.

[20] Compton, O. C., Cranford, S. W., Putz, K. W., An, Z., Brinson, L. C., Buehler, M. J., and Nguyen, S. T., "Tuning the mechanical properties of graphene oxide paper and its associated polymer nanocomposites by controlling cooperative intersheet hydrogen bonding," *ACS Nano*, vol. 6, pp. 2008–2019, 2012.

[21] Curtiss, L. A., Frurip, D. J., and Blander, M., "Studies of molecular association in H_2O and D_2O vapors by measurement of thermal conductivity," *J. Chem. Phys.*, vol. 71, pp. 2703–2711, 1979.

[22] de Heer, W. A., Berger, C., Ruan, M., Sprinkle, M., Li, X., Hu, Y., Zhang, B., Hankinson, J., and Conrad, E. H., "Large area and structured epitaxial graphene produced by confinement controlled sublimation of silicon carbide," *Proceedings of the National Academy of Sciences*, vol. 108, p. 16900, 2011.

[23] Dirac, P. A. M., "Note on exchange phenomena in the Thomas-Fermi atom," *Proc. Cambridge Phil. Roy. Soc.*, vol. 26, pp. 376–385, 1930.

[24] Dreyer, D. R., Jia, H., and Bielawski, C. W., "Graphene oxide: A convenient carbocatalyst for facilitating oxidation and hydration reactions," *Angew. Chem. Int. Ed.*, vol. 49, pp. 6813–6816, 2010.

[25] Eda, G., Fanchini, G., and Chhowalla, M., "Large-area ultrathin films of reduced graphene oxide as a transparent and flexible electronic material," *Nat. Nanotech.*, vol. 3, pp. 270–274, 2008.

[26] Eda, G., Lin, Y., Mattevi, C., Yamaguchi, H., Chen, H., Chen, I., Chen, C., and Chhowalla, M., "Blue photoluminescence from chemically derived graphene oxide," *Adv. Mater.*, vol. 22, pp. 505–509, 2010.

[27] Eigler, S., Enzelberger-Heim, M., Grimm, S., Hofmann, P., Kroener, W., Geworski, A., Dotzer, C., Röckert, M., Xiao, J., Papp, C., Lytken, O.,

Steinrück, H., Müller, P., and Hir, A., "Wet chemical synthesis of graphene," *Adv. Mater.*, vol. 25, pp. 3583–3587, 2013.

[28] Emtsev, K. V., Bostwick, A., Horn, K., Jobst, J., Kellogg, G. L., Ley, L., McChesney, J. L., Ohta, T., Reshanov, S. A., Röhrl, J., Rotenberg, E., Schmid, A. K., Waldmann, D., Weber, H. B., and Seyller, T., "Towards wafer-size graphene layers by atmospheric pressure graphitization of silicon carbide," *Nat. Mater.*, vol. 8, pp. 203–207, 2009.

[29] Emtsev, K. V., Speck, F., Seyller, T., and Ley, L., "Interaction, growth, and ordering of epitaxial graphene on SiC(0001) surfaces: A comparative photoelectron spectroscopy study," *Phys. Rev. B*, vol. 77, p. 155303, 2008.

[30] Erickson, K., Erni, R., Lee, Z., Alem, N., Gannett, W., and Zettl, A., "Determination of the local chemical structure of graphene oxide and reduced graphene oxide," *Adv. Mater.*, vol. 22, pp. 4467–4472, 2010.

[31] Evans, M. G. and Polanyi, M., "Some applications of the transition state method to the calculation of reaction velocities, especially in solution," *Trans. Faraday Soc.*, vol. 31, pp. 875–894, 1935.

[32] Eyring, H., "The activated complex in chemical reactions," *J. Chem. Phys.*, vol. 3, pp. 107–115, 1935.

[33] Fadley, C. S., Hagström, S. B. M., Hollander, J. M., Klein, M. P., and Shirley, D. A., "Chemical bonding information from photoelectron spectroscopy," *Science*, vol. 157, pp. 1571–1573, 1967.

[34] Fadley, C. S., Hagström, S. B. M., Klein, M. P., and Shirley, D. A., "Chemical effects on core-electron binding energies in iodine and europium," *J. Chem. Phys.*, vol. 48, pp. 3779–3794, 1968.

[35] First, P. N., de Heer, W. A., Seyller, T., Berger, C., Stroscio, J. A., and Moon, J., "Epitaxial graphenes on silicon carbide," *MRS Bulletin*, vol. 35, pp. 296–305, 2010.

[36] Fuchs, M. and Scheffler, M., "Ab initio pseudopotentials for electronic structure calculations of poly-atomic systems using density-functional theory," *Computer Physics Communications*, vol. 119, pp. 67–98, 1999.

[37] Fuhrer, M. S., Lau, C. N., and MacDonald, A. H., "Graphene: Materially better carbon," *MRS Bulletin*, vol. 35, pp. 289–295, 2010.

[38] Gauster, W. B. and Fritz, I. J., "Pressure and temperture dependences of the elastic constants of compression-annealed pyrolytic graphite," *J. App. Phys.*, vol. 1974, pp. 3309–3314, 1974.

[39] Geim, A. K. and Novoselov, K. S., "The rise of graphene," *Nat. Mater.*, vol. 6, pp. 183–191, 2007.

[40] Ghaderi, N. and Peressi, M., "First-principle study of hydroxyl functional groups on pristine, defected graphene, and graphene epoxide," *J. Phys. Chem. C*, vol. 114, pp. 21625–21630, 2010.

[41] Giannozzi, P., Baroni, S., Bonini, N., Calandra, M., Car, R., Cavazzoni, C., Ceresoli, D., Chiarotti, G. L., Cococcioni, M., Dabo, I., Dal Corso, A., de Gironcoli, S., Fabris, S., Fratesi, G., Gebauer, R., Gerstmann, U., Gougoussis, C., Kokalj, A., Lazzeri, M., Martin-Samos, L., Marzari, N., Mauri, F., Mazzarello, R., Paolini, S., Pasquarello, A., Paulatto, L., Sbraccia, C., Scandolo, S., Sclauzero, G., Seitsonen, A. P., Smogunov, A., Umari, P., and Wentzcovitch, R. M., "QUANTUM ESPRESSO: A modular and open-source software project for quantum simulations of materials," *J. Phys.: Condens. Matter*, vol. 21, p. 395502, 2009.

[42] Gierz, I., Suzuki, T., Weitz, R. T., Lee, D. S., Krauss, B., Riedl, C., Starke, U., Höchst, H., Smet, J. H., Ast, C. R., and Kern, K., "Electronic decoupling of an epitaxial graphene monolayer by gold intercalation," *Phys. Rev. B*, vol. 81, p. 235408, 2010.

[43] Grimme, S., "Semiempirical GGA-type density functional constructed with a long-range dispersion correction," *J. Comput. Chem.*, vol. 27, pp. 1787–1799, 2006.

[44] Grimme, S., "Density functional theory with London dispersion corrections," *Advanced Review*, vol. 1, pp. 211–228, 2011.

[45] Guinea, F., Katsnelson, M. I., and Geim, A. K., "Energy gaps and a zero-field quantum Hall effect in graphene by strain engineering," *Nat. Phys.*, vol. 6, pp. 30–33, 2010.

[46] Haberer, D., Vyalikh, D. V., Taioli, S., Dora, B., Farjam, M., Fink, J., Marchenko, D., Pichler, T., Ziegler, K., Simonucci, S., Dresselhaus, M. S., Knupfer, M., Büchner, B., and Grüneis, A., "Tunable band gap in hydrogenated quasi-free-standing graphene," *Nano Lett.*, vol. 10, pp. 3360–3366, 2010.

[47] Haerle, R., Riedo, E., Pasquarello, A., and Baldereschi, A., "sp^2/sp^3 hybridization ratio in amorphous carbon from C 1s core-level shifts: X-ray photoelectron spectroscopy and first-principles calculation," *Phys. Rev. B*, vol. 65, p. 045101, 2001.

[48] Han, M. Y., Özyilmaz, B., Zhang, Y., and Kim, P., "Energy band-gap engineering of graphene nanoribbons," *Phys. Rev. Lett.*, vol. 98, p. 206805, 2007.

[49] Hasegawa, M., Nishidate, K., and Iyetomi, H., "Energetics of interlayer binding in graphite: the semiempirical approach revisited," *Phys. Rev. B*, vol. 76, p. 115424, 2007.

[50] Hass, J., Varchon, F., Millán-Otoya, J. E., Sprinkle, M., Sharma, N., de Heer, W. A., Berger, C., First, P. N., Magaud, L., and Conrad, E. H., "Why multilayer graphene on 4H-SiC($000\bar{1}$) behaves like a single sheet of graphene," *Phys. Rev. Lett.*, vol. 100, p. 125504, 2008.

[51] Henkelman, G. and Jónsson, H., "Improved tangent estimate in the nudged elastic band method for finding minimum energy paths and saddle points," *J. Chem. Phys.*, vol. 113, pp. 9978–9985, 2000.

[52] Henkelman, G., Uberuaga, B. P., and Jónsson, H., "A climbing image nudged elastic band method for finding saddle points and minimum energy paths," *J. Chem. Phys.*, vol. 113, pp. 9901–9904, 2000.

[53] Hicks, J., Tejeda, A., Taleb-Ibrahimi, A., Nevius, M. S., Wang, F., Shepperd, K., Palmer, J., Bertran, F., Févre, P. L., Kunc, J., de Heer, W. A., Berger, C., and Conrad, E. H., "A wide-bandgap metal-semiconductor-metal nanostructure made entirely from graphene," *Nat. Phys.*, vol. 9, pp. 49–54, 2013.

[54] Hohenberg, P. and Kohn, W., "Inhomogeneous electron gas," *Physical Review*, vol. 136, pp. 864–870, 1964.

[55] Hossain, M. Z., Johns, J. E., Bevan, K. H., Karmel, H. J., Liang, Y., Yoshimoto, S., Mukai, K., Koitaya, T., Yoshinobu, J., Kawai, M., Lear, A. M., Kesmodel, L. L., Tait, S. L., and Hersam, M. C., "Chemically homogeneous and thermally reversible oxidation of epitaxial graphene," *Nature Chem.*, vol. 4, pp. 305–309, 2012.

[56] Janak, J. F., "Proof that $\partial E/\partial n_i = \epsilon_i$ in density-functional theory," *Phys. Rev. B*, vol. 18, pp. 7165–7168, 1978.

[57] Jansen, H. J. F. and Fressman, A. J., "Structural and electronic properties of graphite via an all-electron total-energy local-density approach," *Phys. Rev. B*, vol. 35, pp. 8207–8214, 1987.

[58] Jónsson, H., Mills, G., and Jacobsen, K. W., *Nudged elastic band method for finding minimum energy paths of transitions*. 1998.

[59] Jr., W. F. E., "Core-level binding-energy shifts at surfaces and in solids," *Surface Science Reports*, vol. 6, pp. 253–415, 1987.

[60] Jr., W. S. H. and Offeman, R. E., "Preparation of graphitic oxide," *J. Am. Chem. Soc.*, vol. 80, pp. 1339–1339, 1958.

[61] Kato, K. and Uda, T., "Backbond oxidation of the Si(001) surface: Narrow channel of barrierless oxidation," *Phys. Rev. Lett.*, vol. 80, pp. 2000–2003, 1998.

[62] Kim, S., Zhou, S., Hu, Y., Acik, M., Chabal, Y. J., Berger, C., Heer, W., Bongiorno, A., and Riedo, E., "Room-temperature metastability of multilayer graphene oxide films," *Nat. Mater.*, vol. 11, pp. 544–549, 2012.

[63] Ko, J. H., Yeo, S., Park, J. H., Choi, J., Nohb, C., and Son, S. U., "Graphene-based electrochromic systems: the case of prussian blue nanoparticles on transparent graphene film," *Chem. Commun.*, vol. 48, pp. 3884–3886, 2012.

[64] Kohn, W., "Nobel Lecture: Electronic structure of matter – wave functions and density functionals," *Reviews of Modern Physics*, vol. 71, pp. 1253–1266, 1999.

[65] Kohn, W. and Sham, L. J., "Self-consistent equations including exchange and correlation effects," *Physical Review*, vol. 140, pp. 1133–1138, 1965.

[66] Kumar, P. V., Bardhan, N. M., Tongay, S., Wu, J., Belcher, A. M., and Grossman, J. C., "Scalable enhancement of graphene oxide properties by thermally driven phase transformation," *Nat. Chem.*, vol. 6, pp. 151–158, 2014.

[67] Laidler, K. J. and Klng, M. C., "The development of transition-state theory," *J. Phys. Chem.*, vol. 87, pp. 2657–2664, 1983.

[68] Langhoff, S. R., "Ab initio evaluation of the fine structure of the oxygen molecule," *J. Chem. Phys.*, vol. 61, pp. 1708–1716, 1974.

[69] Lauffer, P., Emtsev, K. V., Graupner, R., Seyller, T., and Ley, L., "Atomic and electronic structure of few-layer graphene on SiC(0001) studied with scanning tunneling microscopy and spectroscopy," *Phys. Rev. B*, vol. 77, p. 155426, 2008.

[70] Lee, C., Wei, X., Kysar, J. W., and Hone, J., "Measurement of the elastic properties and intrinsic strength of monolayer graphene," *Science*, vol. 321, pp. 385–388, 2008.

[71] Lerf, A., Buchsteiner, A., Pieper, J., Schöttl, S., Dekany, I., Szabo, T., and Boehm, H. P., "Hydration behavior and dynamics of water molecules in graphite oxide," *Phys. Chem. Solids*, vol. 2006, pp. 1106–1110, 67.

[72] Lerf, A., He, H., Forster, M., and Klinowski, J., "Structure of graphite oxide revisited," *J. Phys. Chem. B*, vol. 102, pp. 4477–4482, 1998.

[73] Li, X., Cai, W., An, J., Kim, S., Nah, J., Yang, D., Piner, R., Velamakanni, A., Jung, I., Tutuc, E., Banerjee, S. K., Colombo, L., and Ruoff, R. S., "Large-area synthesis of high-quality and uniform graphene films on copper foils," *Science*, vol. 324, pp. 1312–1314, 2009.

[74] Lian, P., Zhu, X., Liang, S., Li, Z., Yang, W., and Wang, H., "Large reversible capacity of high quality graphene sheets as an anode material for lithium-ion batteries," *Electrochimica Acta*, vol. 55, pp. 3909–3914, 2010.

[75] Liu, M., Yin, X., Ulin-Avila, E., Geng, B., Zentgraf, T., Ju, L., Wang, F., and Zhang, X., "A graphene-based broadband optical modulator," *Nature*, vol. 474, pp. 64–67, 2011.

[76] Loh, K. P., Bao, Q., Eda, G., and Chhowalla, M., "Graphene oxide as a chemically tunable platform for optical applications," *Nat. Chem*, vol. 2, pp. 1015–1024, 2010.

[77] Medhekar, N. V., Ramasubramaniam, A., Ruoff, R. S., and Shenoy, V. B., "Hydrogen bond networks in graphene oxide composite paper: Structure and mechanical properties," *ACS Nano*, vol. 4, pp. 2300–2306, 2010.

[78] Mills, G. and Jónsson, H., "Quantum and thermal effects in H_2 dissociative adsorption: Evaluation of free energy barriers in multidimensional quantum systems," *Phys. Rev. Lett.*, vol. 72, pp. 1124–1127, 1994.

[79] Mills, G., Jónsson, H., and Schenter, G. K., "Reversible work transition state theory: application to dissociative adsorption of hydrogen," *Surface Science*, vol. 324, pp. 305–337, 1995.

[80] Mkhoyan, K. A., Contryman, A. W., Silcox, J., Stewart, D. A., Eda, G., Mattevi, C., Miller, S., and Chhowalla, M., "Atomic and electronic structure of graphene-oxide," *Nano Lett.*, vol. 9, pp. 1058–1063, 2009.

[81] Nair, R. R., Blake, P., Grigorenko, A. N., Novoselov, K. S., Booth, T. J., Stauber, T., Peres, N. M. R., and Geim, A. K., "Fine structure constant defines visual transparency of graphene," *Science*, vol. 320, pp. 1308–1308, 2008.

[82] Neto, A. H. C., Guinea, F., Peres, N. M. R., Novoselov, K. S., and Geim, A. K., "The electronic properties of graphene," *Rev. Mod. Phys.*, vol. 81, pp. 109–162, 2009.

[83] Niyogi, S., Bekyarova, E., Hong, J., Khizroev, S., Berger, C., de Heer, W., and Haddon, R. C., "Covalent chemistry for graphene electronics," *J. Phys. Chem. Lett.*, vol. 2, pp. 2487–2498, 2011.

[84] Novoselov, K. S., Jiang, D., Schedin, F., Booth, T. J., Khotkevich, V. V., Morozov, S. V., and Geim, A. K., "Two-dimensional atomic crystals," *Proceedings of the National Academy of Sciences*, vol. 102, pp. 10451–10454, 2005.

[85] Odutola, J. A. and Dyke, T. R., "Partially deuterated water dimers: Microwave spectra and structure," *J. Chem. Phys.*, vol. 72, pp. 5062–5070, 1980.

[86] Orellana, W., da Silva, A. J. R., and Fazzio, A., "Oxidation at the Si/SiO_2 interface: Influence of the spin degree of freedom," *Phys. Rev. Lett.*, vol. 90, p. 016103, 2003.

[87] Orlita, M., Faugeras, C., Plochocka, P., Neugebauer, P., Martinez, G., Maude, D. K., Barra, A. L., and Sprinkle, M., "Approaching the Dirac point in high mobility multilayer epitaxial graphene," *Phys. Rev. Lett.*, vol. 101, p. 267601, 2008.

[88] Pehlke, E. and Scheffler, M., "Evidence for site-sensitive screening of core holes at the Si and Ge (001) surface," *Phys. Rev. Lett.*, vol. 71, pp. 2338–2341, 1993.

[89] Perdew, J. P., Burke, K., and Ernzerhof, M., "Generalized gradient approximation made simple," *Phys. Rev. Lett.*, vol. 77, pp. 3865–3868, 1996.

[90] Perdew, J. P. and Zunger, A., "Self-interaction correction to density-functional approximations for many-electron systems," *Phys. Rev. B*, vol. 23, pp. 5048–5079, 1981.

[91] Perdew, J. P. and Wang, Y., "Accurate and simple analytic representation of the electron-gas correlation energy," *Phys. Rev. B*, vol. 45, pp. 13244–13249, 1992.

[92] Radhakrishnan, G., Cardema, J. D., Adams, P. M., Kim, H. I., and Foran, B., "Fabrication and electrochemical characterization of single and multilayer graphene anodes for lithium-ion batteries," *J. Electrochem. Soc.*, vol. 159, pp. A752–A761, 2012.

[93] Reuter, K. and Scheffler, M., "Composition, structure, and stability of $RuO_2(110)$ as a function of oxygen pressure," *Phys. Rev. B*, vol. 65, p. 035406, 2001.

[94] Riedl, C., Coletti, C., Iwasaki, T., Zakharov, A. A., and Starke, U., "Quasi-free-standing epitaxial graphene on SiC obtained by hydrogen intercalation," *Phys. Rev. Lett.*, vol. 103, p. 246804, 2009.

[95] Riedl, C. and Starke, U., "Structural properties of the graphene-SiC(0001) interface as a key for the preparation of homogeneous large-terrace graphene surfaces," *Phys. Rev. B*, vol. 76, p. 245406, 2007.

[96] Robinson, J. T., Burgess, J. S., Junkermeier, C. E., Badescu, S. C., Reinecke, T. L., Perkins, F. K., Zalalutdniov, M. K., Baldwin, J. W., Culbertson, J. C., Sheehan, P. E., and Snow, E. S., "Properties of fluorinated graphene films," *Nano Lett.*, vol. 10, pp. 3001–3005, 2010.

[97] Rydberg, H., Dion, M., Jacobson, N., Schröder, E., Hyldgaard, P., Simak, S. I., Langreth, D. C., and Lundqvist, B. I., "Van der Waals density functional for layered structures," *Phys. Rev. Lett.*, vol. 91, p. 126402, 2003.

[98] Sarkar, S., Bekyarova, E., and Haddon, R. C., "Chemistry at the Dirac point: Diels-alder reactivity of graphene," *Accounts of Chemical Research*, vol. 45, pp. 673–682, 2012.

[99] Schedin, F., Geim, A. K., Morozov, S. V., Hill, E. W., Blake, P., Katsnelson, M. I., and Novoselov, K. S., "Detection of individual gas molecules adsorbed on graphene," *Nat. Mater.*, vol. 6, pp. 652–655, 2007.

[100] Schniepp, H. C., Li, J.-L., McAllister, M. J., Sai, H., Herrera-Alonso, M., Adamson, D. H., Prudhomme, R. K., Car, R., Saville, D. A., and Aksay, I. A., "Functionalized single graphene sheets derived from splitting graphite oxide," *J. Phys. Chem. B*, vol. 110, pp. 8535–8539, 2006.

[101] Schwerdtfeger, P., "The pseudopotential approximation in electronic structure theory," *ChemPhysChem*, vol. 12, pp. 3143–3155, 2011.

[102] Schwierz, F., "Graphene transistors," *Nature Nanotechnology*, vol. 5, pp. 487–496, 2010.

[103] Sheppard, D., Terrell, R., and Henkelman, G., "Optimization methods for finding minimum energy paths," *J. Chem. Phys.*, vol. 128, p. 134106, 2008.

[104] Sherpa, S. D., Levitin, G., and Hess, D. W., "Effect of the polarity of carbon-fluorine bonds on the work function of plasma-fluorinated epitaxial graphene," *Appl. Phys. Lett.*, vol. 101, p. 111602, 2012.

[105] Sholl, D. S. and Steckel, J. A., *Density Functional Theory: A Practical Introduction*. Hoboken, New Jersey: John Wiley & Sons, 2009.

[106] Singh, V., Joung, D., Zhai, L., Das, S., Khondaker, S. I., and Seal, S., "Graphene based materials: Past, present and future," *Progress in Materials Science*, vol. 56, pp. 1178–1271, 2011.

[107] Slater, J. C., "Statistical exchange-correlation in the self-consistent field," *Adv. Quant. Chem.*, vol. 6, pp. 1–92, 1972.

[108] Šljivančanin, Ž., Milošević, A. S., Popović, Z. S., and Vukajlović, F. R., "Binding of atomic oxygen on graphene from small epoxy clusters to a fully oxidized surface," *Carbon*, vol. 54, pp. 482–488, 2013.

[109] Smith, A. D., Niklaus, F., Paussa, A., Vaziri, S., Fischer, A. C., Sterner, M., Forsberg, F., Delin, A., Esseni, D., Palestri, P., Östling, M., and Lemme, M. C., "Electromechanical piezoresistive sensing in suspended graphene membranes," *Nano Lett.*, vol. 13, pp. 3237–3242, 2013.

[110] Sofo, J. O., Chaudhari, A. S., and Barber, G. D., "Graphane: A two-dimensional hydrocarbon," *Phys. Rev. B*, vol. 75, p. 153401, 2007.

[111] Sprinkle, M., Hicks, J., Tejeda, A., Taleb-Ibrahimi, A., Févre, P. L., Bertran, F., Tinkey, H., Clark, M. C., Soukiassian, P., Martinotti, D., Hass, J., and Conrad, E. H., "Multilayer epitaxial graphene grown on the SiC$(000\bar{1})$ surface; structure and electronic properties," *J. Phys. D*, vol. 43, p. 374006, 2010.

[112] Sprinkle, M., Siegel, D., Hu, Y., Hicks, J., Tejeda, A., Taleb-Ibrahimi, A., Févre, P. L., Bertran, F., Vizzini, S., Enriquez, H., Chiang, S., Soukiassian, P., Berger, C., de Heer, W. A., Lanzara, A., and Conrad, E. H., "First direct observation of a nearly ideal graphene band structure," *Phys. Rev. Lett.*, vol. 103, p. 226803, 2009.

[113] Stull, D. R. and Prophet, H., *JANAF Thermochemical Tables*. Washington, DC: U.S. National Bureau of Standards, 1971.

[114] Szabo, A. and Ostlund, N. S., *Modern Quantum Chemistry*. Mineola, New York: Dover Publishing, 1996.

[115] Thomas, L. H., "The calculation of atomic fields," *Proc. Cambridge Phil. Soc.*, vol. 23, pp. 542–548, 1927.

[116] Travaly, Y., Vanderbilt, D., and Gonze, X., "Calculation of C 1s core-level shifts in poly(ethylene terephthalate) and comparison with X-ray photoelectron spectroscopy," *Phys. Rev. B*, vol. 61, pp. 7716–7721, 2000.

[117] Triguero, L., Plashkevych, O., Pettersson, L. G. M., and Agren, H., "Separate state vs. transition state Kohn-Sham calculations of X-ray photoelectron binding energies and chemical shifts," *J. Electron Spectrosc. Relat. Phenom.*, vol. 104, pp. 195–207, 1999.

[118] Truhlar, D. G., Hase, W. L., and Hynes, J. T., "Current status of transition-state theory," *J. Phys. Chem.*, vol. 87, pp. 2664–2682, 1983.

[119] Trygubenko, S. A. and Wales, D. J., "A doubly nudged elastic band method for finding transition states," *J. Chem. Phys.*, vol. 120, pp. 2082–2094, 2004.

[120] Vinogradov, N. A., Schulte, K., Ng, M. L., Mikkelsen, A., Lundgren, E., Martensson, N., and Preobrajenski, A. B., "Impact of atomic oxygen on the structure of graphene formed on Ir(111) and Pt(111)," *J. Phys. Chem. C*, vol. 115, pp. 9568–9577, 2011.

[121] Wallace, P. R., "The band theory of graphite," *Phys. Rev.*, vol. 71, pp. 622–634, 1947.

[122] Wang, X., Zhi, L., and Müllen, K., "Transparent, conductive graphene electrodes for dye-sensitized solar cells," *Nano Lett.*, vol. 8, pp. 323–327, 2008.

[123] Wei, Z., Wang, D., Kim, S., Kim, S.-Y., Hu, Y., Yakes, M. K., Laracuente, A. R., Dai, Z., Marder, S. R., Berger, C., King, W. P., de Heer, W. A., Sheehan, P. E., and Riedo, E., "Nanoscale tunable reduction of graphene oxide for graphene electronics," *Science*, vol. 328, pp. 1373–1376, 2010.

[124] Wheeler, V., Garces, N., Nyakiti, L., Myers-Ward, R., Jernigan, G., Culbertson, J., Jr., C. E., and Gaskill, D. K., "Fluorine functionalization of epitaxial graphene for uniform deposition of thin high-k dielectrics," *Carbon*, vol. 50, pp. 2307–2314, 2012.

[125] Williams, A. R., deGroot, R. A., and Sommers, C. B., "Generalization of Slaters transition state concept," *J. Chem. Phys.*, vol. 63, pp. 628–631, 1975.

[126] Winograd, N. and Gaarenstroom, S. W., *X-ray Photoelectron Spectroscopy*, vol. 2. New York: Academic Press, 1978.

[127] Xu, M., Fujita, D., and Hanagata, N., "Perspectives and challenges of emerging single-molecule DNA sequencing technologies," *Small*, vol. 5, pp. 2638–2649, 2009.

[128] Yan, J.-A., Xian, L., and Chou, M. Y., "Structural and electronic properties of oxidized graphene," *Phys. Rev. Lett*, vol. 103, p. 086802, 2009.

[129] Yoon, D., Son, Y., and Cheong, H., "Negative thermal expansion coefficient of graphene measured by Raman spectroscopy," *Nano Lett.*, vol. 11, pp. 3227–3231, 2011.

[130] Zacharia, R., Ulbricht, H., and Hertel, T., "Interlayer cohesive energy of graphite from thermal desorption of polyaromatic hydrocarbons," *Phys. Rev. B*, vol. 69, p. 155406, 2004.

[131] Zener, C., "Non-adiabatic crossing of energy levels," *Proc. R. Soc. Lond. A*, vol. 137, pp. 696–702, 1932.

[132] Zhang, F., Zhang, T., Yang, X., Zhang, L., Leng, K., Huang, Y., and Chen, Y., "A high-performance supercapacitor-battery hybrid energy storage device based on graphene-enhanced electrode materials with ultrahigh energy density," *Energy Environ. Sci.*, vol. 6, pp. 1623–1632, 2013.

[133] Zhang, Y., Tang, T., Girit, C., Hao, Z., Martin, M. C., Zettl, A., Crommie, M. F., Shen, Y. R., and Wang, F., "Direct observation of a widely tunable bandgap in bilayer graphene," *Nature*, vol. 459, pp. 820–823, 2009.

[134] Zhou, S. and Bongiorno, A., "Origin of the chemical and kinetic stability of graphene oxide," *Scientific Reports*, vol. 3, p. 2484, 2013.

[135] Zhou, S., Kim, S., and Bongiorno, A., "Chemical structure of oxidized multilayer epitaxial graphene: A density functional theory study," *J. Chem. Phys. C*, vol. 117, pp. 6267–6274, 2013.

[136] Zhou, S., Kim, S., Gennaro, E. D., Hu, Y., Gong, C., Lu, X., Berger, C., de Heer, W., Riedo, E., Chabal, Y. J., Aruta, C., and Bongiorno, A., "Film structure of epitaxial graphene oxide on sic: Insight on the relationship between interlayer spacing, water content, and intralayer structure," *Adv. Mater. Interfaces.*, p. 1300106, 2014.

[137] Zhou, S. Y., Gweon, G. H., Fedorov, A. V., First, P. N., der Heer, W. A., Lee, D. H., Guinea, F., Neto, A. H. C., and Lanzara, A., "Substrate-induced bandgap opening in epitaxial graphene," *Nat. Mater.*, vol. 6, pp. 770–775, 2007.

[138] Zhu, Y., Murali, S., Stoller, M. D., Ganesh, K. J., Cai, W., Ferreira, P. J., Pirkle, A., Wallace, R. M., Cychosz, K. A., Thommes, M., Su, D., Stach, E. A., and Ruof, R. S., "Carbon-based supercapacitors produced by activation of graphene," *Science*, vol. 332, pp. 1537–1541, 2011.